EUV and Coronagraphic Observations of Coronal Mass Ejections

Dissertation
zur Erlangung des Doktorgrades
der Mathematisch-Naturwissenschaftlichen Fakultäten
der Georg-August-Universität zu Göttingen

vorgelegt von
Durgesh Kumar Tripathi
aus Gorakhpur / India

Göttingen 2005

Bibliografische Information Der Deutschen Bibliothek

Die Deutsche Bibliothek verzeichnet diese Publikation in der Deutschen Nationalbibliografie; detaillierte bibliografische Daten sind im Internet über `http://dnb.ddb.de` abrufbar.

D7
Referent: Prof. Dr. Franz Kneer
Korreferent: Prof. Dr. Rainer Schwenn
Tag der mündlichen Prüfung: 17. Februar 2005

Copyright © Copernicus GmbH 2005

ISBN 3-936586-35-7

Copernicus GmbH, Katlenburg-Lindau
Druck: Schaltungsdienst Lange, Berlin

Printed in Germany

We are at the very beginning of time for the human race. It is not unreasonable that we grapple with problems. But there are tens of thousands of years in the future. Our responsibility is to do what we can, learn what we can, improve the solutions, and pass them on.

Richard P. Feynman (1918 - 1988)

Dedicated to my parents....

Contents

Abstract **xi**

1 Introduction **1**

2 The Sun and its Atmosphere **5**
2.1 Introduction 5
2.2 Solar Interior 5
2.3 Solar Atmosphere 6
2.3.1 The Photosphere 7
2.3.2 The Chromosphere 7
2.3.3 Transition Region 8
2.3.4 The Corona 8
2.4 The Structure of the Solar Corona 12
2.5 The Solar Activity Cycle 15

3 Coronal Mass Ejections **17**
3.1 Introduction 17
3.2 Observed properties of CMEs 18
3.2.1 Shape and Geometry 19
3.2.2 Physical Parameters 20
3.3 Source Regions of Coronal Mass Ejections 22
3.3.1 CMEs and Sunspots 22
3.3.2 CMEs and Erupting Prominences/Disappearing Filaments . . 23
3.3.3 Flares and CME Onset 25
3.3.4 CMEs and X-ray Sigmoids 26
3.3.5 CMEs and Post-Eruptive Arcades (PEAs) 27
3.3.6 Extreme Ultraviolet Imaging Telescope (EIT) Waves and CMEs 28
3.4 Theoretical Concepts of CMEs 29
3.4.1 Thermal Blast Wave 32
3.4.2 Dynamo Model 32
3.4.3 Mass Loading Model 32
3.4.4 Tether Cutting Model 33
3.4.5 Tether Straining Model 33
3.5 Summary 33

4 Instruments **35**
4.1 Introduction . . . 35
4.2 The Solar and Heliospheric Observatory (SoHO) . . . 36
    4.2.1 The Extreme Ultraviolet Imaging Telescope (EIT) . . . 38
    4.2.2 The Large Angle Spectrometric Coronagraph (LASCO) . . . 40
    4.2.3 Michelson Doppler Imager (MDI) . . . 42
4.3 Complementary Data . . . 44
    4.3.1 Ground-Based Hα Observations . . . 44
    4.3.2 *Yohkoh* Soft X-Ray Telescope (SXT) . . . 45

5 Observations and Data Analysis **47**
5.1 Introduction . . . 47
5.2 Identification of Post-Eruptive Arcades . . . 47
5.3 Photospheric Magnetic Field Data . . . 49
5.4 Correlation of PEAs with CMEs . . . 51
5.5 Image Processing Using Wavelets . . . 53
5.6 Remapping of MDI Magnetograms . . . 56

6 Properties of EUV Post-Eruptive Arcades **59**
6.1 Introduction . . . 59
6.2 The Basic Properties of PEAs . . . 60
    6.2.1 EIT 195 Å Emission Lifetime . . . 60
    6.2.2 Heliographic Positions, Spatial Lengths and Latitude Variations 60
6.3 Photospheric Source Regions and Solar Cycle Dependence . . . 63
6.4 Summary and conclusions . . . 70

7 EUV PEAs and CMEs **73**
7.1 Introduction . . . 73
7.2 Association of PEAs with CMEs . . . 73
7.3 Comparison with Ground-Based Hα Data . . . 75
7.4 Multi-Wavelength Investigation of PEAs . . . 77
7.5 Summary and Conclusions . . . 80

8 Plasma Downflows above PEAs after CME Eruptions **83**
8.1 Introduction . . . 83
8.2 Observations . . . 84
8.3 Evolution of Prominence, CME and Downflow . . . 88
8.4 Discussion and Conclusions . . . 94

9 Photospheric Magnetic Flux Evolution in the Source Regions of CMEs **97**
9.1 Introduction . . . 97
9.2 Data Selection and Analysis . . . 99
9.3 Observational Summary of Events . . . 99
9.4 Discussion and Conclusions . . . 109

10 Summary and Conclusions **111**

Perspectives **113**

A Observation Table **115**

B Magnetic Reconnection **125**

Bibliography **127**

Acknowledgements **137**

Scientific Contributions **139**

Lebenslauf **141**

List of Figures

1.1 Example of coronal mass ejection 2
1.2 Example of a post-eruptive arcade recorded on 14-Jul-2000 3

2.1 Six layers of Sun. Courtesy: SoHO consortium. 6
2.2 The solar atmosphere: temperature and density profile (source: Lang 2001) . . . 8
2.3 Images of solar eclipse. Courtesy: HAO/NCAR 9
2.4 Green line corona imaged by LASCO/C1. courtesy: M. Mierla. 10
2.5 Solar corona in EUV and X-ray. Courtesy: EIT and SXT consortium. 11
2.6 Solar corona in soft X-ray. Courtesy: SXT team. 12
2.7 Solar coronal structures (Aschwanden 2004). 13
2.8 MDI magnetogram. Courtesy: SoHO/MDI. 13
2.9 Magnetic carpet. Courtesy: Stanford LMSAL. 14
2.10 Butterfly pattern. Courtesy: MSFC. 15
2.11 SXT and MDI comparison. Courtesy: KPNO and Yohkoh team. 16

3.1 An example of a coronal mass ejection observed by SoHO/LASCO/C3 18
3.2 Example of a three part structured CME observed by LASCO/C3. 19
3.3 Example of a halo CME 20
3.4 Measurement of the angular width of a CME (source: Cremades & Bothmer 2004) 21
3.5 Statistics for halo CMEs (source: Gopalswamy et al. 2003) 22
3.6 Comparison of CME rate and sunspot number (source: Gopalswamy et al. 2003) 23
3.7 Comparison of CMEs with prominences (source: Gopalswamy et al. (2003) . . . 24
3.8 Phase transition of a CME with respect to the soft X-ray flux profile 26
3.9 Sigmoid to arcade evolution. Courtesy: Yohkoh/SXT team. 27
3.10 PEA imaged by TRACE (source: Triapthi et al. 2004) 28
3.11 An example of EIT wave (source: Thompson et al. 1998) 29
3.12 Arcade and flux-rope configuration (source: Klimchuk 2001) 30
3.13 Example of flux-rope CME (source: Chen et al. 1997) 31
3.14 Mechanical analogs for different CME models (source: Klimchuk 2001) 34

4.1 Schematic of SoHO (source: Domingo et al. 1995) 36
4.2 SoHO orbit (source: Domingo et al. 1995) 38
4.3 Solar corona at different temperatures imaged by SoHO/EIT. 39
4.4 EIT optical element (source: Dere et al. 2000) 40
4.5 Images of the solar corona taken by LASCO/C1, C2, C3 42
4.6 Example of SoHO/MDI magnetogram 43
4.7 Hα images taken by BBSO and Meudon observatories. 44

4.8 X-ray image taken by Yohkoh/SXT 45

5.1 Example of post-eruptive arcade 48
5.2 Total number of identified PEAs 49
5.3 Schematic diagram of PEA appearence 50
5.4 MDI magnetogram synoptic chart 51
5.5 Example of post-eruptive arcade 51
5.6 Schematic representation of position angle measurements and height-time diagram 52
5.7 Schematic illustration of wavelet packet analysis (source: Stenborg & Cobelli 2003) 54
5.8 Comparison between raw data and wavelet processed data 55
5.9 Full-disk and remapped magnetograms 57

6.1 Example of a post-eruptive arcade recorded on 24-Jun-1999 by EIT at 195 Å . . 59
6.2 Schematics for PEA formations (source: Kopp and Pneuman 1976; adopted from Svestka 2003) 61
6.3 Life-time frequency distribution of PEAs 62
6.4 Carrington map of EUV PEAs 62
6.5 Length distribution of EUV PEAs. 63
6.6 Variation of length of PEAs with latitude 64
6.7 MDI Carrington maps and EUV PEAs 65
6.8 Sketch of possible pre- and post-eruption magnetic field configuration 67
6.9 Yearly variation of PEAs 68
6.10 Distribution of PEAs corresponding to their polarity 69
6.11 Latitude variation of PEAs with time 70

7.1 An example of PEA and associated CME 74
7.2 Height-time diagram of CME measured in SoHO/LASCO C2&C3 FOV 75
7.3 Distribution of PEAs over the heliographic longitude 76
7.4 An example of halo CME with it's corresponding source region in EUV and Hα . 76
7.5 Comparison of PEAs with Hα filament 77
7.6 Source region of CME on 17-Feb.-2000 in different wavelengths 78
7.7 Comparison of GOES X-ray flux with CME and PEA onset. 79
7.8 X-ray coronal brightening and PEAs 80

8.1 EIT running difference images showing prominence eruptions 85
8.2 LASCO/C2 running difference images showing the associated CME 85
8.3 EIT running difference images showing the downflow 86
8.4 Stack plot showing the eruption and downflow 87
8.5 Height-time diagram for LASCO/C2 and EIT 89
8.6 Wavelet processed images taken from EIT, LASCO/C2 & C3 90
8.7 Position angle, height-time and speed-height profiles 92
8.8 Absolute and vertical speed profile of the downflow 93
8.9 Schematic diagram for the downflow 96

9.1 Hα, EIT 195 Å and MDI magnetogram observations for the event on 23-Oct-1997 102
9.2 Hα, EIT 195 Å and MDI magnetogram observations for the event on 24-Jun-1999 103
9.3 Hα, EIT 195 Å and MDI magnetogram observations for the event on 05-Mar-2000 104

9.4 Hα, EIT 195 Å and MDI magnetogram observations for the event on 29-Apr-2000 105
9.5 Hα, EIT 195 Å and MDI magnetogram observations for the event on 31-May-2000 106
9.6 Hα, EIT 195 Å and MDI magnetogram observations for the event on 04-Sep-2000 107
9.7 Hα, EIT 195 Å and MDI magnetogram observations for the event on 12-Sep-2000 108

List of Tables

2.1 Basic physical parameters of Sun (after Lang 2001) 7

3.1 Properties of coronal mass ejections 20
3.2 The soft X-ray classification of solar flares (Harra 2004). 26

4.1 The SoHO Scientific Instruments (Domingo et al. (1995) 37
4.2 EIT Bandpasses. After Delaboudiénere et al. (1995) 41

7.1 Chronological evolutions of post-eruptive arcades 77

9.1 Observational summary of events 101

A.1 Observational summary of EUV post-eruptive arcades 115

Abstract

Coronal Mass Ejections (CMEs) are one of the most spectacular manifestations of solar activity. Remote sensing and in-situ measurements from various spacecraft have revealed during the past decade that CMEs are the prime agents of interplanetary shock waves, solar energetic particle events and geomagnetic storms. In order to better understand the physical processes causing the space weather effects, it becomes mandatory to investigate the physics of CMEs. Especially the question about the initiation of CMEs and their evolution in interplanetary space is a major scientific challenge. The Extreme-ultraviolet Imaging Telescope (EIT) and the Large Angle Spectrometric Coronagraph (LASCO) aboard the Solar and Heliospheric Observatory (SoHO) provide, since launch in December 1995, unprecedented observations of dynamic processes in the solar corona over the spatial range 1.1 - 30 $R_\odot$. Observations taken by EIT at 195 Å from 1997 - 2002 have been investigated to study for the first time systematically the physical properties of transient large-scale loop systems, termed *Post-Eruptive Arcades* (PEAs), often observed in association with CMEs and X-ray flares. The simultaneous white-light observations from LASCO/C2 were analyzed to investigate the general association between PEAs and CMEs. During the years 1997 - 2002, 236 PEA events were identified based on specific selection criteria that allowed a detailed analysis of these events. An almost *one-to-one* correlation was found between the identified EUV PEAs and white-light CMEs detected by SoHO/LASCO. The result implies that EUV PEAs can be considered as reliable disk tracers of CMEs even without simultaneous white-light coronagraph observations. A detailed study of the plasma dynamics of a limb event showed a *bright coronal inflow* above the PEA, interpreted as evidence for magnetic reconnection processes in the course of the magnetic restructuring taking place in the aftermath of CMEs.

The entire set of studied PEAs provides an ideal data-set to study the evolution of the magnetic field in the source regions of CMEs before, during and after the eruption using SoHO Michelson Doppler Imager (MDI) magnetogram observations. To avoid the impact of line-of-sight (LOS) effects, only disk-centered events were studied. Contrary to the belief that bipole emergences and X-line type formations are precursors of CMEs we found that flux cancellations and field evolutions in active regions located near-by, as well as bipole emergences without formations of X-lines are also processes associated with the onsets of CMEs. More sophisticated studies of the CME source regions are needed making use of vector magnetograms taken with sufficient time resolution. Upcoming missions like Solar-B and Solar TErrestrial RElation Observatory (STEREO) will provide with this information.

1 Introduction

Today we know that the Sun is a dynamic star and that its surface and atmospheric structure is continuously changing. Regions of intertwined magnetic fields arise from the solar interior and give rise to active regions, sunspots, and coronal holes at the Sun's visible surface, giving rise to prominences, helmet streamers, spicules, amongst other features.

The first detailed observation of a powerful lightning of electromagnetic emission, a solar flare, was made by Carrington and Hodge in 1859 (Carrington 1859). During the regular observations of Sunspots, Carrington and Hodge observed a strong white-light brightening for about five minutes. Magnetic disturbances were observed at Earth within the next 24 hours together with a spectacular aurora seen at mid-latitudes. The observations and scientific conclusions of Carrington and Hodge that the flare was the onset of the solar storm that reached the Earth about a day later appears as a milestone in the systematic investigation of the influences of solar activity on Earth's environment.

Space-based telescope observations during the past several decades have revealed the frequent occurrence of giant explosions in the outer solar atmosphere, the corona. These so called *Coronal Mass Ejections* (CMEs) have masses at the order of 10^{13} kg and reach propagation speeds upto 3000 km/s.

A coronal mass ejection (CME) is defined as an observable change in the coronal structure that:

- occurs on a time-scale between a few minutes and several hours, and
- involves the appearance and outward motion of a new, discrete, bright, white-light feature in the coronagraphic field of view (Hundhausen et al. 1984, Schwenn 1996).

CMEs were systematically observed with coronagraphs aboard *Skylab* (1973-1974, MacQueen et al. 1974), *SOLWIND* (Michels et al. 1980) on board *P78-1* and Corona/Polarimeter on board *Solar Maximum Mission* (*SMM, 1984-1989)* (MacQueen et al. 1980). Today the *Large Angle Spectrometric Coronagraph* (LASCO, Brueckner et al. 1995) aboard *Solar and Heliospheric Observatory* (SoHO, Domingo et al. 1995) provides unique observations of CMEs.

An example of a spectacular CME is shown in Fig. 1.1 as a sequence of four images obtained by LASCO/C2 aboard SoHO on 20-Apr-1998. In the figure the white solid circles indicate the solar limb in the shadow of the coronagraphic occulting disk. In the images north points upward and west towards the right. The

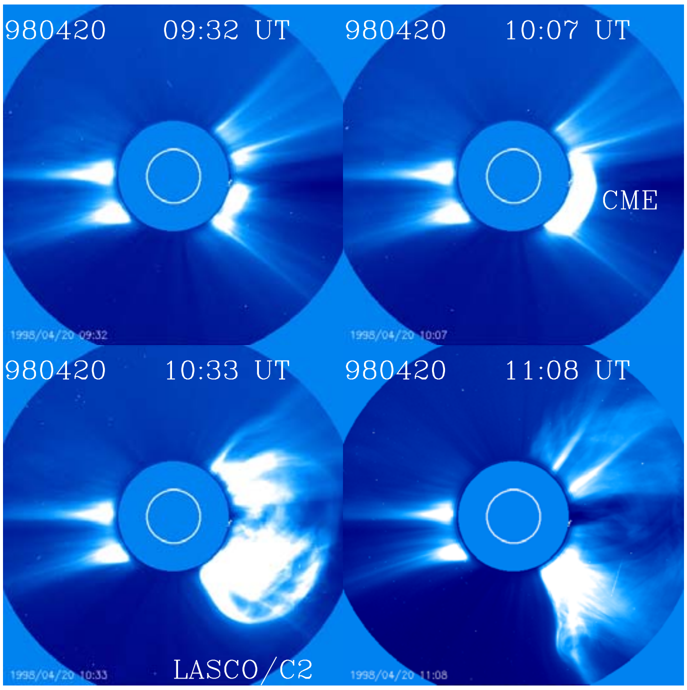

Figure 1.1: Series of LASCO/C2 images showing a coronal mass ejection at the west limb. The appearance of the CME was first detected by LASCO/C2 at 10:07 UT (Top right panel). The white circles in the images demark the solar limb. In the images north points upward and west towards the right. Courtesy: SoHO/LASCO consortium.

bright feature which appeared at the west limb in the south-west quadrant (top right panel at 10:07 UT) expanded outwards in the following images. This feature moved outward through the corona with a speed of about 1863 km/s. The CME perturbed the corona over a spatial angle of about 165°.

CMEs are one of the most spectacular and striking manifestations of solar activity. Apparently they result from a rapid, large-scale restructuring of magnetic fields in the low corona and photosphere (Forbes 2000, Klimchuk 2001). The magnetized plasma of a CME can substantially disturb the Earth's environment, notable as a geomagnetic storm, intense aurorae or sometimes even through electrical power blackouts (e.g., Daglis 2004). Additionally some CMEs accelerate charged particles to high energies, up to GeV, which cause radiation hazards to astronauts. Despite all these tangible effects, unfortunately many aspects of the physics of CMEs, e.g. their solar origin and interplanetary evolution, are not well understood.

The identification of the source regions of CMEs has been a subject of intensive research in solar physics since their first detection in the 1970s. Solar flares are often observed in tight association with CMEs (e.g., Harrison 1986, 1995). However, there are now many observed CMEs which were not associated with flares and vice-versa (e.g., Kahler 1992, Gosling 1993). In order to identify the source regions of CMEs, erupting prominences (disappearing filaments) represent one of the best phenomena of solar activity (e.g., Webb and Hundhausen 1987). However, many CMEs originating from active regions on the Sun are not associated with a disappearing filament (Subramanian and Dere 2001). The X-ray brightening of S-

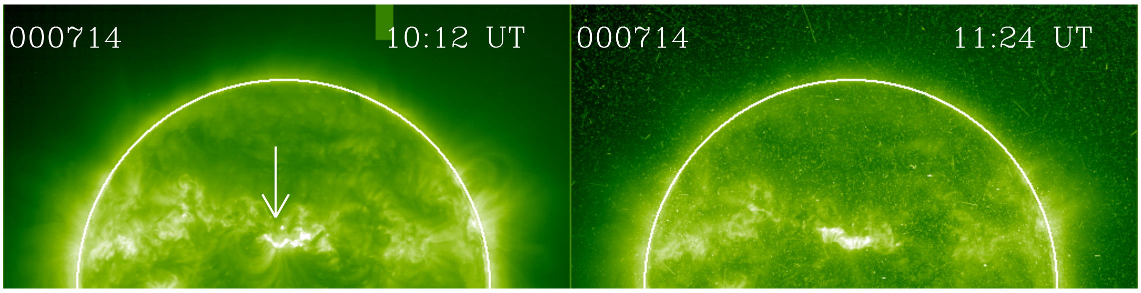

Figure 1.2: Images taken by EIT at 195 Å showing the formations of the post-eruptive arcade on 14-July-2000. The arrow in the left image shows the eruption site. In the images north points upward and west towards the right. Courtesy: SoHO/EIT consortium.

or reverse S-shaped ($\sim 2\times10^6$ K) coronal loop structures, called sigmoids, was found to preceed some CMEs (e.g., Rust and Webb 1977; Svestka et al. 1998; Hudson et al. 1998). Contrary, after some CMEs transient large-scale loop systems, commonly called post-flare loops (PFLs) or post-eruptive arcades (PEAS), were visible in soft X-ray and EUV wavelengths (e.g., Sterling et al. 2000). Fig. 1.2 displays an example of a PEA detected by EIT at 195 Å on 14-Jul-2000 in the course of a CME detected by LASCO/C2.

Presently, SoHO (Domingo et al. 1995) provides an unprecedented opportunity to study the transient processes in the low and outer corona based on the high spatial and temporal resolution of the *Extreme-ultraviolet Imaging Telescope* (EIT, Delaboudiènere et al. 1995), *Large Angle Spectrometric Coronagraph* (LASCO, Brueckner et al. 1995) and *Michelson Doppler Imager* (MDI, Scherrer et al. 1995) instruments and because of its uninterrupted view towards the Sun from the L1 point of the Sun-Earth-System, 1.5×10^6 km ahead of Earth. Ground-based Hα observations and X-ray data taken by the *Geostationary Operational Environmental Satellites* (GOES) and *Soft X-ray Telescope* (SXT, Tsuneta et al. 1991) aboard *Yohkoh* complement the SoHO observations.

The major goals of this thesis are to help identify the source regions of CMEs in the low corona and photosphere through EUV and MDI observations and to study the evolution of the photospheric magnetic field underlying them, possibly yielding information on the CME's energies, directions of propagation, magnetic configurations and onset causes.

Chapter 2 provides a brief overview about the main physical properties of the solar atmosphere followed by a review on CME properties and models in Chapter 3. Chapter 4 briefly outlines the specifications of the SoHO instruments used for the study. The techniques of data analysis applied in this thesis are illustrated in Chapter 5. Chapter 6 summarizes the basic physical properties of PEAs in the studied part of solar cycle 23 as deduced from a systematic analysis of EUV measurements. Their association to white-light CMEs is discussed in Chapter 7. Chapter 8 presents the discovery of a post-CME inflow above a post-eruptive arcade. Chapter 9 provides a detailed study of the evolution of the photospheric magnetic field in the source regions of a selected subset of events. The major results and conclusions are summarized in Chapter 10, including a perspective for future research.

2 The Sun and its Atmosphere

Observations over several centuries have revealed the dynamic nature of the solar atmosphere. This chapter illustrates the basic structure of our Sun and its atmosphere, with special emphasis on the solar corona.

2.1 Introduction

Altogether there are about five-thousand stars visible to naked eye in the entire celestial sphere. There are hundreds of billions of stars in the Milky Way. Our Sun is just one such star. Our existence and sustenance is inherent to the Sun. Although it is on average 150 million kilometers away, it is the only star which can be studied in detail using ground- and recently space-based observations, e.g., German Vacuum Tower Telescope at the Observatorio del Teide at Tenerife, Solar and Heliospheric Observatory (SoHO), Transition Region And Coronal Explorer (TRACE).

The Sun is an ordinary main sequence star of spectral type G2. There are many stars which are much hotter or much cooler than the Sun. The Sun is mostly made up of hydrogen (92.1%), helium (7.8%) and other heavy elements like carbon, nitrogen, oxygen, neon, magnesium, silicon and iron. The Sun is a sphere of hot plasma. A plasma is a gas of sufficiently high temperature at which atoms are stripped of some or all their electrons to enable the gas to conduct electric current. The plasma is gaseous on and near the surface and gets denser towards the core. The Sun's interior basically consists of the core, the radiative zone and the convective zone. The atmosphere consists of the photosphere, the chromosphere, the transition region and the corona. Fig. 2.1 illustrates the different layers of the Sun. Some special features e.g. a flare, sunspots, the photosphere, the chromosphere, the corona, a coronal hole and a prominence are clipped from actual solar images taken by different instruments aboard SoHO (see Chapter 4). The basic physical parameters of the Sun are provided in Table 2.1.

2.2 Solar Interior

The solar interior can be divided in three basic parts: the core (containing about 10% of the mass of Sun), the radiative zone and the convective zone. The solar core is defined as the region where the temperature is high enough to enable the hydrogen fusion reaction. Here hydrogen fuses into helium and produces an enormous amount of energy. It is transported out through two spherical shells. The inner shell is called

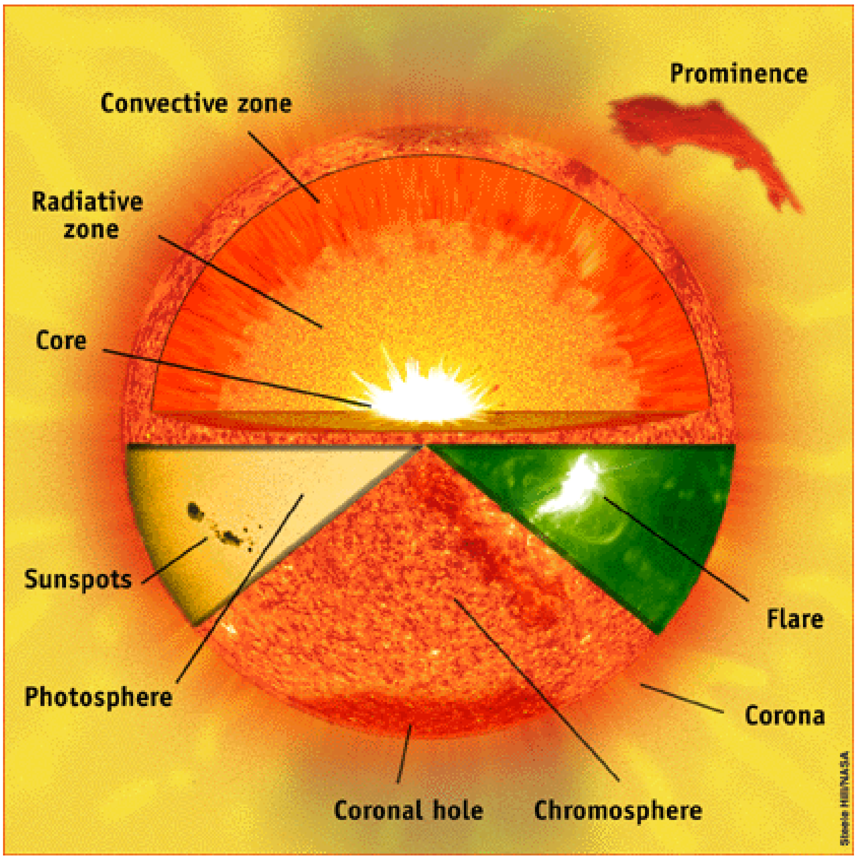

Figure 2.1: Six layers of the Sun shown in different colors. Courtesy: SoHO Consortium.

radiative zone and the outer shell is called the convective zone. Mechanisms of heat transfer in these shells are radiation and convection respectively. The radiative zone extends from the core boundary out to ∼0.7 $R_\odot$. Above this height the convection mechanism dominates over the radiation mechanism. The convection zone is a layer starting from the upper boundary of the radiative zone to the lower boundary of the photosphere. In the convection zone, also termed as sub-photospheric zone the generation of magnetic fields takes place. In the convection zone bubbles of gas which are hotter than their surroundings are buoyant and rise, whereas bubbles which are cooler than their surroundings, sink. Statistically there is no net transport of mass by the rising and sinking bubbles, but there is a net transport of heat (convective transport). The granular appearance of the Sun in visible light provides observational evidence for such convective motions in the outer layer of the Sun.

2.3 Solar Atmosphere

The atmosphere of the Sun is composed of different layers of hot plasma and gases threaded by magnetic fields. They differ greatly from each other in terms of their physical characteristics. Starting from the visible solar surface, these layers are the *photosphere*, the *chromosphere*, the *transition region* and the *corona*.

Table 2.1: Basic physical parameters of Sun (after Lang 2001)

Name	**Sun**
Parent galaxy	Milky Way
Type	Fixed Star
Spectral type	G2
Magnitude	4.8
Mean distance to Earth	149,589,000 km = 1 AU
Radius ($R_{\odot}$)	696,000 km i.e. 109 R_e
Total mass ($M_{\odot}$)	1.989×10^{30} kg
Density (average)	1.409 g cm^{-3}
Surface temperature	5800 K
Rotation duration	27.25 days (synodic) at equator 25.38 days (sideric) at equator
Age	4.60 billion years
Among neighbor star	α Centauri, at 4.37 lightyears
Next neighbor galaxy	Magellan's Clouds, at 165,000 lightyears
Earts's distance variations	± 1.69 % (+ in July, − in January)
Apparent diameter	31' 59.3"= 1913.3" i.e. 0.5 degree
Apparent radius	959.65" i.e. 1000 arcsec 1 arcsec on Sun from Earth=725 km
Energy output	3.82×10^{26} Watt

2.3.1 The Photosphere

The visible disk of the Sun recognized as the so called "solar surface" may be considered as the base of the photosphere. This is the lowest and densest part of the atmosphere with a thickness of about 400 km. The effective temperature of the photosphere is about 5800 K and the density is about 10^{-6} g/cm^3. As we move out from the bottom of the photosphere towards the chromosphere the temperature and density both decreases. The temperature becomes minimum ($\sim$ 4500 K) at the top of the photospheric layer. Observed photospheric phenomena are sunspots, granules, super-granules, faculae.

2.3.2 The Chromosphere

The layer with a thickness of $\sim$2500 km above the photosphere is called the chromosphere. The Sun's chromosphere starts from a temperature of about 4500 K at the top of the photosphere. The chromosphere is very faint because the atmosphere becomes transparent (optically thin) in the continuum spectrum. The chromosphere can be observed during total solar eclipses when the moon blocks the overwhelming photospheric light from the visible solar disk. Then a narrow rose-colored band at the limb of the Sun can be seen which gave it the name chromosphere. The chromosphere is optically thick in strong resonance lines such as Hα and CaII K. The most prominent chromospheric features are filaments, prominences, spicules, the chromospheric network associated with the boundaries of super-granular cells. Filaments and prominences are the same phenomena seen from different perspectives and with different background. Filaments are seen against the bright disk in absorption whereas prominences are seen at the limb against dark space in emission.

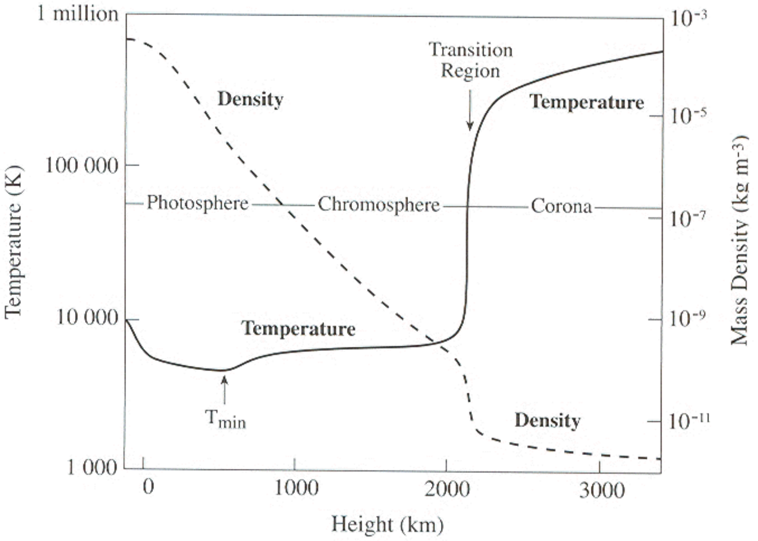

Figure 2.2: Temperature and density profile of the solar atmosphere (Adopted from Lang 2001).

2.3.3 Transition Region

The transition region is considered to be the interface between the cooler chromosphere and the million degree corona. This is the region where the temperature and density changes drastically, as is illustrated in Fig. 2.2. Starting from the photosphere, the temperature decreases slowly up to the bottom of the chromosphere. It slowly increases in the chromosphere before a drastic increase in the transition region takes place. In the transition region the temperature increases abruptly from 10000 K to some million degree Kelvin. Conversely, the density decreases abruptly from the photosphere to the corona.

2.3.4 The Corona

The corona is the extended solar atmosphere above the transition region. Sometimes the transition region may be referred to as the 'low corona'. The corona can only be observed during a total solar eclipse or by means of a coronagraph. A coronagraph is an instrument designed to create an artificial eclipse through blocking out the photospheric light. Fig. 2.3 displays images of the solar corona during a solar eclipse taken at solar activity minimum (top panel, 1994) and solar activity maximum (bottom panel, 1980). The solar activity is explained in section 2.5. The images shown in Fig. 2.3 reveal a highly structured and differently shaped corona. At minimum solar activity, the corona is mainly elongated along the solar equatorial direction. In contrast, the corona has a more spherically symmetric appearence at maximum solar activity. From the eclipse observations it is known that the corona changes it's structure from minimum to maximum.

White-light Corona:

The visible coronal radiation is primarily composed of two different parts: the *K-corona* and the *F-corona*. The K-corona derives its name from the German “Kontinuum”. Its continuum spectrum resembles the photospheric spectrum without the Fraunhofer lines (absorption lines). The K-corona is produced by Thomson scattering of photospheric light by coronal electrons. The thermal electron velocity is 1/60 the speed of light, so that broadening of Fraunhofer lines is 1/60 of their wavelength and they are all washed out. Since it is produced by Thomson scattering of photospheric light by free electrons in the corona, the light of the K-corona is highly

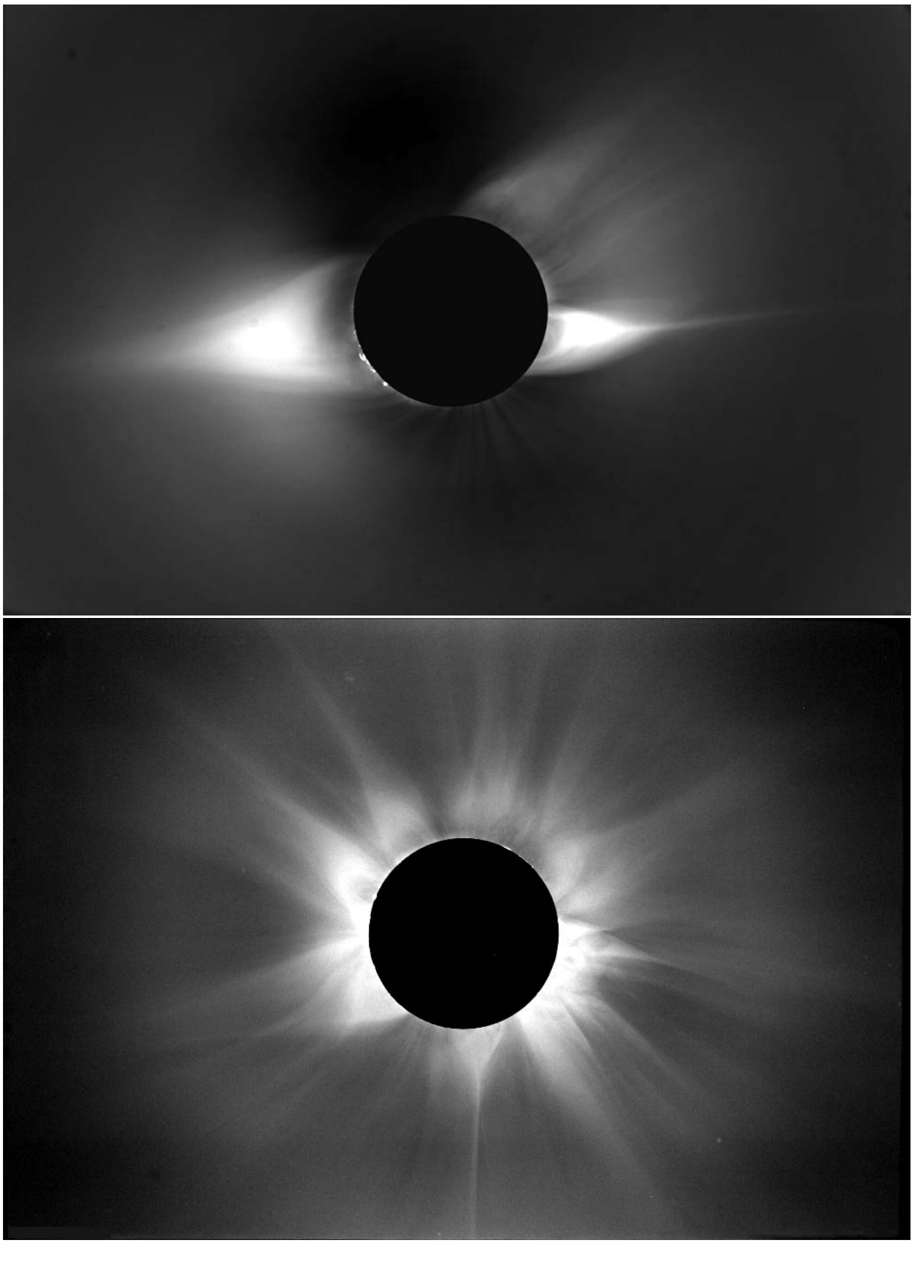

Figure 2.3: Images taken during the total solar eclipse on 03-Nov-1994 i.e. at solar minimum (top panel) and on 16-Feb-1980 i.e. at solar maximum (bottom panel). Courtesy: HAO/NCAR.

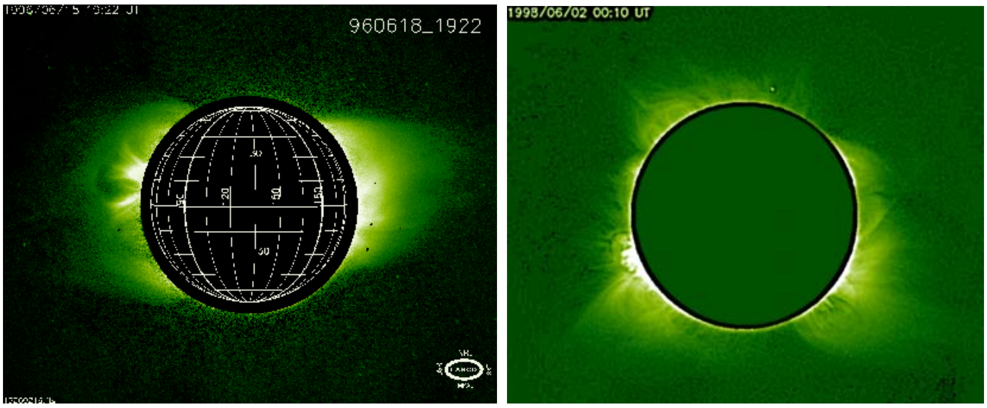

Figure 2.4: Images of the solar corona taken by the LASCO/C1 coronagraph aboard SoHO. The left image shows the corona at times of solar minimum on 18-Jun-1996. The right image displays the corona around solar maximum taken on 02-Jun-1998. The images are taken at green line (5303 Å). Courtesy: M. Mierla.

polarized. The K-corona extends between $\sim 1.03 R_{\odot}$<R<2.5 $R_{\odot}$.

The F-corona, dominant at distances of R>2.5 $R_{\odot}$, displays the Fraunhofer lines superimposed on the continuum solar spectrum. The prefix *F* is dedicated to Fraunhofer. The spectrum of the outer corona also resembles the photospheric spectrum, and is weakly polarized. The spectrum of the F-corona is mainly produced by the photospheric light scattered by dust particles into the interplanetary space. The F-corona together with the K-corona constitute the white-light corona which merges into interplanetary space with decreasing brightness.

Emission Corona or E-Corona:

In the optical range of the coronal spectrum, about two dozen emission lines were found to be superimposed on the continuous background. These emission lines are formed by highly ionized atoms implying million degree coronal temperatures. The strongest observed emission lines of the E-corona are λ 5303 Å (Fe XIV) (see Fig. 2.4) and λ 6374 Å (Fe X). The formation of these lines in the coronal spectrum yield two definite informations about the physical state of the coronal gas. First, that the gas density is very low (at the order of 10^6-10^8 cm^{-3}) and second, the temperature of the corona is extremely high ($\sim 2\times10^6$K).

Ultraviolet and X-ray Corona:

Because of the high temperature of the corona, it radiates strongly in the ultraviolet and soft X-ray energy range. Figure 2.5 shows an image (left panel) taken by the Soft X-ray Telescope (SXT) aboard Yohkoh and an EUV image (right panel) taken by the Extreme-ultraviolet Imaging Telescope (EIT) aboard SoHO at 195 Å emission lines.

The brightness difference in the images taken at EUV and X-ray wavelenghts is due to different coronal densities and temperatures. The emission intensity depends on the electron number density N_e and temperature T of the plasma by the relation given by, N_e^2 exp($-$hν/kT), where ν is the frequency of light and k is Boltzmann's constant. Because of this dependence the images taken at X-rays and at EUV wavelengths enhance the actual temperature and density contrast.

The Radio Corona:

At larger wavelengths the radio emission of the Sun is dominated by various types of *radio bursts*. These radio bursts can be used as a probe for the solar corona because in a coronal plasma electromagnetic waves can not propagate if their frequency lies below the *plasma frequency*. The plasma frequency is given by

$$\nu_p = \frac{e}{2\pi}\left(\frac{n_e}{\varepsilon_0 m_e}\right)^{1/2}; \nu_p[kHz] = 9 \times \sqrt{n_e[cm^{-3}]}$$

Where n_e = electron density, electrons m^{-3}
ν_p = plasma frequency, Hz
ε_0 = permittivity of vacuum (= 8.85 × 10^{-12} farad m^{-1})
m_e = mass of electron (9.1 × 10^{-31} kg)
e = charge of electron (=1.6 × 10^{-19} coul)

Where, the electron number density n_e in terms of the distance from the center of the Sun is given by (Allen 1947):

$$n_e = (1.55r^{-6} + 2.99r^{-16}) \times 10^{14}$$

Where r = distance from center of the Sun in solar radii.

Waves with frequencies lower than the plasma frequency will either be absorbed or reflected. In the corona the electron density decreases with distance from the Sun. Therefore the radio signals with longer wavelength must arise from sources which lie further outwards than the sources of short-wavelength signals.

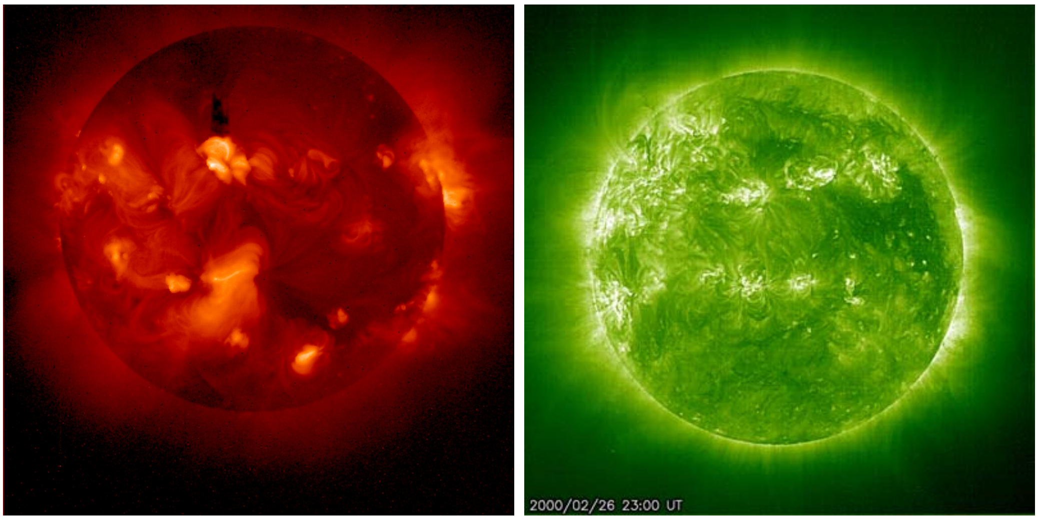

Figure 2.5: Left image taken by the soft X-ray Telescope aboard Yohkoh. Right image is taken by the Extreme-ultraviolet Imaging Telescope aboard SoHO at 195 Å. Courtesy: Yohkoh and SoHO/EIT teams.

2.4 The Structure of the Solar Corona

The structures in the solar corona can be basically divided into three zones: 1) active regions, 2) quiet Sun regions, 3) coronal holes (e.g., Aschwanden 2004). Active regions are located in the areas of strong magnetic field concentrations, visible as sunspots in optical wavelengths or magnetograms. Sunspots typically exhibit a strongly concentrated magnetic flux of the leading magnetic polarity, followed by a more fragmented trailing area of opposite magnetic polarity. Because of the bipolar nature of the field active regions are mainly made up of closed magnetic field lines connecting both polarities. A consequence of plasma heating in the chromosphere are permanent upflows of plasma into coronal loops, which give active regions the familiar appearence of numerous loops filled with heated plasma, which are hotter and denser than the surrounding corona, producing bright emission in soft X-rays and extreme ultraviolet (EUV) wavelengths. In the Yohkoh soft X-ray image shown in Fig. 2.6 active regions appear bright. The heliographic positions of active regions is typically confined in bands located at latitudes of ±40° with respect to the solar equator.

Historically, the remaining areas outside active regions were defined as the quiet Sun regions. However many dynamic processes have recently been discovered all over the solar surface. The distinction between active regions and quiet Sun regions becomes thus more and more blurred because most of the large scale structures that overarch quiet Sun regions are rooted in active regions. A good definition is that quiet Sun regions encompass all closed magnetic field regions (excluding active regions), clearly de-marketing the quiet-Sun territory from the coronal holes, which encompass open magnetic field regions (Aschwanden 2004). The quiet Sun regions in the corona appear less bright in the soft X-ray image shown in Fig. 2.6.

During solar eclipses the northern and southern polar zones of the solar globe

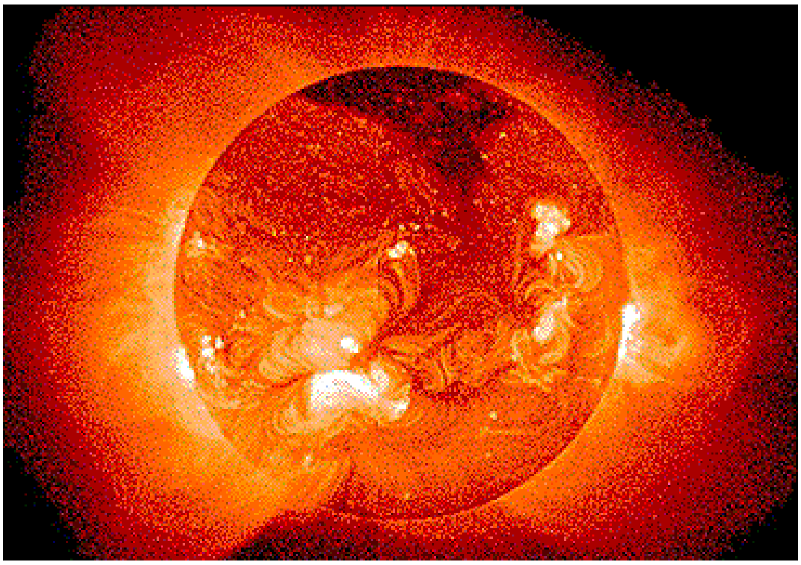

Figure 2.6: Soft X-ray image of the solar corona recorded on 26-Aug-1992 by Yohkoh's soft X-ray Telescope (SXT). Courtesy: Yohkoh team.

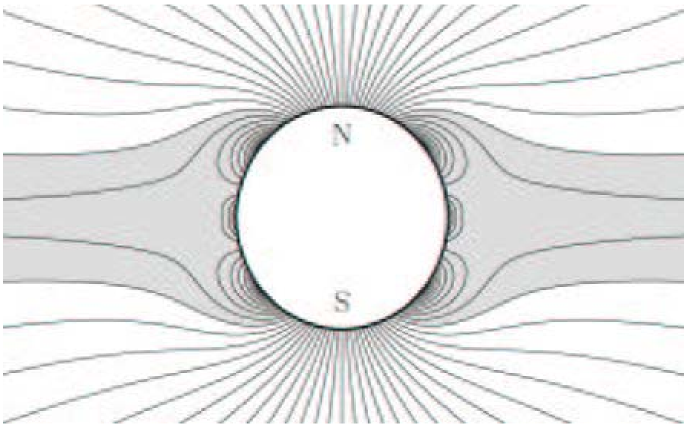

Figure 2.7: Schematic representation of the magnetic field structure of the corona arounds times of solar minimum (Adopted from Aschwanden 2004).

have generally found to be darker than the equatorial zones. Max Waldmeier thus called those zones as ”Koronale Löcher” (in German), i.e., coronal holes (e.g., Aschwanden 2004). These zones are dominated by open magnetic field lines, that act as efficient conductors for flushing heated plasma from the corona into the solar wind. Because of this efficient transport mechanism, coronal holes are most of the time ”empty” and thus appear darker than the quiet-Sun. Two polar coronal holes (northern and southern) can be seen in Fig. 2.6.

On the global scale, there are two different magnetic zones in the corona with fundamentally different physical properties: The open and closed field regions (compare with Fig. 2.7). Open field regions exist primarily in the polar regions. They are the source regions of the fast solar wind ~ 800 km/s. A consequence of the open field configuration is efficient plasma transport out into the heliosphere whenever

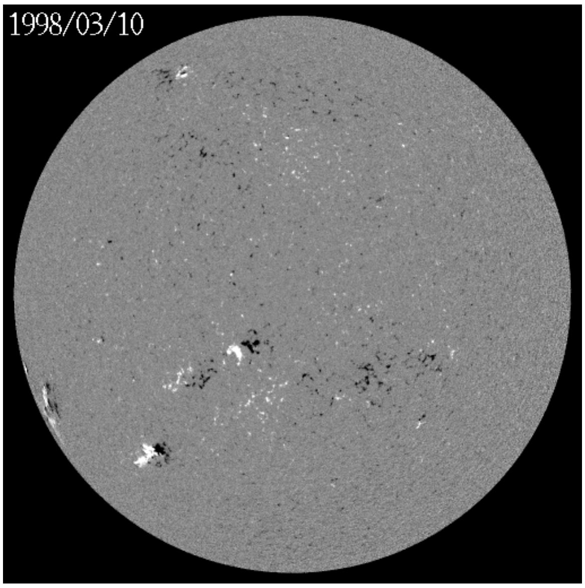

Figure 2.8: Magnetogram taken by SoHO/MDI on 10-Mar-1998. Courtesy: SoHO/MDI consortium.

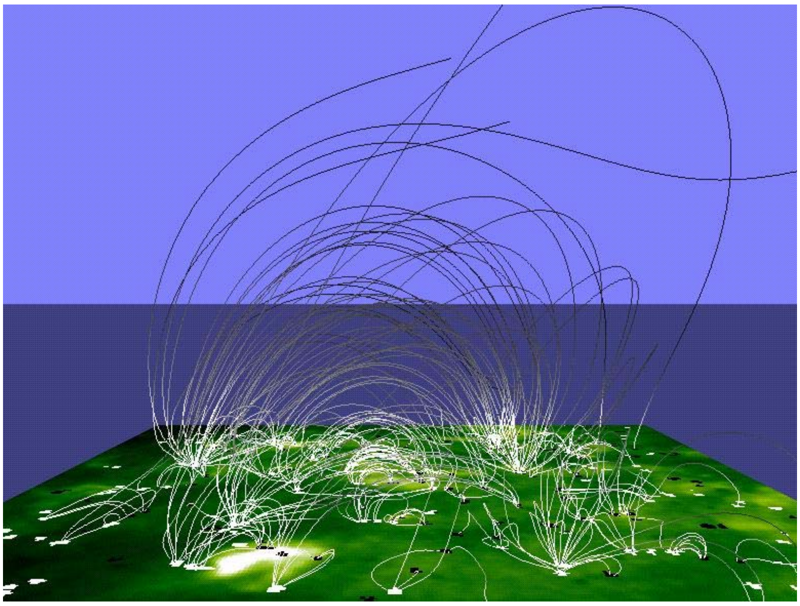

Figure 2.9: Magnetic field extrapolation from the photosphere to the corona based on the MDI magnetograms and EIT images obtained on 19-Oct-1996. Courtesy: Stanford LMSAL.

chromospheric plasma is heated at the foot-points. In contrast, closed field regions comprise mostly the closed loops in the solar corona up to heights of one solar radius. The outer parts open up at higher altitudes and connect eventually to the heliosphere producing a slow solar wind component of $\sim$ 400 km/s. It is closed field regions that contain all the bright and dense coronal loops, produced by filling with chromospheric plasma that stays trapped in these closed magnetic loops.

The magnetic field arising from the solar surface is very inhomogeneous. The strongest magnetic field regions are concentrated in sunspots, having field strength of $\sim$ 2000 - 3000 G. Active regions and their plages comprise a large area around sunspots, with average photospheric field of $\sim$ 100 - 300 G. The background magnetic field in the quiet Sun and in coronal holes has a net field of 0.1 - 0.5 G, while the absolute field strength in resolved elements amounts to 10 - 50 G (e.g., Aschwanden 2004).

The observed coronal features in EUV and X-rays can be compared with photospheric magnetograms. A magnetogram taken by the Michelson Doppler Imager (MDI) aboard SoHO is shown in Fig. 2.8. The white color corresponds to regions of positive magnetic polarity, i.e. magnetic field lines pointing away from the Sun, and the black color represents regions of negative magnetic polarity, i.e. field lines pointing towards the Sun. The regions in the magnetogram where the black and white color are concentrated are commonly known as active regions with higher magnetic field strengths. However, there are many tiny bipolar regions on the solar disk where black and white dots are seen. Comparison of the EUV data taken from the Extreme-ultraviolet Imaging Telescope (EIT) aboard SoHO with the MDI magnetogram show that all these small dots seem to be the foot points of magnetic field loops. Fig. 2.9 represents a model of the magnetic field lines from the surface of the Sun developed by combining data from MDI and EIT and is referred to as the magnetic carpet. The data were taken on 19-Oct-1996. The white magnetic field lines emanate from the magnetic carpet and form arches from one magnetic polarity (white) to the other (black). Current theories predict that length and curvature of these arches determine the degree to which they are heated (Aschwanden 2004). The image underlying the arches shows the intensity enhancement observed at the same time by EIT in the Iron line at 195 Å, with bright green corresponding to relatively hot regions and dark green corresponding to cooler ones.

2.5 The Solar Activity Cycle

It is well known that the number of sunspots and active regions on the Sun is varying. The obvious variations are caused by the Sun's rotation (sunspots disappear from view and then re-appear), and over time new sunspot groups form and old ones decay and fade away. The solar magnetic cycle was discovered based on the increase and decrease of sunspots. The orientation of the magnetic field in the active regions was found to be opposite in the northern and southern hemisphere (e.g., Hale et al. 1919). The orientation of the global polarity changes about every 11 years which is called the solar cycle. A complete magnetic reversal takes place every $\sim$ 22 years which is known as *Hale's cycle* (Hale et al. 1919). During a 11 year cycle, the zones of sunspot appearances migrate from higher latitudes towards the equator giving rise to the well known *butterfly* diagram (see Fig. 2.10), also known as *Spörer's* law.

During the solar cycle of about 11 years, the total radiation output changes dramatically in X-ray, hard X-ray and radio wavelengths. The total magnetic flux of active regions observed at the photosphere reaches a peak intensity during solar maximum and drops to a lower level during solar minimum (see. Fig. 2.11, left panel). The magnetic flux varies during the solar cycle by a factor of ≈ 8 in active regions and by a factor of ≈ 2 in ephemeral regions (e.g., Hagenaar et al. 2003). Ephemeral regions are the small-scale magnetic flux concentrations found outside active regions (Martin and Harvey 1979). Due to direct coupling of the radiation mechanisms to the dissipation of the magnetic energy (Fisher et al. 1998; Benevolenskaya et al. 2002) and related plasma heating, the total output radiation in these wavelengths is modulated correspondingly from solar maximum to solar minimum (see Fig. 2.11, right panel).

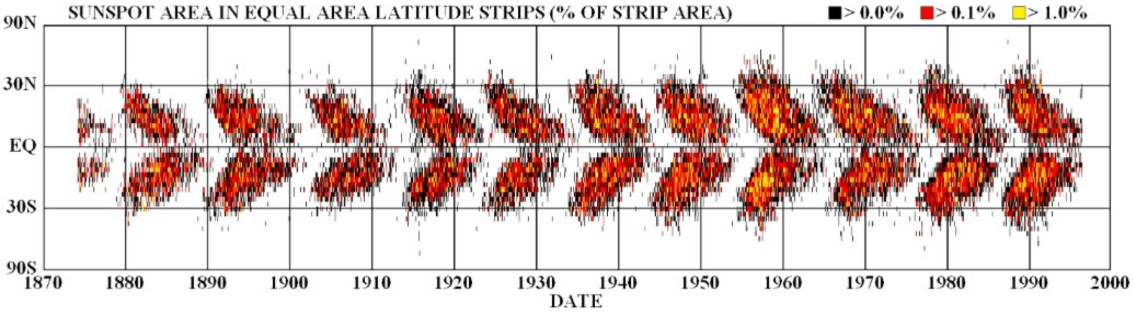

Figure 2.10: A butterfly diagram of the latitudes of sunspot occurrences versus time. Courtesy: MSFC.

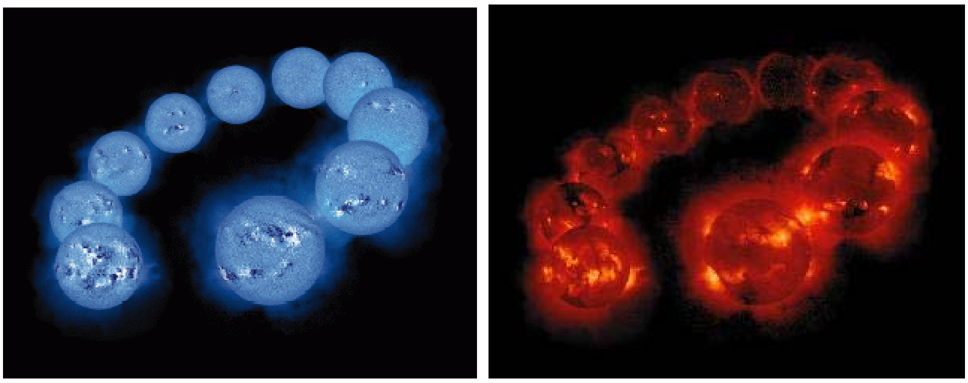

Figure 2.11: Changes in the solar corona as observed in photospheric magnetic field and X-ray over the solar cycle. Courtesy: KPNO and Yohkoh team.

The evolution of the sunspots over the solar cyclic period can be explained in terms of the global solar magnetic field changes. According to Babcock (1961), the global solar magnetic field evolves from an initial poloidal field to a toroidal field under the influence of solar differential rotation. However, in the recent scenarios, the solar cycle is caused by a process called *solar dynamo* which is driven by the internal magnetic field at the bottom of the convection zone. A strong field of about 100,000 G at the bottom of the convection zone is periodically strengthened and weakened. From this magnetic field, buoyant magnetic flux-tubes arise and emerge to the photosphere (Aschwanden 2004). The new emerging fields then shear into a more toroidal fields due to differential rotation, until surface diffusion by granulation breaks up the field. The fragments of the magnetic fields are then transported towards the poles due to meridional flows. The toroidal field component diffuses increasingly during the decay of the cycle. Consequently, a weak poloidal global field is left at solar minimum. When the field at the bottom of the convection zone strengthens by the action of the internal solar dynamo process, the rate of buoyant flux-tube increases and the next cycle starts (Aschwanden 2004).

3 Coronal Mass Ejections

Coronagraphic observations taken with a cadence of several minutes reveal the outward motion of new material in the corona termed as a coronal mass ejection (CME). This chapter provides a brief introduction to the basic physical properties of CMEs and their associated solar activity features. The attempts to describe the theoretical concepts of coronal mass ejections are briefly summarized.

3.1 Introduction

Inspecting the Sun, we observe basically two forms of mass loss: the steady solar wind outflow and the sporadic ejection of large plasma structures, termed *coronal mass ejections*, in short CMEs. CMEs are one of the most spectacular and striking manifestation of solar activity seen in the corona. Observation of CMEs has become possible only by means of a coronagraph which provides artificial total solar eclipses by blocking the overwhelming photospheric light. CMEs were first discovered through observations made by space-borne coronagraph aboard the *Orbiting Solar Observatory* (*OSO)-7* in 1973 (Tousey et al. 1973). They were detected on a more routinely basis during the *Skylab* mission in 1973-1974 (MacQueen et al. 1974).

From an observational point of view, a CME is defined as an observable change in the coronal structure that (1) occurs on a time-scale between a few minutes and several hours and (2) involves the appearence and outward motion of a new, discrete, bright, white-light feature in the coronagraph field of view (Hundhausen et al. 1984; Schwenn 1996).

The *Solwind* coronagraph (Michels et al. 1980) on board *P78-1* and the Corona/Polarimeter (C/P) on board the *Solar Maximum Mission* (*SMM)* in 1984-1989 (MacQueen et al. 1980) provided valuable data advancing the research on the physics of CMEs. The FOV (Field of View) of the *Solwind* coronagraph was 2.5-10 $R_\odot$ measured from the Sun's center with a resolution of 75 arcsec per pixel. The C/P instrument had a resolution of 10 arcsec per pixel and a FOV of 1.6-6.0 $R_\odot$. Presently, coronal mass ejections are continuously observed in white-light by the Large Angle Spectrometric Coronagraph (LASCO) aboard the *Solar and Heliospheric Observatory* (SoHO, Domingo et al. 1995) with unprecedented spatial (11.2 arcsec per pixel) and temporal resolution (20 minutes, Brueckner et al. 1995).

An example of a CME is shown in Fig. 3.1 taken by the LASCO/C3 coronagraph on 29-Mar-1998. The CME first appeared in the LASCO/C3 field-of-view (FOV) at

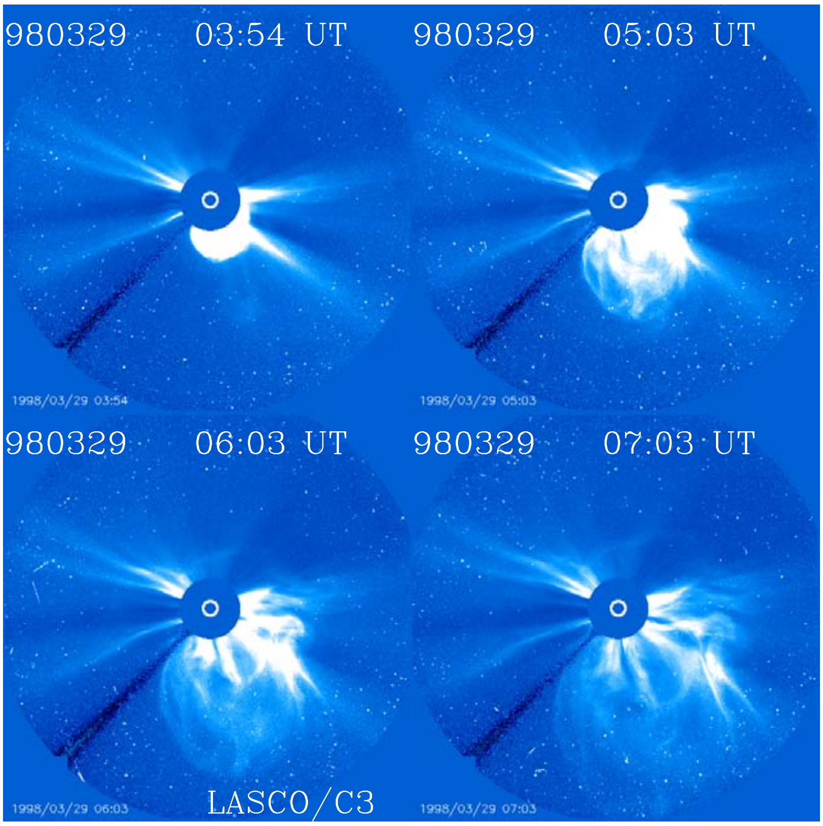

Figure 3.1: Series of LASCO/C3 white-light images taken on 29-Mar-1998 showing the evolution of a coronal mass ejection. The CME appeared in the LASCO/C3 FOV at 03:54 UT (top left panel) and evolved in the outer corona during the next three hours. Courtesy: SoHO/LASCO consortium.

03:54 UT and propagated outward with a speed (obtained from the CME catalogue[1]) of $\sim$ 1400 km/s.

The phenomenon of a CME consists of the ejection of hot ionized gas from the gravitational field of the Sun in the presence of magnetic fields. Though, the magnetic field in CMEs can not be directly observed, the high electrical conductivity in the ionized coronal plasma, according to Alfvén's theorem (Alfvén 1942), ensures to first order that the field is frozen into the plasma. Hence the magnetic field lines move with the plasma. Thus coronagraph observations of a changing coronal density structure provide informations about the geometry and evolution of the magnetic lines of force.

3.2 Observed properties of CMEs

Several basic properties of CMEs have been inferred on the basis of the measurements performed by Skylab, SMM, Solwind and presently by the LASCO coronagraphs on board SoHO. In the following sub-sections the basic properties will be summarized.

---

[1] http://cdaw.gsfc.nasa.gov/CME_list/

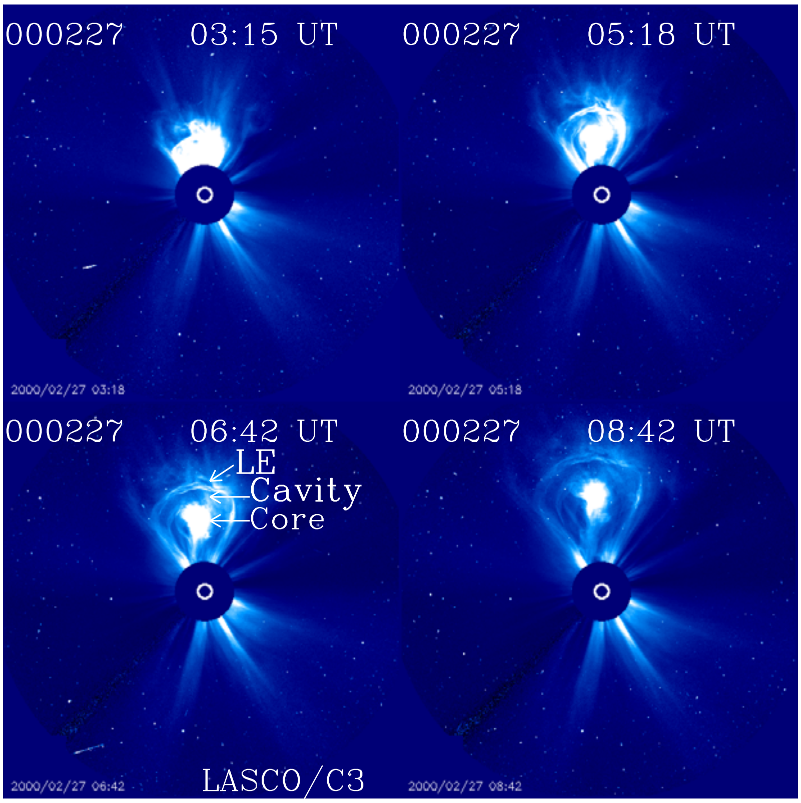

Figure 3.2: Series of LASCO/C3 images showing the evolution of a white-light CME on 27-Feb-2000. The CME reveals a three part structure: a leading edge, a dark cavity and a bright core. Courtesy: SoHO/LASCO consortium.

3.2.1 Shape and Geometry

Images obtained by a coronagraph depend on the density distribution of the plasma along the line-of-sight (LOS). Therefore, the visual appearence of a CME in coronagraphic images is related to the spatial distribution of free electrons in the corona. Since the corona is optically thin in the visual wavelengths, the radiation recorded at a point in the coronagraphic image is an integral of Thomson scattered light along the entire LOS extending through the corona until the instrument. In the images obtained by the coronagraph, the true three-dimensional density structures are projected onto two dimensions, hence the geometric interpretation of CMEs is complicated.

The results of the visual appearances of CME are summarized based on the observations made by different instruments e.g., for the *Skylab* data by Munro & Sime (1985), for *Solwind* data by Sheeley et al. (1982) and Howard et al. (1984, 1985) and for *SMM* data by Burkepile & St. Cyr (1993).

In the common observations there are basically two kinds of appearances of CMEs. The ones which originate from the solar limb, called limb CMEs. They propagate perpendicular to the LOS. Those CMEs which originate from the disk center, called halos (Howard et al. 1982) which propagate parallel to the LOS. The structure of limb CMEs (see Fig. 3.2) are better observed. They often appear as three-part structured entities with bright frontal loops known as *a leading edge, a*

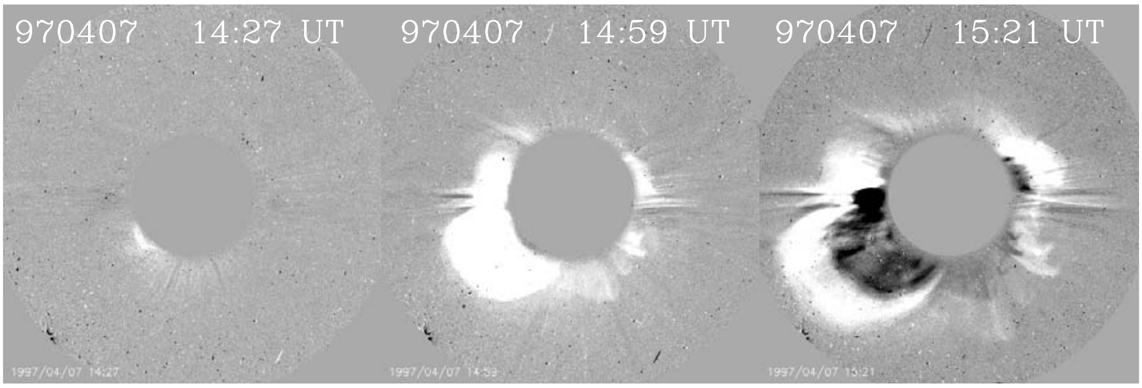

Figure 3.3: Running difference images of a halo CME on 07-Apr-1997 detected by LASCO/C2. The CME appeared first in the LASCO/C2 FOV at 14:27 UT. It propagated covering almost the complete coronagraph FOV. Courtesy: SoHO/LASCO consortium.

dark cavity and *a bright core*. Figure 3.2 shows an example of a typical three-part structured CME imaged by the LASCO/C3 coronagraph aboard SoHO on 27-Feb-2000. However, CMEs originating near the disk center appear unstructured covering the occulter either partially or fully as they propagate parallel to the LOS and are called *halos* (e.g. Fig. 3.3).

3.2.2 Physical Parameters

Speed of CMEs

The speed of CMEs and their acceleration over the first solar radii outward have been analyzed by several authors based on different space-based instruments (e.g., Gosling et al. 1976; Howard et al. 1985; Hundhausen et al. 1994; St. Cyr et al. 2000; Gopalswamy et al. 2003). The speeds of CMEs cover a broad range between 50-3000 km/s with an average value of ∼400-500 km/s. The speed of slow solar wind in the corona is of about 300-400 km/s and of the fast solar wind is about 750 km/s. The sound speed at a typical coronal temperatures of about 1.5-2.0 MK is at around 175 km/s. Hence the speed range of CMEs suggests that many CMEs travel with super-sonic speed (Sheeley et al. 1999).

Table 3.1: Average observed properties of coronal mass ejections (After: Gosling et al. 1976 (from skylab); Howard et al. 1985, 1986 (from SOLWIND); Hundhausen 1993, 1994 (from SMM) and Gopalswamy et al. 2003 (from LASCO)).

Parameter (Average values)	Skylab (1973-74)	SOLWIND (1979-80 & 1984-85)	SMM (1980, 1984-89)	LASCO (1996-2002)
Angular Size(deg)	42	43	47	72
Speed (km/sec)	470	460	350	437
Mass (gm)	–	4.0×10^{15}	2.5×10^{15}	–
Kinetic Energy (ergs)	–	3.4×10^{30}	3.1×10^{30}	–

Angular Width of CMEs

The angular width of a CME is defined as the angle subtended by the two outer sides of a CME with respect to the center of the solar disk. The angular size of CMEs is sufficiently well defined at least for the limb CMEs. However, for halo CMEs the angular widths are overly estimated as they propagate in the LOS covering either partially or fully the coronagraphic FOV. An example for the measurement of the angular width of a CME width is shown in Fig. 3.4 taken from Cremades & Bothmer (2004). Table 3.1 presents the average angular width measured during different missions. The angular width based on *Skylab, Solwind, SMM, & LASCO* measurements was found to be very similar. A remarkable disparity in the angular width appears in the measurements of LASCO. This difference is very likely caused by many halo CMEs which were very often detected by LASCO coronagraphs compared to the previous observations due to its unique sensitivity. Usually halos are very hard to detect because the intensity of the Thomson scattered light is reduced for structures far from the plane of the sky (Plunkett et al. 1998; Thompson et al. 1998). The sufficiently improved sensitivity of LASCO over the previous coronagraphs made it possible to detect even very faint halo CMEs. Gopalswamy et al. (2003) showed that the measured average angular width of CMEs increased from solar minimum to solar maximum. They presented statistic (see Fig. 3.5) for the number of halo CMEs over the calender years 1996-2002. The figure reflects that the number of halos substantially increased around solar maximum. It is likely that the increase in the angular width is caused by the increase in the number of halo CMEs detected by the LASCO coronagraphs (Gopalswamy et al. 2003).

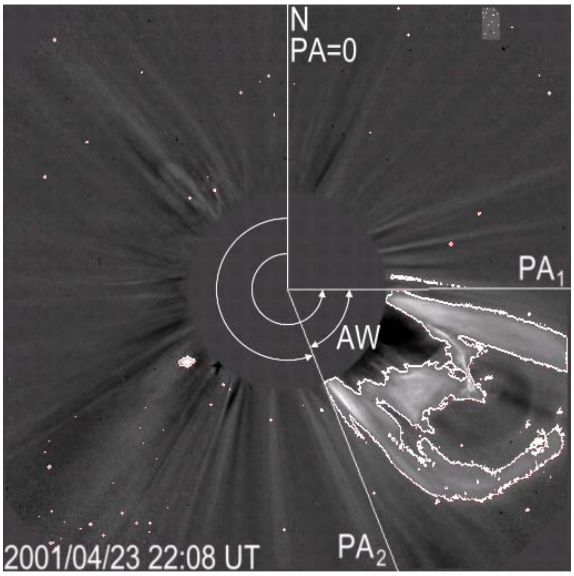

Figure 3.4: LASCO/C2 image of a CME, from which a pre-event image taken at 18:11 UT had been subtracted in white-light intensity. A white contour demarks the CME, demarked by the position angle of its two outer edges (PA1 & PA2), subtending its angular width (AW). Courtesy: Cremades & Bothmer 2004).

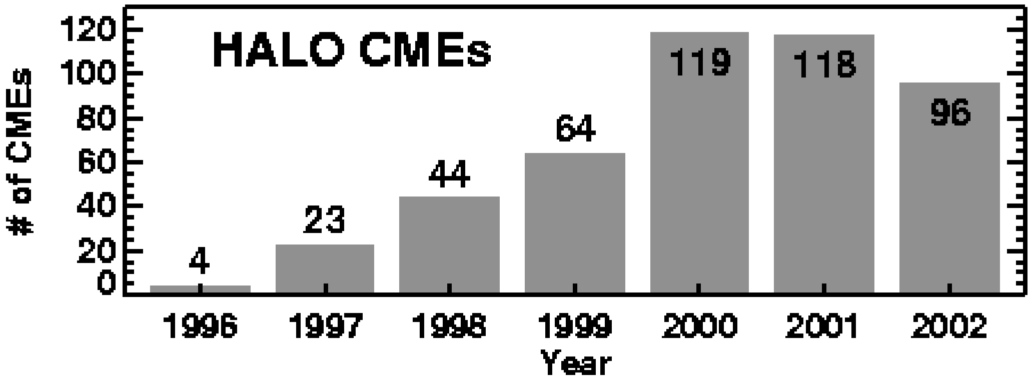

Figure 3.5: Frequency of halo CMEs for the period 1996-2002 (Gopalswamy et al. 2003).

CME Frequency

The number of CMEs observed per day varies substantially from solar minimum to maximum. The first space based coronagraph *OSO-7* detected 23 CMEs in total. Tousey et al. (1974) reported a rate of 0.5 CME/day at times close to solar minimum. Later on Hildner et al. (1976) estimated an average rate of one CME per day. Based on the complete data-set from *Skylab, SMM* and *Solwind* a detailed study of the CME rate was performed by Webb & Howard (1994). The long-term averaged CME rate obtained by Webb & Howard was similar to the one predicted by Hildner et al. (1976).

In the early phase of the SoHO mission (1996-1998), i.e. in the rising phase of solar cycle 23, the CME rate studied by St. Cyr. et al. (2000) based on the *LASCO* data was similar as to the earlier observations during the period of investigation. However, based on the complete data-set of LASCO from 1996-2002, Gopalswamy et al. (2003) found that the CME rate varies from less than one CME per day during solar minimum to slightly more than six CMEs per day during solar maximum. The estimated CME rate based on analysis of LASCO observations turned out to be much higher during times of solar maximum.

3.3 Source Regions of Coronal Mass Ejections

Since the first detection of CMEs in the 1970s, it is a big scientific challenge to understand how CMEs are intrinsically related with other forms of solar activity, e.g., active regions, sunspots, solar flares or prominence eruptions, since it was thought that this understanding will help answer the question how CMEs originate.

3.3.1 CMEs and Sunspots

The variations of CME frequency with respect to the solar cycle addresses the question of the relationship between CMEs and sunspots. Based on the Skylab CME data base, Hildner et al. (1976) found a correlation between the CME rate (R) and the sunspot number (N). The relation between the CME rate and sunspot number

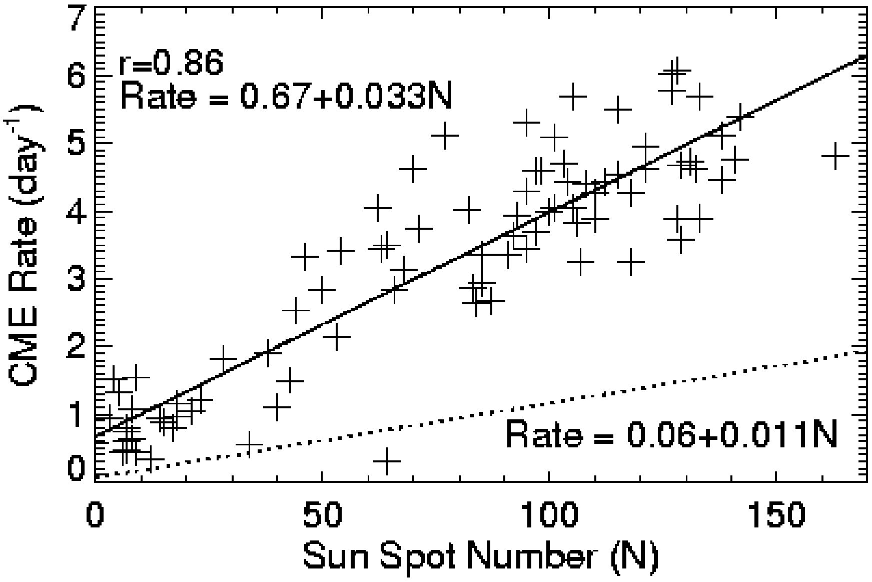

Figure 3.6: Scatter plot of CME rate against the daily sunspot number. The correlation coefficient was 0.86. The solid line is the regression line. The dotted regression line was adopted from Cliver et al. (1994) based on pre-SoHO data (Gopalswamy et al. 2003).

was given by R = 0.07 + 0.01 N for the observation period of 13.5 days. This relationship was further confirmed by Solwind and SMM observations (Webb & Howard 1994; Cliver et al. 1994). Based on the LASCO data taken between 1996-2002 Gopalswamy et al. (2003) found a correlation coefficient of 0.86 between CMEs and the sunspot number. The slope of the regression line obtained based on the LASCO data was found to be very different than that by Cliver et al. (1994). The difference can be attributed to the higher sensitivity and better dynamic range of the LASCO instrument.

Since not all the CMEs originate from active regions visible as sunspots, the correlation between CMEs and sunspots may improve if one takes only those CMEs into account which originate from active regions (Gopalswamy et al. 2003).

3.3.2 CMEs and Erupting Prominences/Disappearing Filaments

Hα images of the chromosphere reveal massive loops of cooler dense gas that arch up over the photosphere. Seen from above, they are elongated, dark features, called filaments, that stretch sometimes up to halfway across the entire visible solar disk. The cool gas looks dark against the hot Sun beneath it. When seen from the side at the edge of the solar disk these same features light up as bright bundle of loops called prominences. Basically two primary types of plasma motions have been recognized in prominences. One, with material streaming from one foot-point of the prominence to the other called *active prominences* and the other with prominence material leaving the Sun either partially or completely, known as *eruptive prominences* (Tandberg-Hanssen 1974, p. 2).

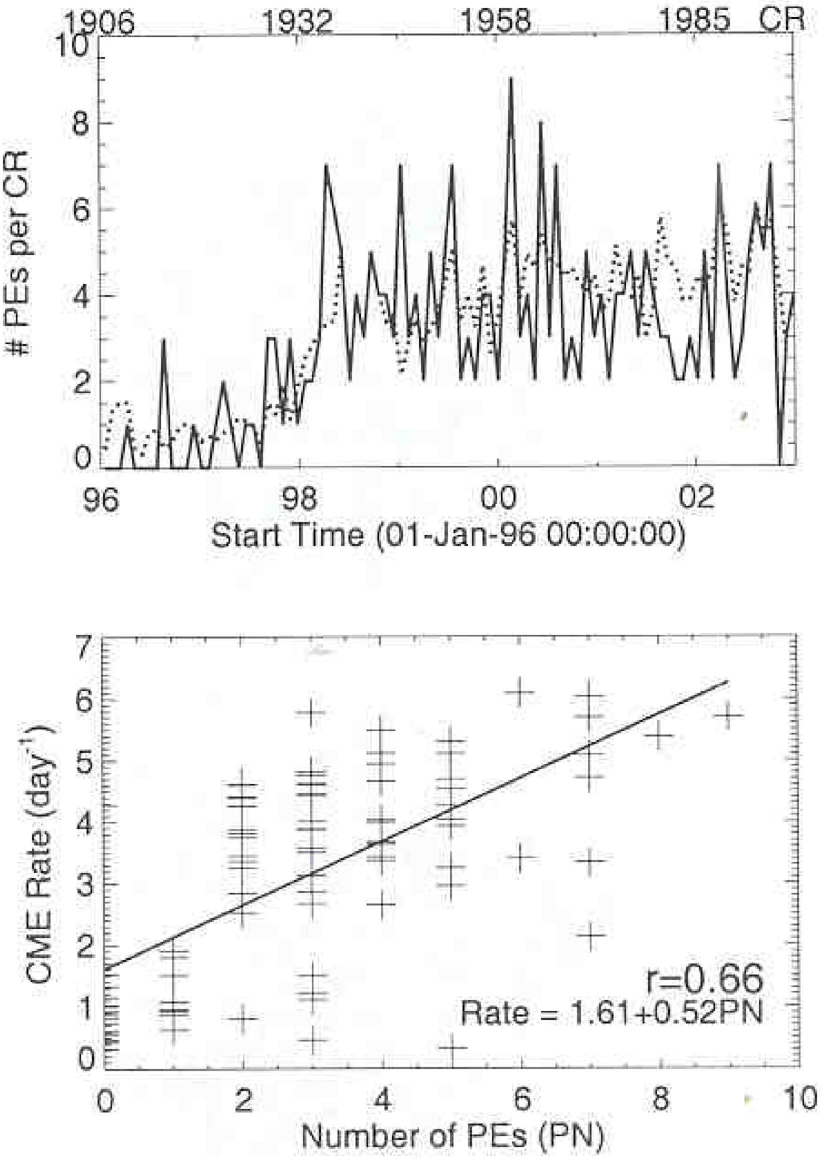

Figure 3.7: Top panel: Comparison between the solar cycle variation of prominence eruptions per CR (solid line) and the daily CME rate (dotted line). Bottom panel: Correlations of the CME rate and the prominence number (PN). The solid line is the derived regression line. PEs labels the prominence eruptions and PN labels the prominence number (Gopalswamy et al. 2003).

It had been recognized early on that erupting prominences/disappearing filaments are the most common form of the solar activity found to be associated with CMEs (Webb, Krieger & Rust 1976; Munro et al. 1979; Webb & Hundhausen 1987; St Cyr & Webb 1991). Based on the white-light observations of CMEs taken by *Skylab* (Munro et al. 1979) it was found that about 70% of all observed CMEs were associated with erupting prominences/disappearing filaments with or without the presence of a solar flare. Based on SoHO/EIT & LASCO data, Subramanian and Dere (2001) reported that many active region CMEs were not associated with disappearing filament/erupting prominence. From a study of microwave observations, Gopalswamy et al. (2003) found that $\sim$ 72% of the prominence eruptions were clearly associated with CMEs. Further they found that the CME onsets and related prominence eruptions started roughly at the same time. Fig. 3.7 from Gopalswamy et al. (2003) shows the correlation between the number of prominence eruptions and CMEs in each Carrington Rotation (CR) for the time period 1996-2002. The correlation coefficient was found to be 0.66 which is weaker than the correlation between CMEs and sunspots (see Fig 3.6, bottom panel). They also compared the latitude variations of CMEs with latitude variations of prominence eruptions and concluded that CMEs originating at higher latitude are commonly associated with prominence eruptions. The finding supports the results that active region CMEs may be of different nature.

3.3.3 Flares and CME Onset

Solar flares are the powerful and explosive events on the Sun, releasing energies up to $\sim 10^{32}$ erg over time periods of less than an hour. They generally cover only 0.1% of the visible hemisphere at any one time (Harrison 1995). They were first documented in 1859 by Carrington and Hodge during the regular observations of sunspots (Carrington 1859). Flares have a wide range of sizes and energies, and various classification schemes have been developed over the years. A recent classification scheme (see Table 3.2) to describe the X-ray intensities of flares has been introduced after the GOES (*Geostationary Operational Environmental Satellite*) satellites were flown which have systematically recorded the total intensity in soft X-rays covering the wavelength range of 1 - 8 Å.

The association of flares with CMEs has been a subject of intensive research in solar physics and space sciences for a long time. Since CMEs and flares have often been found to be associated with each other, the potential cause-effect relationships between them have attracted much attention in the community (Gosling 1993; Hundhausen 1999). However the cause-effect relationship is still a controversial subject because of the lack of high resolution observation of CMEs in their early phase of evolution, particularly in the low corona. So far, coronagraphs provide high cadence observation of CMEs only above $\sim 2\ R_\odot$, except LASCO/C1 which, for the first time, provided informations from 1.1 to 3.0 $R_\odot$. Therefore, most of the time the onset time of CMEs has been derived from backward extrapolation of the height-time evolution profile of the corresponding CME which in itself can invoke an error of several minutes in the estimation of the onset time. The left panel of Fig. 3.8 shows the height-time diagram of the CME observed on 11-Jun-1998 taken from the CME catalogue[2].

By making use of the internally occulted *LASCO/C1* coronagraph on board *SoHO*, Zhang et al. (2001) analyzed four well observed CME events detected by C1. The advantage of these observations was that there was no need of extrapolation in order to obtain the onset time of the CME (see Fig. 3.8 right panel; Zhang et al. 2001). The figure illustrates the temporal relationship between the CME and flare on 11-Jun-1998. In the plot, the thick line represents the X-ray flux profile

---

[2] http://cdaw.gsfc.nasa.gov/CME_list/

Table 3.2: The soft X-ray classification of solar flares (Harra 2004).

GOES class	**Intensity (ergs $cm^{-2}\ s^{-1}$)**
B	10^{-4}
C	10^{-3}
M	10^{-2}
X	10^{-1}

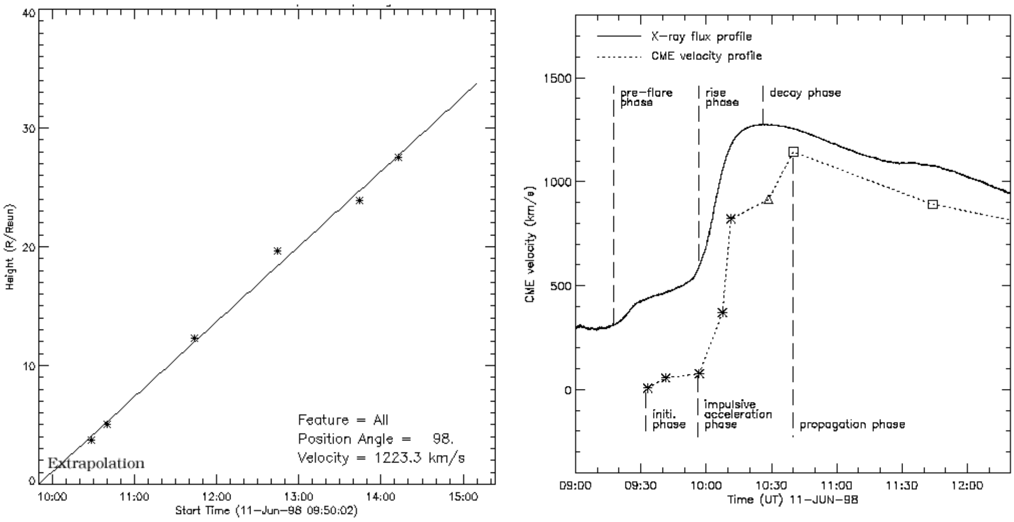

Figure 3.8: Left panel: Height-time diagram of the CME observed on 11-Jun-1998 taken from the CME catalogue. Right panel: CME speed-time profile (dotted line) and soft X-ray flux temporal profile (solid line) for the event on 11-Jun-1998. The CME impulsive acceleration phase coincides with the flare intensity rise phase (Zhang et al. 2001).

in normalized units. The dotted line corresponds to the CME speed profile. The initiation phase of the CME is identified to lie in the pre-flare phase of the CME whereas the rising phase of the flare corresponds to the impulsive acceleration phase. When the flare intensity starts decreasing, the CME propagates outward almost with constant speed as illustrated in Figure 3.8. According to Zhang et al. (2001) the initiation phase of the CME occurs before the onset of the associated flare. However, there are may CMEs which are not associated with flares and vice-versa (e.g., Kahler 1992).

3.3.4 CMEs and X-ray Sigmoids

Sigmoids are S-shaped structures frequently seen on the solar disk, usually associated with active regions (Canfield et al. 1999). The sigmoid structures are likely the result of twisted magnetic fields. Shearing and stressing of magnetic field lines above the magnetic neutral line may have led to the helical structure which are S-shaped in projection. They are often observed in soft X-ray and EUV images (Canfield et al. 1999, Sterling et al. 2000). The shape of the twisted loops was found to have a hemispheric preference: Forward (reverse) S-shape structure dominant in the southern (northern) hemisphere independent of solar cycle (Rust & Kumar

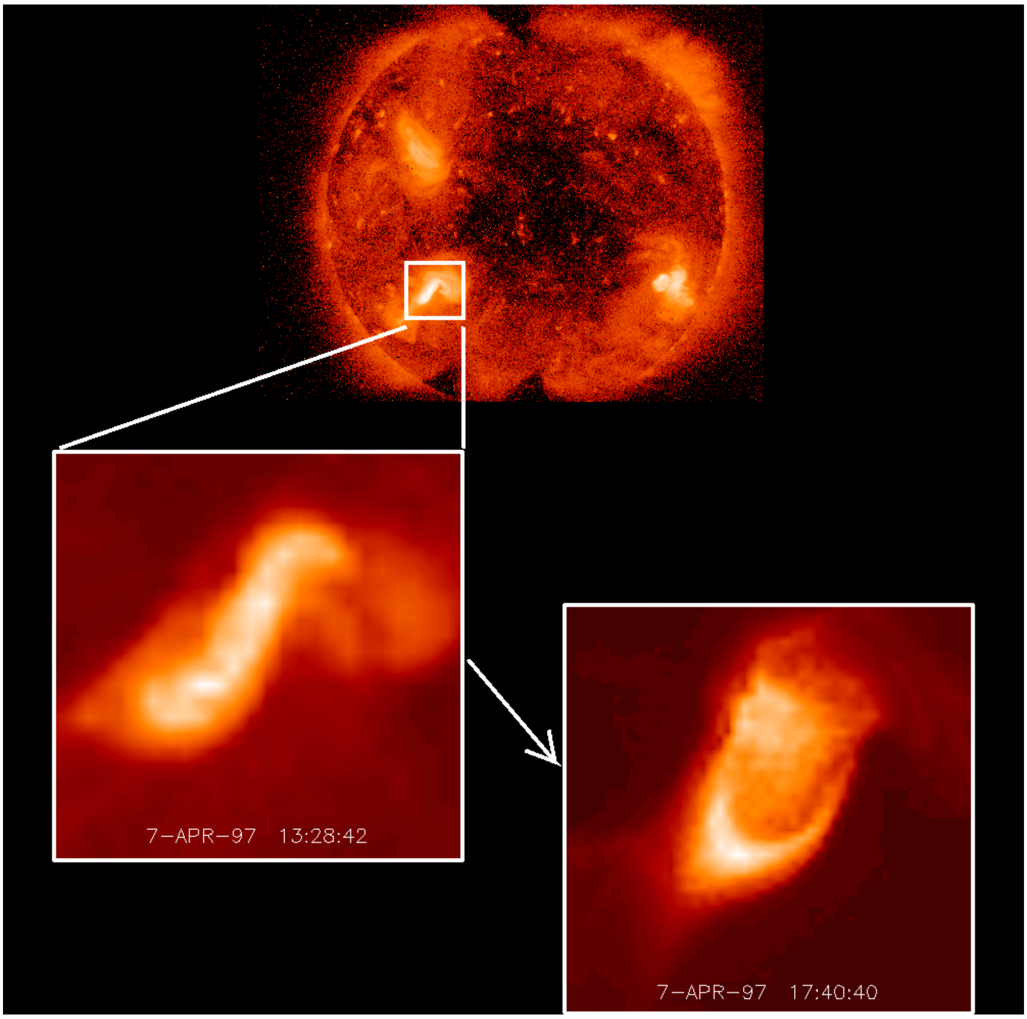

Figure 3.9: Collage showing the sequence from pre-eruption sigmoid to post-eruption cusp/arcade imaged by Yohkoh/SXT on 07-Apr-1997. Courtesy: Yohkoh/SXT team.

1996). The sigmoidal shape has been described as an observational signature of azimuthal currents in twisted coronal structures, i.e., loops, arcades, or filaments (e.g., Aschwanden 2004). When the helical twist exceed a critical value, the structure might become unstable, producing a disruption of the magnetic field leading to the expulsion of a filament or CME (Gibson and Low 2000). Canfield et al. (1999) established statistically that active regions seem to be significantly more likely to erupt if they have a sigmoidal shape. An S-shaped active region structure may flare and transform itself into a set of bright loops during the launch of a CME (Hudson et al. 1998). The active region itself evolves from a sheared sigmoid seen in X-rays to a potemtial-like post-eruption arcade (Kahler 1977, Sterling et al. 2000).

3.3.5 CMEs and Post-Eruptive Arcades (PEAs)

Post-eruptive arcades (PEAs) are large-scale transient loop systems that often form in the corona during solar eruptions. PEAs, often also called post-flare loops (PFLs) are best visible at EUV wavelengths (Sterling et al. 2000). An example of a PEA is

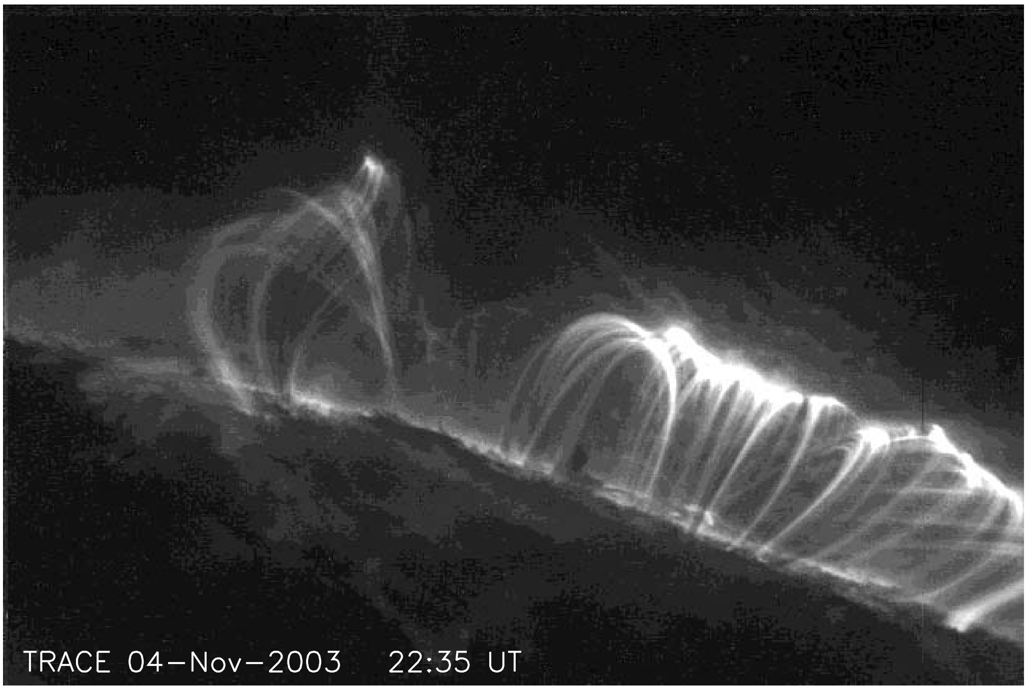

Figure 3.10: A post-eruptive arcade imaged by TRACE at 195 Å on 04-Nov-2003 at 22:35 UT (source: Tripathi et al. (2004) .

shown in Fig. 3.10 taken by TRACE (Transition Region And Coronal Explorer) on 04-Nov-2003 at 195 Å. In Hα wavelengths footpoints of these loops are often seen as ribbons and are referred to as the so called two-ribbon flares.

The development of large-scale X-ray arcade-like loop system after the brightening of S- and reversed S-shaped hot (T$\sim$2$\times$10^6 K) loop structures often observed in association with coronal mass ejections (e.g., Rust and Webb 1977; Svestka et al. 1998; Hudson et al. 1998) can also be seen at EUV wavelengths (Sterling et al. 2000).

3.3.6 Extreme Ultraviolet Imaging Telescope (EIT) Waves and CMEs

”EIT waves” (Thompson et al. 1998) named after the Extreme Ultraviolet Imaging Telescope on the SoHO mission, are large-scale wave disturbances detected in the Sun’s lower corona. An example of an EIT wave is shown in Fig. 3.11. EIT waves appear as propagating large-scale bright-fronts. They often propagate nearly isotropically over large parts of the visible solar disk, being blocked at boundaries of coronal holes also avoiding the active regions (Thompson et al. 1998, 1999). Thompson et al. measured the propagation speed of the these waves. The typical speed was found to be about 250 km/s.

Soon after the discovery of EIT waves it was suggested that these waves are strongly associated with CMEs (Plunkett et al. 1998). Based on the observations made by EIT at 195 Å, Biesecker et al. (2002) confirmed that EIT waves are often found to be associated with CMEs. Additionally, in brightness a dimming is

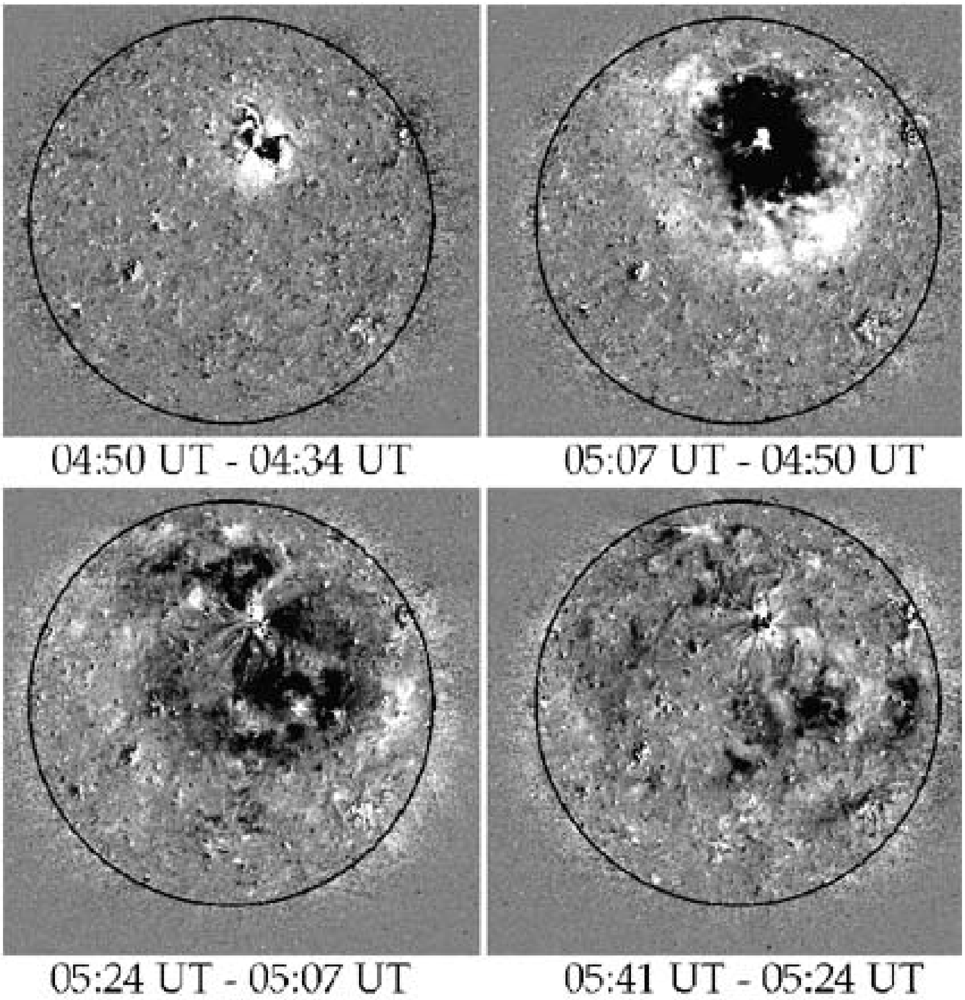

Figure 3.11: SoHO/EIT 195 Å running difference images showing a large-scale wavefront which was observed in association with the CME on 12-May-1997 (Thompson et al. 1998).

usually seen behind the front of the EIT waves (Thompson et al. 2000a; Zhukov & Auchère 2004). Thompson et al. found that the dimming areas may extend to large distances on the solar disk (see Fig.3.11). The dimmings seem to correspond to the CME locations obtained by tracing back the CMEs spatial extent detected by LASCO/C2. Thompson et al. concluded that the dimmings are due to evacuation of mass during the CME. Later Harra & Sterling (2001) found blue-shifts in the oxygen five line in a dimming region corresponding to outflow velocities up to 80 km/s based on the data from the Coronal Diagnostic Spectrometer (CDS), supporting evidence for the outward ejection of coronal matter.

3.4 Theoretical Concepts of CMEs

The fundamental theoretical question about CME initiation has been studied for many years. A number of interesting theoretical models have been proposed to explain the nature and origin of CMEs. Here we briefly summarize the basic concept of CMEs based on a review by Kilmchuk (2001).

In most of CME models, the pre-eruption magnetic field has either a simple arcade-like (see Fig. 3.12, left panel) or a flux-rope like (see Fig. 3.12, right panel) configurations. Arcade field lines arch directly over the magnetic polarity inversion line connecting opposite magnetic polarities on the photosphere. The arcade like configuration may get sheared due to displacement of positive and negative polarities in opposite directions parallel to the polarity inversion line due to the Sun's differential rotation. Due to this shearing the magnetic fields can gain magnetic free energy that can be released during an eruption. Left image of Fig. 3.12 shows an arcade-like configuration which corresponds to a dipolar configuration. There may also exist quadrupolar configurations consisting of multiple arcades lined up side by side.

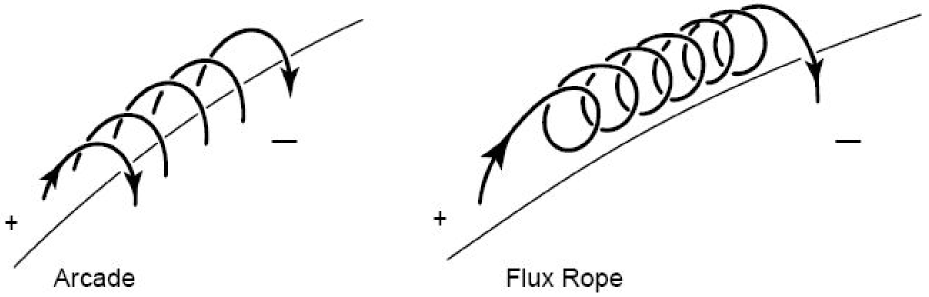

Figure 3.12: Schematic representation of arcade-like and flux-rope like coronal magnetic field geometry (Klimchuk 2001).

The flux-rope magnetic topology is quite different from the arcade-like magnetic topology. Here magnetic field lines form a helical structure which lies above the neutral line. Flux-ropes are disconnected from the photosphere except at the ends, i.e. at their foot-points (Klimchuk 2001). The right panel of Fig. 3.12 shows a flux-rope like topology. The cartoon representing the flux-rope topology has much more twist than expected in the real structure. Sometimes a flux-rope may have one turn or less (Klimchuk 2001) which makes the distinction between flux-rope and arcade-like topology doubtful (Titov and Démoulin 1999). In a typical three-part CME, it is suggested that the dark cavity corresponds to a flux-rope seen edge-on (e.g., Chen et al. 1997, Dere et al. 1999). An example of a flux-rope CME is given in Fig. 3.13. It is commonly believed that the embedded core represents prominence material which is trapped at the bottoms of helical field lines and dragged upward during the eruption (Klimchuk 2001). However all CMEs are not comprised of three-parts (e.g., Burkepile and St. Cyr 1993, Dere et al. 1999). It should be noted that observations of flux-rope like topology in the corona does not imply that a flux-rope was part of the initial configuration. Gosling (1993) has suggested that a flux-rope may form due to magnetic reconnection during the eruption of a sheared arcade.

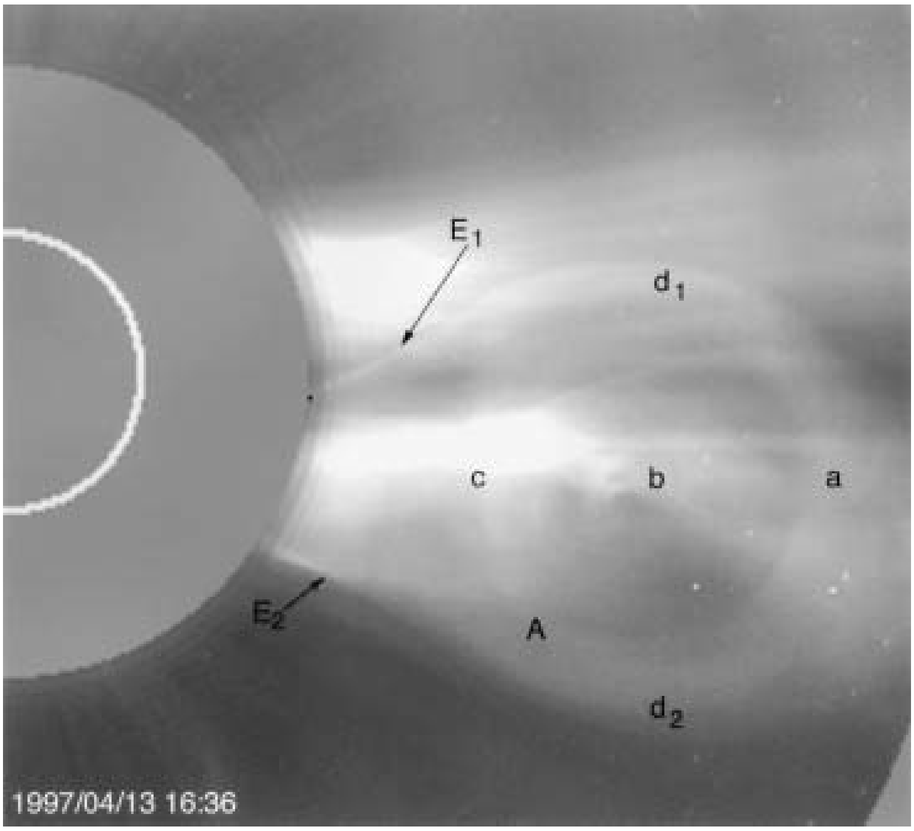

Figure 3.13: Image of a CME taken by LASCO/C2 at 16:36 UT on 13-Apr-1997. Note the nearly circular rim A. Leading edge a, trailing edge c, upper d_1, and lower d_2 edges are labeled. Bright edges E_1 and E_2 are visible. Concentric striated fine features can be seen in A (Chen et al. 1997).

Though it is not certain, in many models it has been presumed that a CME occurs when the balance of forces that maintain the equilibrium is lost. Somehow the resultant force pointing upward becomes greater than the resultant force pointing downward (Klimchuk 2001). There are mainly three forces in order to balance the equilibrium: The gravity force, the plasma/gas pressure, magnetic forces (magnetic pressure and magnetic tension). In many of the CME models the gravity force and gas pressure play important roles. However in many models the gravity force and the plasma pressure are ignored due to the low value of plasma beta (ratio of plasma pressure with magnetic pressure), especially within active regions.

On the Sun, the magnetic field spreads through the entire corona. Regions of strong magnetic fields in the corona have enhanced pressure and therefore magnetic field tends to expand into regions of weak field. On the solar surface, the arcade-like magnetic field lines arch over a flux-rope that may exist. The foot-point of these arcades are in the photosphere and the tension in the field lines act to hold the flux-rope in space. Similar kind of mechanism exist where the magnetic pressure is balanced by magnetic tension force in simple arcade-like magnetic field topology where there is no flux-rope (Klimchuk 2001). The magnetic field strength is maximum at the center of the arcade in the equilibrium. The outward force produced by the gradient in magnetic pressure is balanced by the inward magnetic tension force.

Whenever the balance in these two forces is lost the eruption begins. If this force imbalance grows with time the eruption becomes violent.

A variety of theoretical models have been proposed in order to understand the CME eruption. For reviews see Low (1999, 2001), Forbes (2000), and Klimchuk (2001). Klimchuk (2001) classified existing CME models into five distinct classes. Based on the classification of Klimchuk (2001) we briefly describe the CME models.

3.4.1 Thermal Blast Wave

Initially flares were thought to be the main trigger of CMEs. It is assumed that the magnetic field can not sustain the greatly enhanced thermal pressure produced by a flare and thus pushes the CME outward into the heliosphere (e.g., Dryer 1982; Wu 1982). An analouge to the thermal blast model is the overpressure generated by a bomb explosion (Fig. 3.14, first panel). However, many CMEs have been detected without a preceding flare. Further it was found that often the CME was launched prior to a flare (Harrison 1986). Although sometimes the relative onset timing of flares and CMEs are very close, it is believed that the thermal blast model can not explain the onsets of CMEs (e.g., Dryer 1996; Délannée et al. 2000; Zhang et al. 2001).

3.4.2 Dynamo Model

The dynamo driven CME model is analogous to the stressing of a spring by an external force (see Fig. 3.14, second panel). The rapid displacement of the footpoints of a coronal magnetic field system may generate stressing in the magnetic field which in turn leads to the inflation of the entire magnetic system (Klimchuk 2001). In this model a sufficiently fast driver is expected to produce a CME-like eruption requiring a very fast motion of the foot points, at least two orders of magnitude more than the observed values (e.g., Krall et al. 2000).

3.4.3 Mass Loading Model

This model is known as the *storage and release* model. The storage and release model involves the slow build-up of magnetic stresses prior to the eruption. In the pre-eruption phase the mass loading process might be manifested through the spatial growth of a quiescent or active prominence (see Fig. 3.14 third panel). There seem to exist two types of mass loading: 1) Through extremely dense compact prominences at chromospheric temperatures, 2) through dense plasma distributed over large volume which become unstable if they overlay coronal volumes of lower densities. This model proposes that the prominences play the fundamental role in CME initiation (Low 1996, 1999), however they do not explain many CMEs not associated with prominences.

3.4.4 Tether Cutting Model

Magnetically dominated configurations like coronal loops generally require a balance between the magnetic pressure force directed upward and the magnetic tension force directed downward. These tensions are provided by the magnetic field lines and called *tethers*. Once some tethers are released (see Fig. 3.14 fourth panel), the strain in other tethers increases. Eventually the strain becomes so large that the remaining tethers (field lines) start to break up. A 2D-model (Forbes & Isenberg 1991; Isenberg et al. 1993) has been developed which demonstrates how a tether release may work in the corona. The presence of resistivity in the non-ideal MHD situation leads to magnetic reconnection processes. Due to reconnection the tethers break-off and an eruption occurs (e.g., Forbes 1991; Lin & Forbes 2000; Mikíc & Linker 1999).

3.4.5 Tether Straining Model

The tether strain model is similar to the tether release model. In this model the strain on the tethers gradually increases by some external forces until they break (see Fig. 3.14, fifth panel). Antiochos (1998) and Antiochos et al. (1999) proposed a model based on the quadrupolar structure of two adjacent arcades. In this model, one loop arcade is continuously sheared and builds up magnetic stress until magnetic reconnection starts. The magnetic reconnection process then opens up the magnetic field in the upward direction and allows the CME to escape into interplanetary space. Other examples of tether straining models are the sheared arcade model suggested by Mikíc & Linker (1994), Amari et al. (1996) and the flux rope model suggested by Wu et al. (1995) and Wu et al. (2000).

3.5 Summary

Many models have been developed to explain the onset and propagation of CMEs, but very few have been able to explain the exact nature of the mechanism which triggers them. For example, several models propose that CMEs are triggered by the onset of a micro-instability but they do not actually prescribe the physical process producing it (Forbes 2000). At the present time, there is a general (but not universal) consensus that the onset mechanism involves the release of free magnetic energy associated with electric currents flowing in the corona. However, there is no consensus about the mechanism which releases the energy.

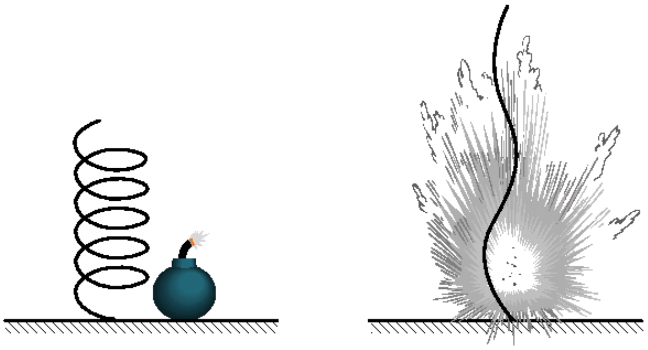

Thermal Blast

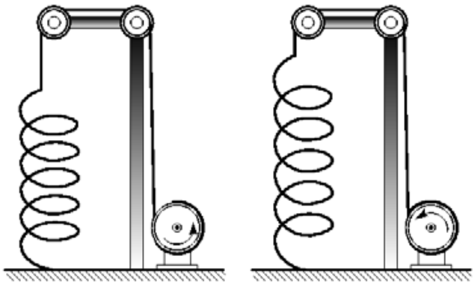

Dynamo

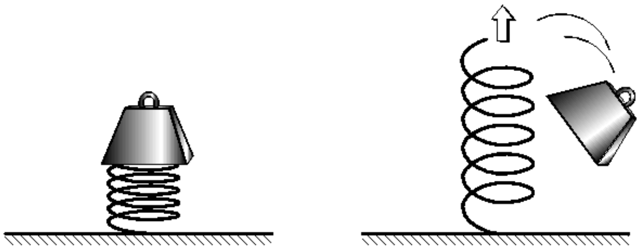

Mass Loading

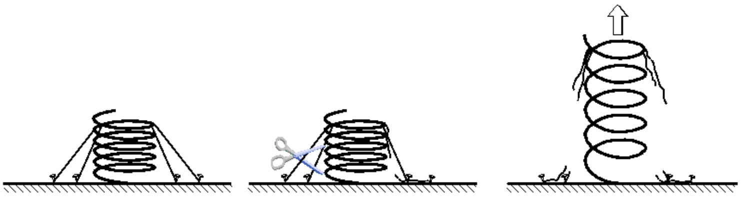

Tether Release

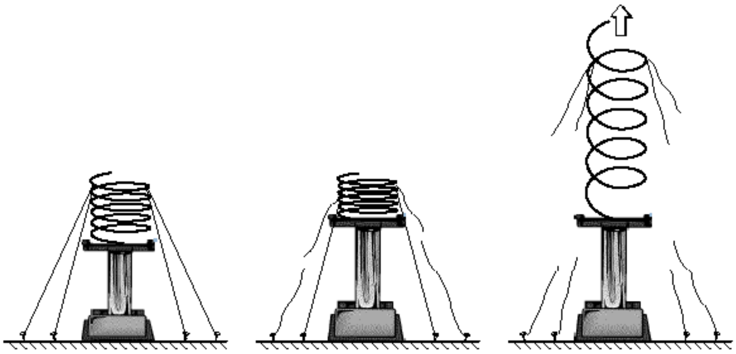

Tether Straining

Figure 3.14: Physical analogies of five different coronal mass ejections model. From top to bottom: 1) thermal blast model, 2) dynamo model, 3) mass loading model, 4) tether cutting model, 5) tether straining model (Klimchuk 2001; adopted from Aschwanden 2004).

4 Instruments

Sophisticated instrumentation has been an integral part of modern solar research. From the humble beginnings of observations of sunspots using a telescope and a sheet of paper, modern solar research aims to get ever closer to the Sun in upcoming missions like Solar-B, Solar Orbiter and Solar Probe. And missions like STEREO will provide us with the first three-dimensional view of the heliosphere. These missions are undertaken as a consequence of the overwhelming success of the Solar and Heliospheric Observatory (SoHO) mission launched in late 1995. In this chapter we provide a brief overview of the instruments that have provided the data used for our research which includes the Extreme Ultraviolet Imaging Telescope (EIT), the Large Angle Spectrometric Coronagraph (LASCO) and the Michelson Doppler Imager (MDI). Inputs from ground-based observations complement the space-based observations, helping to resolve ambiguities and thus extents the dataset of reliable information.

4.1 Introduction

Observations of the solar corona are only possible either during a total solar eclipse or by means of a coronagraph. Studies of the solar corona were extremely limited until the launch of a series of Orbiting Solar Observatory (OSO) missions that observed the Sun in the Ultraviolet (UV), X-ray and white-light spectral range. Within a few months after launch, the first coronal transient was identified through the coronagraph flown aboard OSO-7 (Tousey 1973). These coronal transients were later termed *coronal mass ejection* .

In 1973, Skylab was launched (Tousey 1977). It provided images at X-ray, Extreme Ultra-violet (EUV) and white-light and spectra of the solar chromosphere and corona. The Solar Maximum Mission (SMM) was flown in 1980 to study solar flares (e.g. MacQueen et al. 1980). SMM was comprised of high energy X-ray detectors, a UV spectrograph and a white-light coronagraph. This satellite provided simultaneous observations of solar flares in X-ray and UV spectral ranges. These observations greatly enhanced our understanding of transient features like flares and CMEs.

The successful launch of the Solar and Heliospheric Observatory (SoHO) on 02-Dec-1995 provided new challenging opportunities. The combined analysis of the data taken by different instruments aboard SoHO and ground-based instruments, currently allow us to study CMEs and their corresponding solar source regions in the

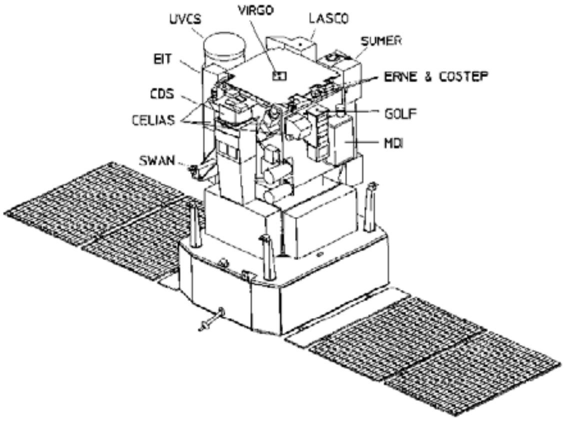

Figure 4.1: Schematic of SoHO spacecraft showing all the scientific instruments aboard (Domingo et al. 1995).

low corona and photosphere based on data obtained by the EIT (Extreme Ultraviolet Imaging Telescope), the LASCO (Large Angle Spectrometric coronagraph) and the MDI (Michelson Doppler Imager) instruments aboard SoHO along with ground-based Hα observations and observations made by Soft X-ray Telescope (SXT) aboard Yohkoh.

4.2 The Solar and Heliospheric Observatory (SoHO)

The Solar and Heliospheric Observatory is a project of international cooperation between the European Space Agency (ESA) and the National Aeronautics & Space Administration (NASA). SoHO has 12 different instruments on board. Fig. 4.1 displays the schematic of the SoHO spacecraft and the different instruments aboard.

The principal scientific objectives of the SoHO mission are (Domingo et al. 1995):

- to study the solar interior, using the techniques of helioseismology,
- to study the heating mechanisms in the solar corona,
- to investigate the origin of the solar wind and its acceleration processes.

Depending on the area of research, the instruments can be classified in three groups: helioseismology instruments, instruments for coronal studies, and solar wind ”in-situ” instruments. A brief summary of the instruments is provided in Table 4.1.

SoHO was launched on 02-Dec-1995 near solar minimum. Initially it was injected into a low Earth parking orbit and finally into a halo orbit (see Fig. 4.2) around the L1 Lagrangian point, about 1.5×10^6 km sunward from the Earth. The L1 halo orbit has several particular advantages as compared to a low Earth orbit: 1) it provides smooth Sun-spacecraft relative velocity changes throughout the orbit, 2) it is permanently outside of the magnetosphere, and c) it allows uninterrupted observations of the Sun.

Table 4.1: The SoHO Scientific Instruments (Domingo et al. (1995)

Instruments	**Measures**	**Technique**	**Kb/sec**
HELIOSEISMOLOGY			
GOLF	Global Sun velocity oscillations (l= 0, 3)	Na-vapour resonant scattering Doppler shift and circular polarization	0.16
VIRGO	Low degree (l= 0, 7)irradiance oscillations and solar constant	Global Sun and low resolution (12 pixels) Imaging, active cavity radiometer	0.1
MDI/SOI	Velocity oscillations, and harmonic degree up to 4500	Fourier tachometer, angular resolution: 1.3 and $4''$	5 (+160)
SOLAR ATMOSPHERE REMOTE SENSING			
SUMER	Plasma flow characteristics (T, density, velocity) chromosphere through corona	Normal incidence spectrometer, 50-160nm, spectral res. 20000-40000, angular res. ≈$1.3''$	10.5 (or 21)
CDS	Temperature and density: transition region and corona	Normal and grazing incidence spectrometers, 15-80 nm, spectra. res. 100-10000,angular res.≈$3''$	12 (or 22.5)
EIT	Evolution of chromospheric and coronal structures	Full disk image ($42' \times 42'$ with 1024 × 1024 pixels) in He II, Fe IX, Fe XII and Fe XV	1 (or 26.2)
UVCS	Electron and ion temperature, densities, velocities in corona 1.03 to 10 R$_\odot$	Profiles and/or intensity of selected EUV lines between 1.03 et 10 R$_\odot$	5
LASCO	Evolution, mass, momentum and energy transport in corona (1.1-30 R$_\odot$)	1 internally and 2 externally occulted coronagraphs; Fabry-Perot spectrometer for 1.1-3 R$_\odot$	4.2 (or 26.2)
SWAN	Solar wind mass flux anisotropies and its temporal variations	Scanning telescopes with hydrogen absorption cell for Ly-α-light	0.2
SOLAR WIND 'IN SITU'			
CELIAS	Energy distribution and composition (mass, charge, charge-state)(0.1-1000 KeV/e)	Electrostatic deflection, time of flight measurements, solid state detectors	1.5
COSTEP	Energy distribution of of ions (p,He) de 0.04-53 MeV/n and electrons 0.04-5 MeV	Solid state and plastic, scintillator detectors	0.3
ERNE	Energy distribution and isotopic composition of ions (p-Ni) 1.4-540 MeV/n and electrons 5-60 MeV	Solid state and plastic scintillator detectors	0.7

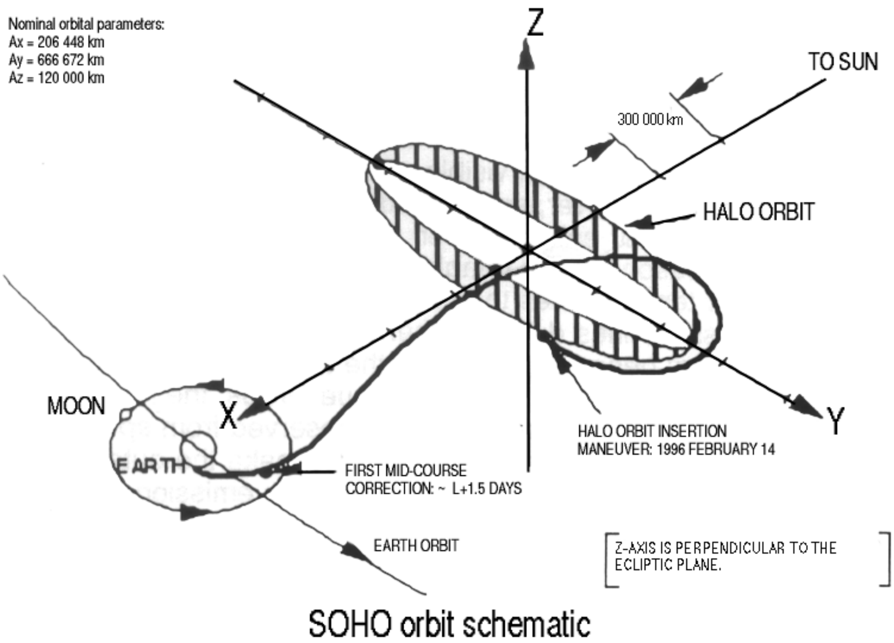
Nominal orbital parameters:
Ax = 206 448 km
Ay = 666 672 km
Az = 120 000 km
Z
TO SUN
300 000 km
HALO ORBIT
MOON
X
Y
EARTH
HALO ORBIT INSERTION
MANEUVER: 1996 FEBRUARY 14
FIRST MID-COURSE
CORRECTION: ~ L+1.5 DAYS
EARTH ORBIT
Z-AXIS IS PERPENDICULAR TO THE
ECLIPTIC PLANE.
SOHO orbit schematic

Figure 4.2: Orbit of SoHO (Domingo et al. 1995).

4.2.1 The Extreme Ultraviolet Imaging Telescope (EIT)

Scientific Goals of EIT

The principal scientific goals of EIT are to study the dynamics and evolution of coronal structures over a wide range of time-scales, sizes and temperatures in order to bring new insights into the mechanisms responsible for transient events such as CMEs, flares, coronal heating processes and those responsible for solar wind acceleration. Images taken by EIT at different EUV-wavelengths provide informations about different solar activity features. Fig. 4.3 displays images taken on 02-Mar-2002 at all the four different wavelengths. The general informations provided by the images can be summarized as follows (Moses et al. 1997):

1. The images taken at 171 Å (FeIX, X; Fig. 4.3 top left panel) shows that diffuse and unresolved emission is present over most of the quiet Sun, including coronal hole regions. In this passband the open magnetic field regions as well as closed field structures can be distinguished. Active region structures can be identified by its different brightness. At 171 Å EIT provides one image every six hours.

2. The 195 Å (FeXII; Fig. 4.3 top right panel) images are dominated by the closed field regions of the quiet Sun. Coronal holes are more easily visible in this channel because of the contrast between the emission intensity of the open field regions and the closed field quiet Sun regions. In the same way, the X-ray bright points are more easily identified. Because of the high contrast and high sensitivity compared to the quiet Sun structure of the Fe XII channel, it is frequently used in order to study the evolution of coronal structures. On average EIT provides one image every 12 minutes at this particular wavelength.

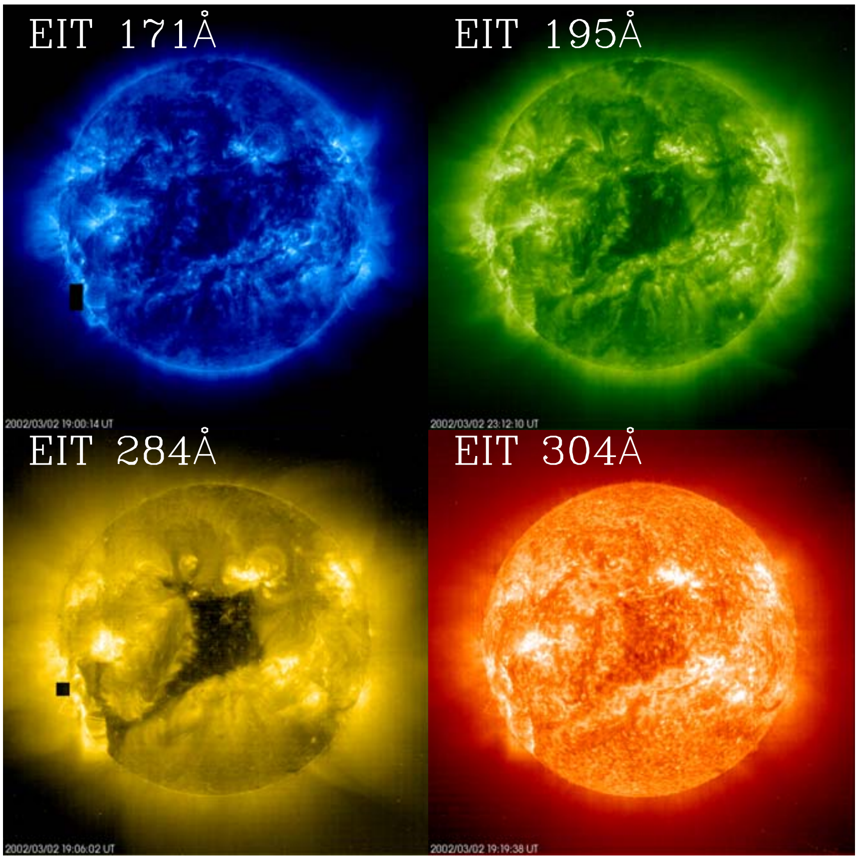

Figure 4.3: Images taken by the Extreme ultraviolet Imaging Telescope at four different wavelengths on 02-Mar-2002. Courtesy: SoHO/EIT consortium.

3. The 284 Å (Fe XV; Fig. 4.3 bottom left panel) images are dominated by the emissions from active region loops. Outside the active regions, the emission at this wavelength is primarily due to X-ray bright points, regions associated with erupting filaments and large-scale loop structures. In quiet Sun regions, there is a low level brightness structure related to the inter-network field structure. Coronal holes are best visible in this channel because of difference in contrast between the closed field and open field regions. The cadence of EIT at this wavelength is six hours.

4. The 304 Å (HeII; Fig. 4.3 bottom right panel) images are dominated by the network structure of the transition region. Bright network elements are visible throughout regions with closed loop structure. The active regions are generally bright in He II images. Prominences are very well seen in this channel. Filaments are slightly more difficult to identify because the contrast of the absorption features is frequently comparable to the contrast of the network structure. The time resolution of EIT is about 6 hours at this wavelength.

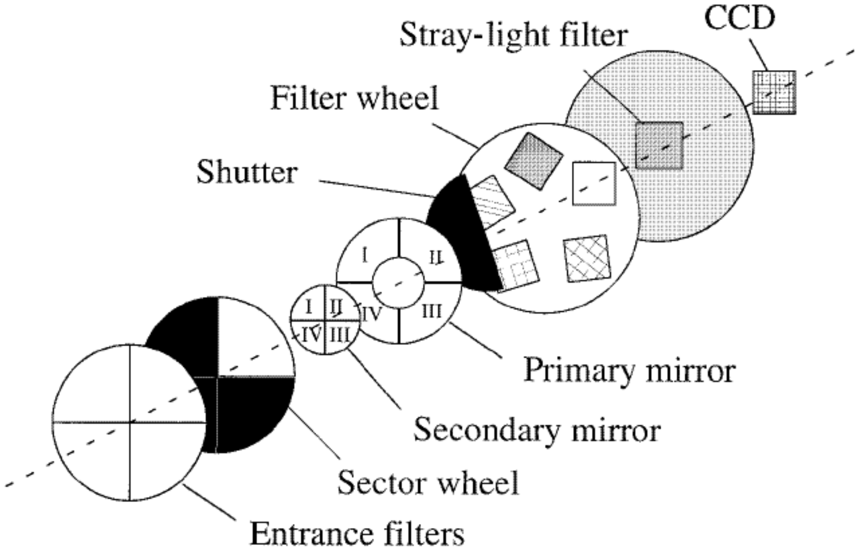

Figure 4.4: Optical elements of the Extreme ultraviolet Imaging Telescope (Dere et al. 2000).

Technical Description

The EIT instrument (Delaboudinière et al. 1995 and references therein) provides full disk observations of the transition region and solar corona with a field-of-view (FOV) of 1.5 $R_\odot$ on an EUV sensitive charged coupled device (CCD) camera. Briefly, EIT consists of a Ritchey-Chretien telescope with a CCD and several optical filters. EIT records images of the complete Sun out to 1.5 $R_\odot$ (Dere et al. 2000) on a 1024× 1024 CCD detector with a resolution of 2.6 arcsec per pixel. The primary and secondary mirrors are multilayer coated in order to provide high reflectivity in narrow bands at EUV wavelengths. The mirror coatings have been applied in quadrants. For each quadrants different coating have been applied to select four wavelength bands near 171, 195, 284 and 304 Å. The sector wheel at the front of the telescope selects one of four quadrants at a time. A schematic diagram of the EIT optics is given in Fig. 4.4. Several other filters have also been included in the instrument design: entrance filter, filters on a filter wheel, and a final stray light filter immediately in front of the CCD. For details about the instrumentation see Delaboudinière et al. (1995) and Dere et al. (2000).

4.2.2 The Large Angle Spectrometric Coronagraph (LASCO)

Scientific Goals of LASCO

The primary scientific goals for LASCO are to understand (Brueckner et al. 1995):

1. the heating mechanism of the solar corona,
2. the location and mechanisms responsible for the acceleration of the solar wind,

Table 4.2: EIT Bandpasses. After Delaboudiénere et al. (1995)

Wavelength Å	**Ion**	**Peak Temperature**	**Observational Objective**
304	He II	8.0×10^4 K	chromospheric network; prominences
171	Fe IX,X	1.3×10^6 K	corona/transition region boundary; structures inside coronal holes
195	Fe XII	1.6×10^6 K	quiet corona outside coronal holes
284	Fe XV	2.0×10^6 K	active regions

3. the initiation mechanisms of coronal mass ejections,
4. the roles of coronal mass ejections with respect to evolution of the large-scale magnetic field, and
5. the distribution and properties of the dust clouds and effects of the small sun-grazing comets.

The images obtained from LASCO provide unique opportunities to study the transport of mass, momentum and energy through the solar corona into the solar wind. LASCO provides the following measurements:

1. The distribution of plasma parameters e.g. temperature, density, bulk & non-thermal velocities and direction of the magnetic field,
2. the sequences of coronal dynamic events, especially processes that occur in coronal mass ejections, and conditions that trigger them,
3. the spatial distribution and properties of the circumsolar dust particles including those newly released from sun-grazing comets.

Technical Description

The Large Angle Spectrometric Coronagraph (LASCO; Brueckner et al. 1995) is a wide-field, white-light coronagraph comprising of three optical systems: An internally occulted coronagraph C1 (1.1 to 3.0 $R_\odot$) and two externally occulted coronagraphs, C2 (2.0 to 6.0 $R_\odot$) and C3 (3.7 to 32.0 $R_\odot$). The field of view of the C3 telescope extends to 32.0 $R_\odot$, but at the equator and at the poles, the CCD detector limits the range to 30.0 $R_\odot$.

An externally occulted coronagraph has two basic limitations (Howard et al. 1997): First, for a given distance from the occulting disk to the first imaging element, the instrument can only provide images of the corona for a finite distance above the solar limb ($>1.5R_\odot$). At the inner edge of the FOV, most of the imaging elements are shadowed by the occulter. Consequently the spatial resolution in the inner corona is poor because of the very small effective aperture. Secondly, because of the size limitations, the aperture can not usually exceed a few centimeters. The LASCO

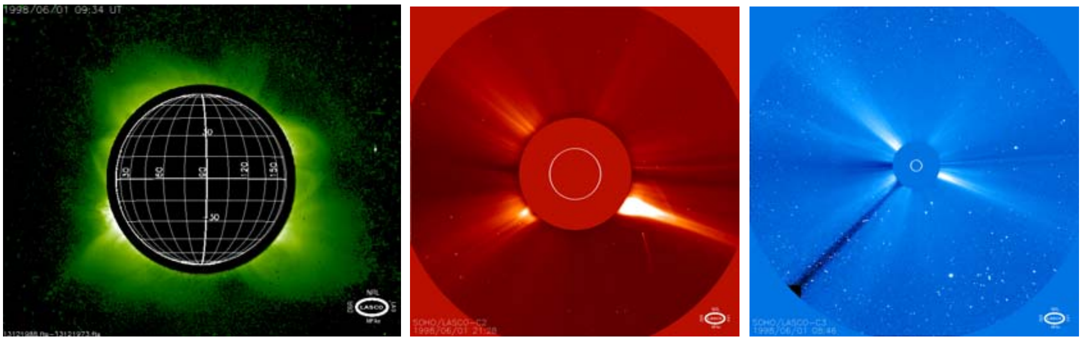

Figure 4.5: Coronal images taken by LASCO/C1 (left image), LASCO/C2 (middle image), LASCO/C3 (right image) showing the solar corona. The gridded circle in the left panel and the white circle in the middle and right panel represent the solar limb. Courtesy: SoHO/LASCO consortium.

coronagraph overcomes these problems by using three different coronagraphs with deliberately overlapping FOVs.

The C1 Coronagraph

The C1 coronagraph was the first internally occulted system operating in space. Because of the internal occultation, this coronagraph did not suffer from diffraction limited spatial resolution at its inner edge like the externally occulted coronagraphs. The C1 system used parabolic mirrors rather than lenses and observed the Sun with a pixel size of 5.6 arcsec. C1 observed the corona from 1.1-3.0$R_\odot$ (e.g., see Fig. 4.5 left image). A tunable Fabry-Pérot interferometer spectral filter system allows narrow pass band images of the solar corona to be obtained simultaneously over the entire FOV. For the complete instrumental details see Brueckner et al. (1995) and Schwenn et al. (1997). The C1 coronagraph was in operation from 1996 to 1998.

The C2 and C3 Coronagraph

The coronagraphs C2 and C3 are both externally occulted. The primary goal of C2 (2-6 $R_\odot$; e.g., see Fig. 4.5 middle image) and C3 (3.7-32 $R_\odot$; e.g., see Fig. 4.5 right panel) is to detect the corona as close as 2 $R_\odot$ from the Sun center up to 32 $R_\odot$ into the heliosphere. This approach in which an external occulting disk assembly completely shadows the objective lense from photospheric light, has the advantage of dramatically lowering levels of scattered stray light. The coronagraphs C2 and C3 observe the solar corona with a spatial resolution of 11.2 and 56 arcsec. The cadence of LASCO C2 is usually 20 minutes whereas C3 provides one image every 54 minutes.

4.2.3 Michelson Doppler Imager (MDI)

MDI Science Objectives

The main scientific objective of the Solar Oscillation Investigation (SOI, Scherrer et al. 1995) is to measure the internal stratification and dynamics of the Sun using the technique of helioseismology. The SOI investigation uses the Michelson Doppler Imager (MDI) instrument to observe intermediate to high degree p-modes oscillations. The Michelson Doppler Imager not only provides information about interior conditions but the images obtained offer the opportunity to understand the solar activity processes with respect to the solar cycle variations.

MDI provides high-resolution and full-disk observations of the line-of-sight (LOS) magnetic field. Measurements of the magnetic field are of fundamental importance to understand many physical processes in solar physics. The MDI instrument allows to derive longitudinal magnetograms by measuring the Doppler shift separately in right and left handed circularly polarized light.

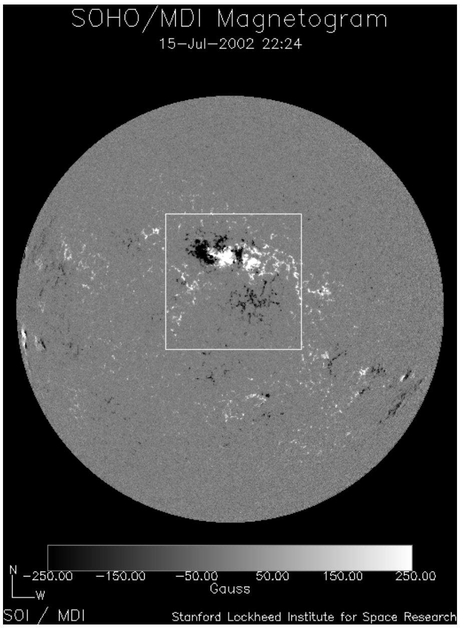

Figure 4.6: Longitudinal magnetogram taken by SoHO/MDI on 15-Jul-2002. The box in the image represents the region for which MDI provides high-resolution (up to 0.65 arcsec) observations. Courtesy: SoHO/MDI consortium.

Technical Description

The Michelson Doppler Imager (MDI) observes intermediate to very high degree p-mode solar oscillations. It samples the Ni I 6768 Å line with two wide-field tunable Michelson interferometers. MDI provides solar images of the line-of-sight velocity, line intensity, continuum intensity longitudinal magnetic field components and limb position. It can be operated in full disk mode (2 arcsec pixel size) to resolve modes in the range of harmonic degree $3 \leq l \leq 1500$ as well as in high resolution mode (0.65 arcsec pixel size) to resolve modes as high as $l=4500$. The high-resolution FOV is roughly 650 arcsec squared and is centered about 160" north of the equator on the central meridian. For complete details about the instrument see Scherrer et al. (1995).

For our study we use line-of-sight magnetograms obtained from SoHO/MDI. An example of a line-of-sight magnetogram is shown in Fig. 4.6. It shows a gray scale image of a magnetogram with the magnetic field density scaled in the range ± 250

G. The white box overlayed onto the image represents the region for which the MDI provides high-resolution observations.

4.3 Complementary Data

For the multi-wavelength study of the source regions of coronal mass ejections identified by EIT and LASCO, we additionally used ground-based Hα observations and coronal observations made by the soft X-ray telescope aboard Yohkoh. Hα observations were mainly used to compare our events with filaments whereas X-ray data were used to identify coronal brightness changes.

4.3.1 Ground-Based Hα Observations

BBSO Spectroheliograph

At Big Bear Solar Observatory (BBSO), a 20 cm telescope monitors the whole Sun. The Hα full disk images are obtained with a large format digital CCD and enhanced with modern image processing techniques. Every clear day the 20 cm full disk telescope observes the Sun from sunrise to sunset, obtaining an image every 30 seconds. The high quality (1 arcsec per pixel; e.g., see Fig. 4.7 left image) of the final full disk image is ideal for a detailed study of the evolution of fine solar structures as well as large-scale features.

Meudon Spectroheliograph

The Meudon Spectroheliograph routinely makes full-disk images of the Sun at the Hα line-center and at 0.5 Å on either side of the center. The Hα images have a spatial resolution of $\sim$ 2 arcsec per pixel (e.g., see. Fig. 4.7 right image). On an average one spectroheliogram image is taken per day.

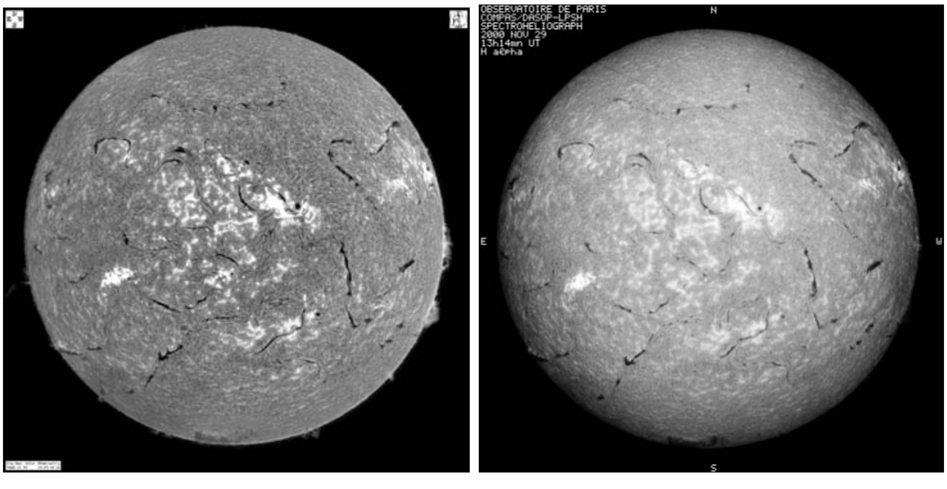

Figure 4.7: Left Image: High resolution Hα image taken at BBSO (http://http://bbso.njit.edu/) on 29-Nov-2000. Right image: Hα image taken by the Meudon observatory (http://bass2000.obspm.fr/home.php) on 29-Nov-2000.

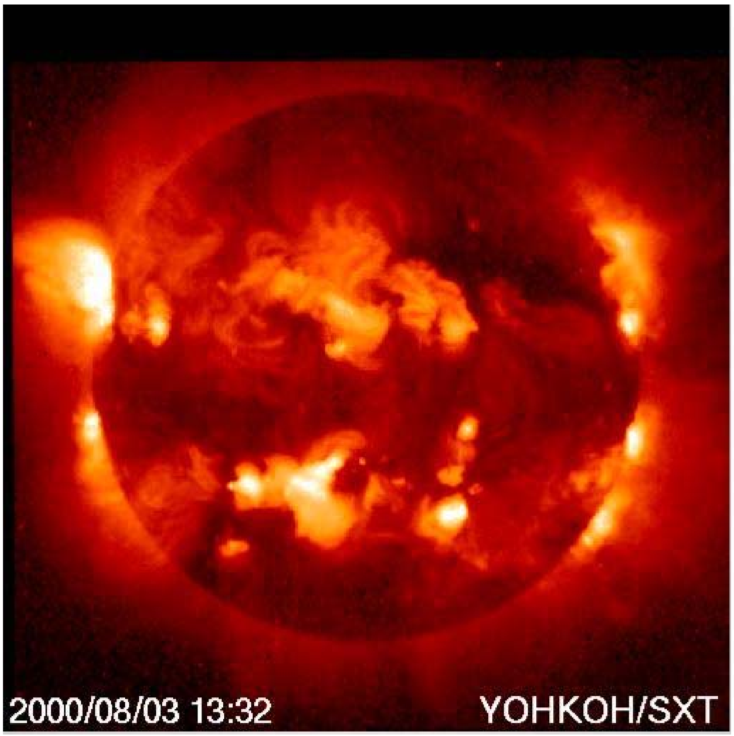

Figure 4.8: Image taken by the soft X-ray telescope aboard Yohkoh on 03-Aug-2000 at 13:32 UT.

4.3.2 *Yohkoh* Soft X-Ray Telescope (SXT)

The payload of the *Yohkoh* (Tsuneta et al. 1991) satellite was comprised of four different scientific instruments: The Hard X-ray Telescope (HXT), the Soft X-ray Telescope, the Wide Band Spectrometer (WBS) and the Bragg Crystal Spectrometer (BCS). The SXT observed the Sun in 3−60 Å (selectable with filters) in X-rays and between 4600−4800 Å and 4923−4323 Å. SXT provided a time resolution up to 0.5 sec and a spatial resolution of about 2.5 arcsec per pixel. It had a full solar disk field of view. For our study we used full-disk data, an image is shown in Fig. 4.8.

5 Observations and Data Analysis

Detecting subtle variations in data sets is a key problem to unravel interesting scientific phenomena. This chapter provides a detailed information about the applied methods for the data analysis used in this thesis.

5.1 Introduction

Erupting prominences/disappearing filaments represent to date the best solar activity phenomena found to be associated with CMEs (e.g., Webb, Krieger & Rust 1976; Munro et al. 1979; Webb & Hundhausen 1987; St Cyr & Webb 1991). However, based on the SoHO/LASCO and EIT observations, Subramanian & Dere (2001) showed that frequently no associated disappearing filaments had been observed mainly for CMEs originating from active regions (see Chapter 3, subsection 3.3.2). Contrary to the cooler disappearing filaments seen in absorption, brightening of S- or reversed S-shaped ($\sim 2 \times 10^6$ K) structures, called sigmoid, were proposed to indicate the onset of CMEs (e.g., Rust & Webb 1977; Svestka et al. 1998, Hudson et al. 1998). In many events large-scale transient coronal loop systems called *post-eruptive arcades* (PEAs), also known as *post-flare loops* (PFL), have been observed at EUV wavelengths (Sterling et al. 2000).

Such PEAs can be identified in the images taken by EIT at 195 Å. The successful and long years of operation of the SoHO mission provided unique opportunity for a detailed study of post-eruptive arcades in context with CMEs observed with LASCO. The basic methods that have been used to analyze the data set are described in this chapter.

5.2 Identification of Post-Eruptive Arcades

Post-eruptive arcades (PEAs) were identified using daily 195Å mpeg-movies[1] taken by EIT from 1997 to 2002. The EIT 195 Å observations provide a very regular high temporal resolution data-set with a maximum cadence of 12 minutes. Further, this wavelength is suitable to show active regions as well as quiet Sun regions simultaneously (see Chapter 4). Since in 1996, the cadence of EIT 195 Å data was limited (up to 6 hours) due to telemetry restrictions (Subramanian & Dere 2001), we started the systematic search of PEAs in 1997.

EUV PEAs were identified in the EIT movies according to the following criteria:

---

[1] http://star.mpae.gwdg.de/daily_mpg/

1. Appearances of localized transient brightenings of large-scale loop systems (≈ 5° heliographic length) over the periods of several hours.

2. The large-scale loop systems which were selected had to be observed over their full spatial extents as clearly discernable features with respect to the ambient corona so that their extreme end points could be located.

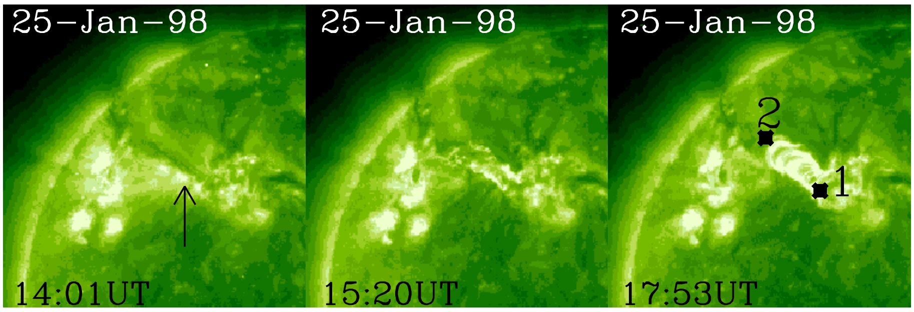

Figure 5.1: Images taken by EIT at 195 Å on 25-Jan-1998. The first two images show the eruption of a prominence (marked with an arrow in the left panel) and consequent post-eruptive arcade formation. The right panel shows the post-eruptive arcade at times of its maximum evolution. Points '1' and '2' represent the two extreme points of the post-eruptive arcade. In the images north points upwards and west towards the right. The images show the north-east quadrant of the solar disk.

These criteria by definition exclude primarily limb events because for most PEAs forming at the limb, the two extreme end points can not be properly located. These criteria also exclude PEA events which had formed after the eruption of polar-crown filaments. Fig. 5.1 shows an example of a PEA identified on 25-Jan-1998 for which the two extreme end points (marked '1' & '2') were located on the solar disk. The PEA formed after a prominence eruption. The arrow in the left panel of Fig. 5.1 indicates the site of the erupting prominence.

Based on the described criteria, 236 PEA events were identified in the time period 1997-2002 and are listed in Table A.1 provided in appendix A.

Fig. 5.2 shows the yearly variation of the total number of identified PEAs (blue colored bars) based on EIT 195 Å movies together with the variation of the yearly averaged sunspot numbers (red colored bars). The number of identified PEAs could have been biased in early 1997 due to telemetry restrictions and from June-December 1998 when SoHO had lost its contact to the operation facilities. The number of identified PEAs increased in the rising phase of solar activity from 1997-2000 and decreased after solar maximum in the years 2001 and 2002. Fig. 5.2 shows a very good correlation of PEA frequency with the sunspot number.

For each identified PEA, its spatial extent based on the located two extreme ends was determined at times around its maximum EUV brightness. For some of the events the high-resolution mvi-format[2] (512 × 512 pixels) data were further

---

[2] ftp://cronus.nrl.navy/mil/net/corona/export/raid2/mvi/daily/

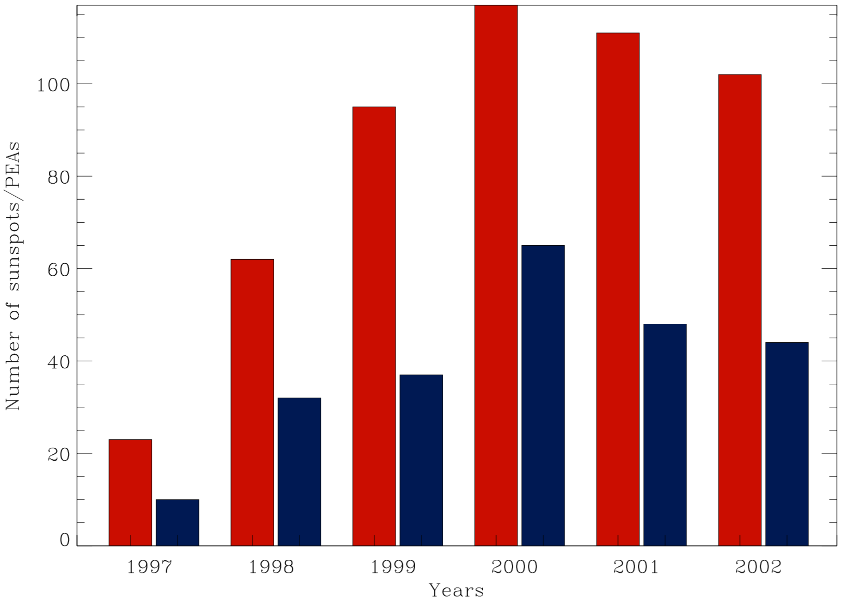

Figure 5.2: Averaged sunspot number (red colored bars) and total number of identified EUV post-eruptive arcades (blue colored bars) from 1997-2002.

studied. Each mvi-file usually contains 120 frames taken 12 minutes apart which provides sequential and continuous observation for the complete day.

The heliographic coordinates of the arcade's extreme ends were determined in latitude and longitude and are listed in the table in appendix A, where (b_1, l_1) and (b_2,l_2) denotes the PEA's end points to the West and East, respectively. The calculation of coordinates for the extreme end points introduces errors in the measurement due to projection effects. However since most PEAs were identified by definition near central meridian, the line-of-sight effects are negligible to first order compared with the full length of the PEAs. The values provided in appendix A can be compared with Fig. 5.1 for the event observed on 25-Jan-1998.

For those PEAs that could be considered as fairly linear features (see Fig. 5.3, left picture) to first order, (b_1, l_1), (b_2, l_2) represent the endpoints of the mid axis of the arcade. Sometimes PEAs appeared rather curved shaped (see Fig. 5.3, right picture). In such cases the coordinates of the middle point of the PEAs (denoted as '3' in the right panel of Fig. 5.3) were also calculated.

The analysis of the high resolution data was based on IDL (Interactive Data Language). Naval Research Laboratory (NRL) provides a library containing data analysis packages written in IDL for LASCO and EIT data. Complementary programs included in the Solar Software (SSW) were further used for the data analysis.

5.3 Photospheric Magnetic Field Data

In order to study the underlying photospheric field signatures of each PEA, magnetograms from the SoHO/MDI (Michelson Doppler Imager, Scherrer et al. 1995)

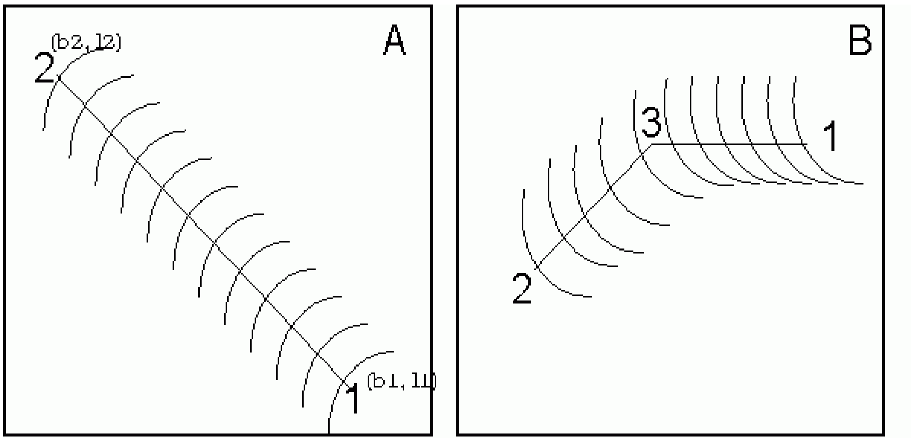

Figure 5.3: Left panel: Schematic diagram showing a linearly appearing post-eruptive arcade. Right Panel: Schematic diagram showing a curved shaped appearing post-eruptive arcade.

instrument were used. The synoptic charts[3] are produced from the definitive magnetograms taken around central meridian. For simplicity, no considerations of the time differences between the arcade occurrences and the observation dates of single magnetograms that contributed to the individual synoptic maps were taken into account. This implies that arcade events identified in the eastern solar hemisphere had appeared in time before the magnetogram observations were taken, whereas western hemisphere events had followed the magnetogram observations. An example of MDI magnetogram synoptic chart produced for Carrington Rotation 1948 is shown in Fig. 5.4. A Carrington Rotation covers a time period of 27.3 days, representing one full rotation of the Sun as seen from Earth. Carrington Rotation numbers are referenced to the time they were introduced first on November 9, 1853 (Carrington 1863) and counted every 27.3 days as one Carrington Rotation.

In the image shown in Fig. 5.4 the white color represents the positive magnetic polarity (field lines pointing outward from the photosphere) and the black color represents negative magnetic polarity (field lines pointing towards the photosphere). Each PEA axis was plotted on top of the synoptic charts by converting the heliographic coordinates into the corresponding Carrington coordinates. In Fig. 5.4, the axes of all identified PEAs during Carrington Rotation 1948 are shown.

The magnetic polarities on both sides of each PEA's axis were inferred from the magnetograms and are provided in the second last column in Table of appendix A. The position of the PEA axes in the synoptic charts provided informations on the photospheric magnetic field configurations in the source regions of the associated CMEs.

Through application of the above described techniques we inferred the basic physical properties of PEAs and the photospheric magnetic field configurations of their source regions. The obtained results are discussed in detail in Chapter 6.

---

[3] http://soi.stanford.edu/magnetic/index5.html

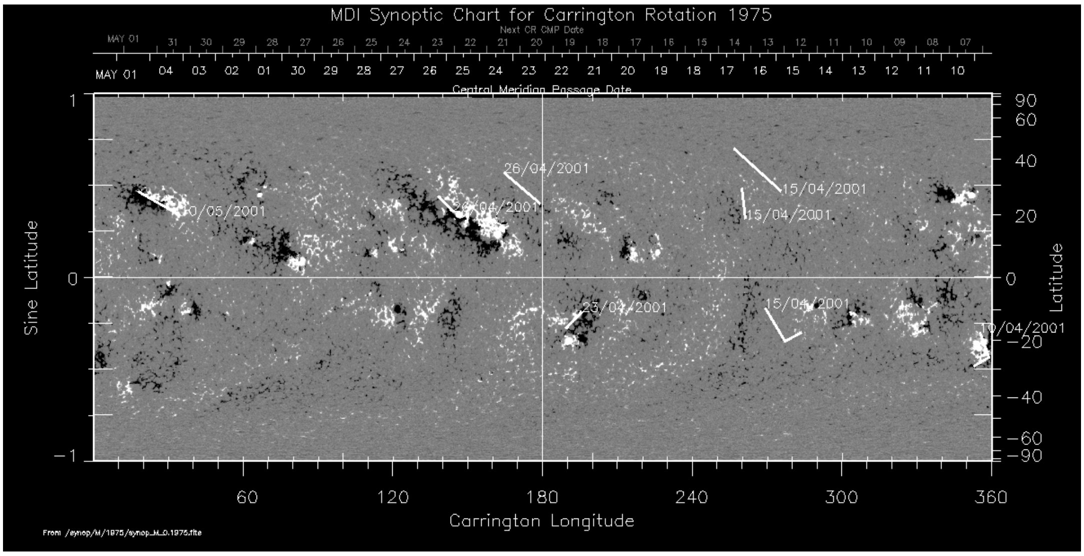

Figure 5.4: MDI magnetogram synoptic chart for Carrington rotation 1948 covering the time period 4 to 30-Apr-1999. The long axes of the identified PEAs are labeled with solid white lines. The white colors show the positive magnetic polarities and black colors correspond to the negative polarities. Courtesy: SoHO/MDI consortium.

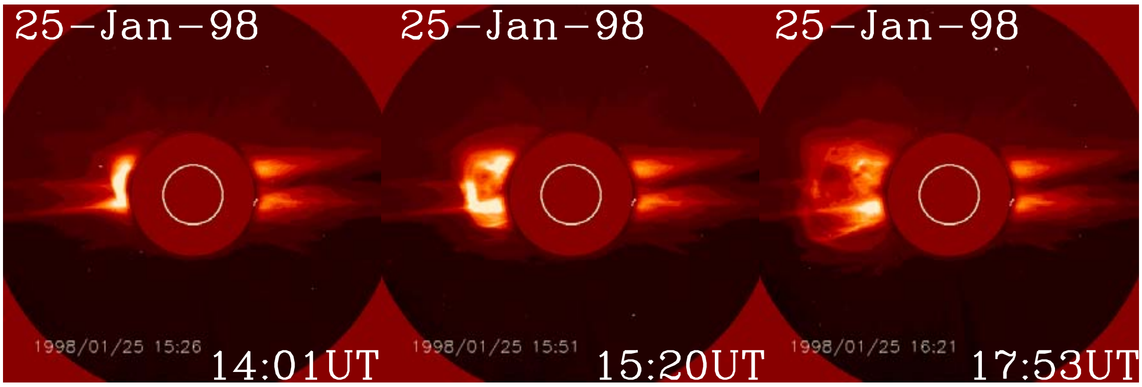

Figure 5.5: SoHO/LASCO/C2 white-light images showing the coronal mass ejection at the East limb associated with the post-eruptive arcade shown in Fig. 5.1. Courtesy: SoHO/LASCO consortium.

5.4 Correlation of PEAs with CMEs

One of the main goals of this study is to investigate the underlying source regions of CMEs. For this purpose the correlation of PEAs with CMEs was studied using data from the SoHO/LASCO coronagraphs. An example of a CME detected by LASCO/C2 which was associated with the PEA on 25-Jan-1998 is shown in Fig. 5.5. The CME was first seen at 14:01 UT in the LASCO/C2 field-of-view (FOV).

The spatial correlation of PEAs with CMEs was investigated by comparing the CME's position angle (PA) as provided by the CME catalogue[4] (Yashiro et al. 2002) with the solar positions of the related PEAs (see, e.g. Fig. 5.5). The PA is measured positive in the counter-clockwise direction, starting with zero degrees at solar North

---

[4] http://cdaw.gsfc.nasa.gov/CME_list/

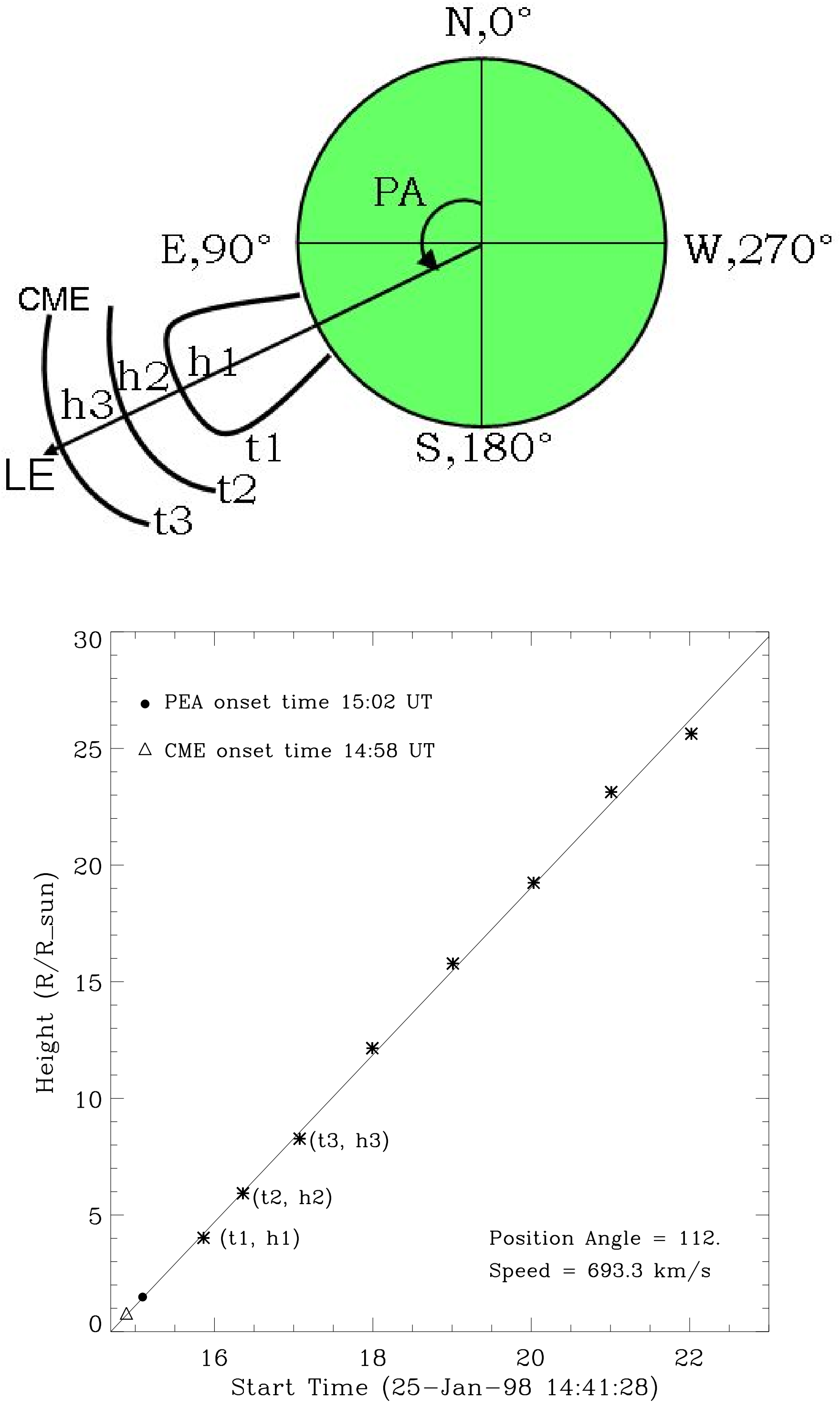

Figure 5.6: Top panel: Schematic representation of position angle measurements. LE denotes the leading edge of the CME. Bottom panel: Height-time diagram for the LE of the CME observed on 25-Jan-1998 as provided by LASCO C2 and C3. h1 is the height measured at time t1, h2 is the height measured at time t2 and so on.

as illustrated in the top panel of Fig. 5.6. A spatial correlation itself does not always ensure that a particular CME was indeed associated with a given PEA. Therefore, in order to prove the association of a given PEA with a CME detected by LASCO/C2, the temporal correlation of both phenomena was further investigated by comparing the observation time of the PEA with the height-time (ht) diagram of the CME taken from the CME catalogue, including both LASCO C2 and C3 (FOV 2.0-6.0 $R_\odot$ & 4.0-30 $R_\odot$) measurements. The height-time diagrams were produced by measuring the height evolution of the leading edge of the CME with respect to the solar limb as illustrated in Fig. 5.6 (top and bottom panel). The time of the first detection of each related CME in C2 is specified in the last column of the table in Appendix A. From backward extrapolation of the h-t diagrams the approximate CME onset times were estimated and compared with the estimated onsets of the corresponding PEA events. The bottom panel of Fig. 5.6 represents an example of a height-time diagram for the event on 25-Jan-1998 obtained from the CME catalogue. The approximate CME and PEA onset times are labeled in the plot. The plot shows that the onset of the PEA was seen shortly in time after the estimated CME onset.

Sometimes, for further study of the CME associations, we used the running difference image technique. In this technique, the intensity difference between consecutive white-light coronal images, obtained with the LASCO coronagraph are displayed. Black-and-white areas then show the relative spatial variations of motions (Sheeley et al. 1999). The obtained results on the association of EUV PEAs with white-light CMEs is discussed in detail in Chapter 7.

5.5 Image Processing Using Wavelets

In a specific event of the PEAs list provided in the table in appendix A, a bright coronal inflow was discovered in the EIT FOV as described in Chapter 8 in detail. In order to study the evolution of the erupting prominence, the associated CME and the inflow we performed height and speed measurements of different identified specific features in the FOV of EIT, LASCO/C2 and LASCO/C3. For this purpose, a reliable and accurate image analysis technique is needed especially to make precise measurements of spatial positions and speed profiles. A straight forward technique would be to cross-correlate a particular sub-region in consecutive images, provided sharp and fixed features are present in the sub-region considered. However the white-light features often lack the necessary sharpness to obtain positive results (Stenborg & Cobelli 2003).

The images taken by EIT and LASCO were thus processed in order to enhance the contrast of the visible fine-scale features by applying a wavelet decomposition technique established by Stenborg and Cobelli (2003). The method is based on the work by Fligge & Solanki (1997) and Starck et al. (1997). In the wavelet transform, the basis functions are highly localized (compactly supported). Although it is a linear transform, it is not an inverse of itself like the Fourier transform. Such an application corresponds to a wavelet packet analysis which allows finer detail structure to be processed. This increases the redundancy in the transformed plane which is essential to the identification of hierarchical structures in the individual

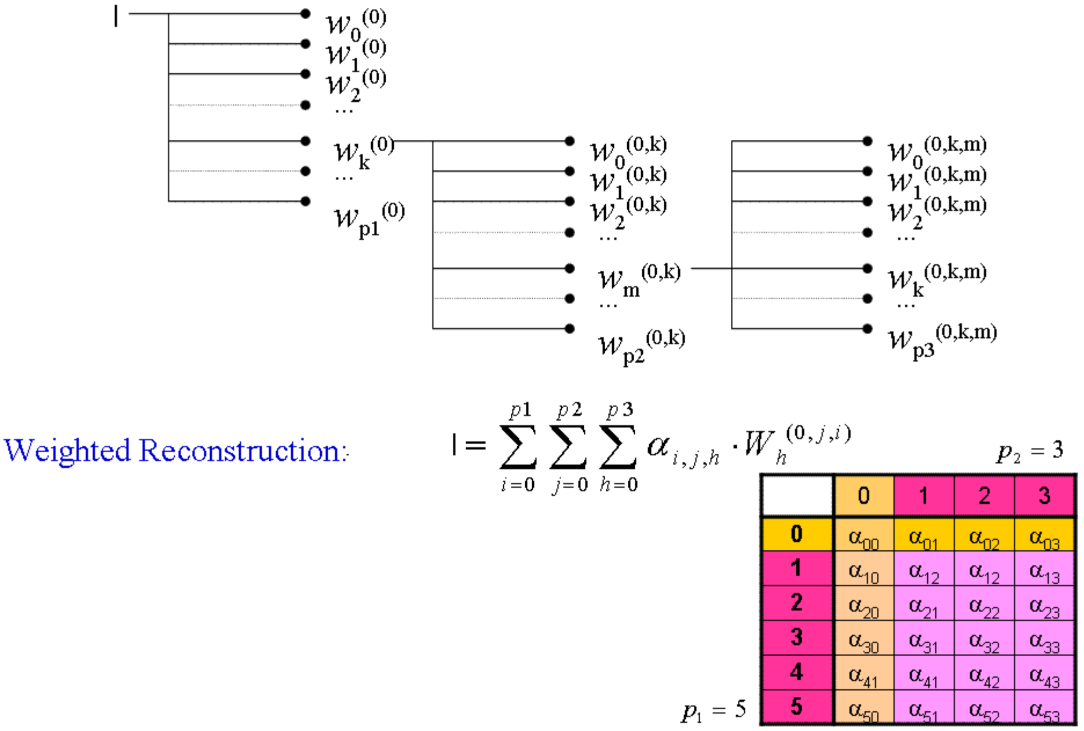

$$I = \sum_{i=0}^{p1} \sum_{j=0}^{p2} \sum_{h=0}^{p3} \alpha_{i,j,h} \cdot W_h^{(0,j,i)}$$

	0	1	2	3
0	α_{00}	α_{01}	α_{02}	α_{03}
1	α_{10}	α_{12}	α_{12}	α_{13}
2	α_{20}	α_{21}	α_{22}	α_{23}
3	α_{30}	α_{31}	α_{32}	α_{33}
4	α_{41}	α_{41}	α_{42}	α_{43}
5	α_{50}	α_{51}	α_{52}	α_{53}

Figure 5.7: Schematic illustration of the wavelet packet application. Courtesy: G. Stenborg.

image. The algorithm used in the processing of the images was the 2D- á trous transform (Shensa 1992). Most of the noise in the image is then concentrated in the high frequency scale in the wavelet plane. A weighted reconstruction scheme is employed in which during the process of reconstruction considerably less weight can be given to the scale containing noise.

Fig. 5.7 illustrates the wavelet decomposition technique (Stenborg & Cobelli 2003). In the figure, 'I' is considered as an original image. The first level decomposition of the image 'I' into p scales gives rise to the wavelet transform set W_i^0, where i = 0, 1, 2,.....p0 are the wavelet planes. The zeroth plane corresponds to the continuum and 1, 2....p corresponds to the frequency scales. In this algorithm the lower the value of i, the higher is the frequency scale in the wavelet plane. These planes can be further decomposed into finer wavelet scales. This decomposition leads to the tree structure as shown in Fig. 5.7. Further, the images can be constructed by giving high weight to the low frequency scales and less weight to the high frequency scales, in order to get rid of the noise. Based on the formula given below the images were reconstructed.

$$I(x,y) = \sum_{i=0}^{p1} \sum_{j=0}^{p2} \sum_{h=0}^{p3} \alpha_{i,j,h} W(x,y)_h^{(0,j,i)}$$

where α is the weight and W are the wavelet planes. Further details about the algorithm and this technique can be found in Stenborg & Cobelli (2003).

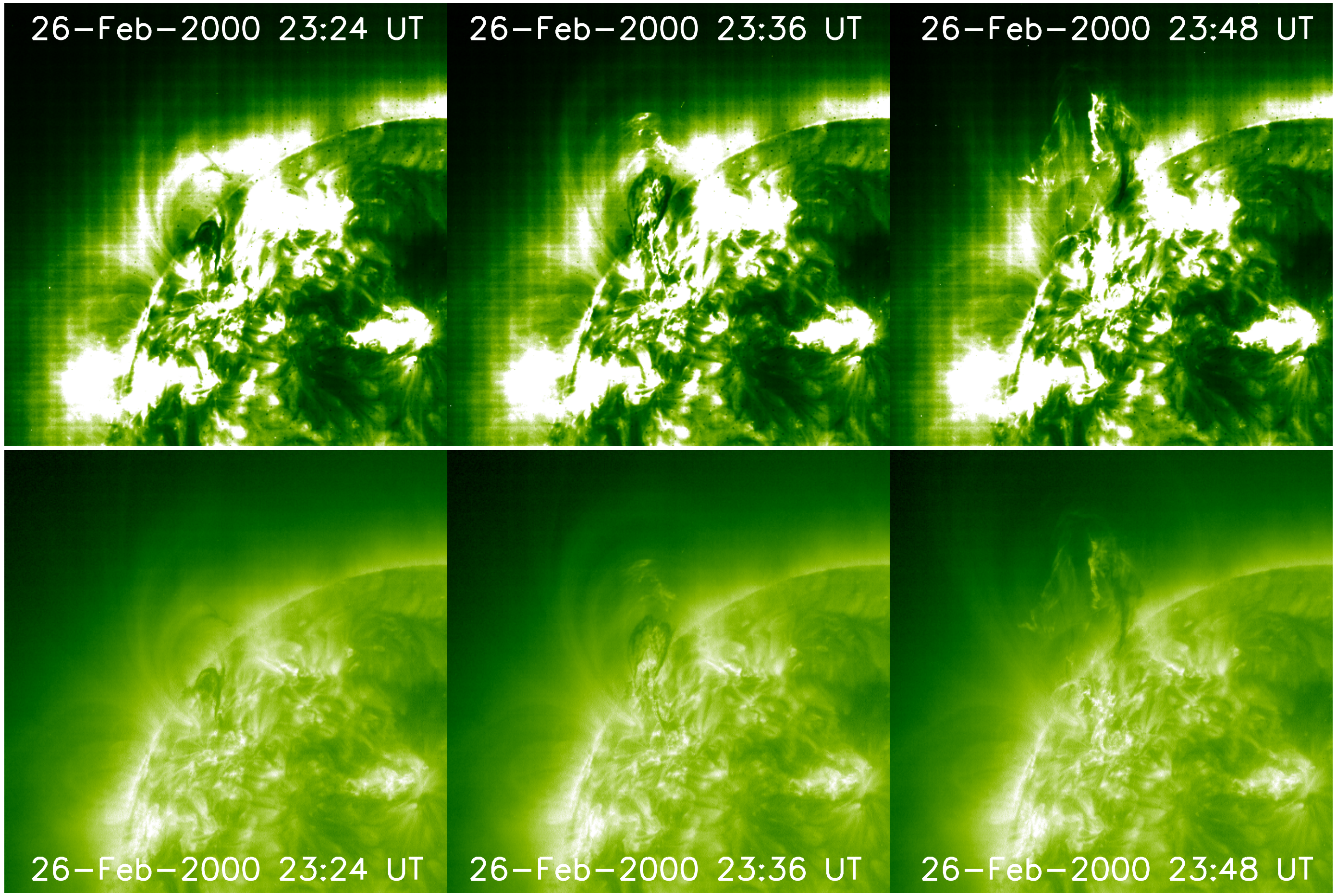
26−Feb−2000 23:24 UT
26−Feb−2000 23:36 UT
26−Feb−2000 23:48 UT
26−Feb−2000 23:24 UT
26−Feb−2000 23:36 UT
26−Feb−2000 23:48 UT

Figure 5.8: Top panel: Raw images taken by EIT at 195 Å on 26-Feb-2000. Bottom panel: Corresponding wavelet processed images.

Fig. 5.8 shows the raw (top panel) and wavelet processed (bottom panel) images taken by EIT at 195 Å on 26-Feb-2000 at 23:24, 23:36 and 23:48 UT. The loops overlying to the prominence can best be seen in the wavelet processed images.

The wavelet packet analysis technique has been applied to the images obtained from EIT, LASCO/C2&C3 for the event on 05-Mar-2000. The obtained results are discussed in detail in Chapter 8.

5.6 Remapping of MDI Magnetograms

Based on the PEA events listed in the table provided in Appendix A, we have selected those cases in which the erupting filament seen in EIT 195 Å was associated with EUV PEAs together with Hα filtergrams allowing a detailed study of the evolution of magnetic flux in the source region. The selected events are marked by superscript '2' in this table.

To avoid LOS effects, only those events were selected , which were located near the central meridian in the latitude and longitude range of $\pm 40°$ and with a length equal or greater than 10°. Based on these criteria seven events were selected. For each events, five-minute averaged MDI magnetograms with a time cadence of 96 minutes were analyzed. The magnetogram data were investigated in time starting from the day before the eruption until the day after.

The MDI magnetograms provide observations of the longitudinal component (line-of-sight) of the magnetic field. These measurements are highly affected by projection effects. The region which is on the intersection of the central meridian and the equator is least affected.

In order to remove any projection effects, the program *map_carrington.pro* from the SSW library was used. This routine projects a solar image onto a rectangular area preserving heliographic longitudes and latitudes. The remapped image has larger size than the full disk image (see Fig. 5.9). The projection is referred to as Carrington projection. After remapping of the images, the meridians and latitude lines are perpendicular to each other in the processed image. Fig. 5.9 shows an example of a full disk magnetogram (top panel) obtained from SoHO/MDI and its corresponding remapped image (bottom panel).

Finally, a rectangular sub-area of interest was selected based on observations of the corresponding erupting filaments in EIT and Hα images and the locations of the CME's source regions provided by the corresponding PEAs. The diagonal of the rectangles corresponded to the spatial extent of the erupting filaments. Finally we tracked the area of interest for three consequtive days starting a day before until the day after the solar eruption by compensating the effects of solar differential rotation. The rotation period varies from about 25 days near the equator to 30 days near the pole. The differential rotation was fitted by the following formula (Zirin 1987)

$$\Omega(\theta) = 14.42 - 2.30 sin^2\theta - 1.62 sin^4\theta (deg/day)$$

with Ω being the rate of rotation in degrees per day and θ being the corresponding heliographic latitude.

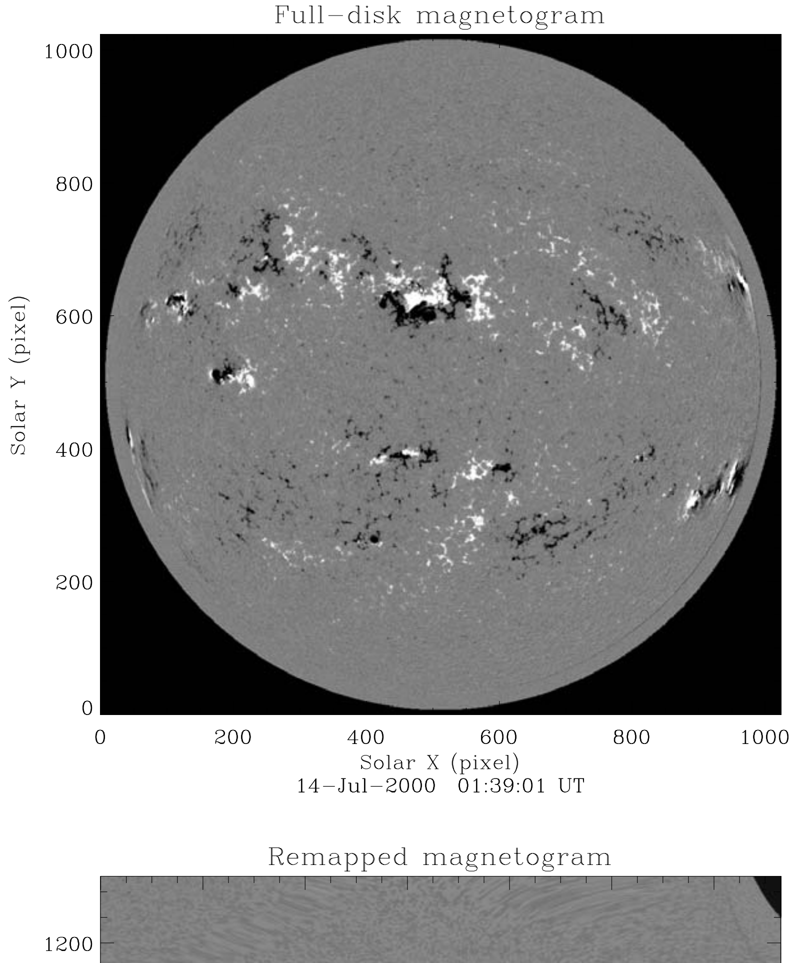

Figure 5.9: Top panel: Full disk magnetogram taken by MDI on 14-Jul-2000. Bottom panel: Remapped magnetogram. Note that after remapping, both the X and Y size has been increased and that the heliographic coordinates are preserved.

The technique has been applied to all the seven selected events located near disk center. The results are described in Chapter 9.

6 Properties of EUV Post-Eruptive Arcades

In this chapter we present an overview of the basic physical properties of post-eruptive arcades detected by the EIT at 195 Å. Based on the observations of the MDI magnetogram synoptic-charts the photospheric magnetic field configuration in the source regions of the PEAs are investigated. Additionally the characteristic dependence of post-eruptive arcades during a part of solar cycle 23 is examined.†

6.1 Introduction

Post-eruptive arcades (PEAs) are transient large-scale loop systems that are observed to form in the corona in association with solar eruptions. Fig. 6.1 displays an example of a PEA located near the central meridian in the northern hemisphere. The filament eruption was observed at around 13:13 UT. The identified onset time of the corresponding PEA at 195 Å in the EIT images was 14:14 UT, showing its maximum development around 14:36 UT and disappearing at about 16:00 UT.

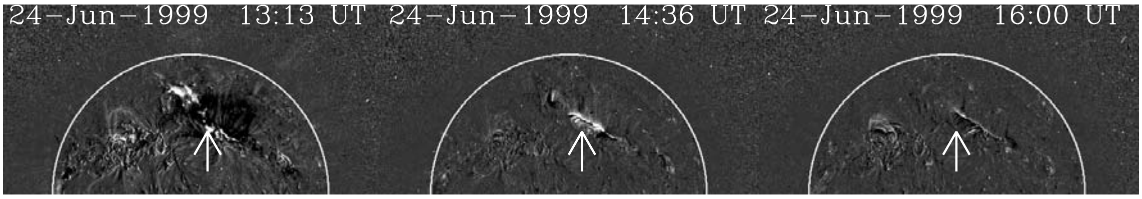

Figure 6.1: EIT running difference images taken by EIT at 195 Å on 24-Jun-1999. The first two images show the erupting prominence and consequent post-eruptive arcade formation. The last image reveals the dimming of the arcade. The site of the filament eruption and arcade formation is marked by arrow in the corresponding images. Images show the northern hemisphere of the Sun. In all images north is up and west is towards the right.

Fig. 6.2 shows a schematic representation of the formation of a PEA according to the model proposed by Kopp and Pneuman (1976). In this model it is assumed that the arcade-like loop system forms as a consequence of magnetic reconnection processes in the corona. In this interpretation it is assumed that prior to the eruption, originally the underlying photospheric bipolar region comprised of closed magnetic field lines holds down the filament/prominence (Fig. 6.2 a, b). Through the sudden release of mass and energy during the eruption, the field lines open up and an open bipolar field geometry with a magnetic neutral sheet forms (Fig. 6.2 c). As the field lines open up, the plasma begins to flow upwards from the chromosphere to the corona decreasing the gas pressure. Therefore the magnetic pressure starts dominating. The dominating magnetic pressure then leads to sequential reconnections of open magnetic field lines creating new loops (Fig. 6.2 (d)). The magnetic reconnection produces heating at the top of the new loops being conducted downward to the chromosphere. The reconnection process also accelerates particles which flow along the loops to their foot-points. The heated gas at chromospheric foot-points finally evaporates into the newly formed loops, being visible in X-rays and EUV wavelengths. The newly formed loops are commonly called post-eruptive arcades or post-flare loops (e.g., Cargill & Priest 1983; Forbes & Malherbe 1986). The reconnection processes continues while the already formed loops cool down. Repeated reconnection processes can lead to the growth of the entire loop system. There are several other models which explain the formations of loop systems after eruptions in similar manner (e.g., Lin and Forbes 2000; Linker et al. 2003).

---

† The content of this chapter has been published in Astronomy and Astrophysics, V. 422, p. 337-349, 2004.

The development of transient loop systems has been frequently observed also in soft X-rays in association with disappearing filaments seen in Hα, with life-times varying from 3-40 hours (Webb, Krieger & Rust 1976). In this chapter the basic physical properties of EUV PEAs will be described. Finally the photospheric magnetic field configuration in the source regions of PEAs and their solar cycle variations are examined.

6.2 The Basic Properties of PEAs

6.2.1 EIT 195 Å Emission Lifetime

For each of the PEA events listed in appendix A, the time interval was determined over which the EUV arcade could be clearly distinguished at EIT images at 195 Å. The time cadence of the images was usually 12 min. The start time of an arcade event was defined as the time when the large-scale loop system could be identified the first time in an EIT image and the end time was simply defined as the time when the loops could not be distinguished anymore in the EIT images. All estimated lifetimes are listed in appendix A. Fig. 6.3 shows the EIT 195 Å lifetime distribution of the identified PEAs during 1997-2002 in bins of 2 hours. The typical lifetimes of EUV PEAs ranged from less than one hour to more than 15 hours, with an average lifetime of 7 ± 2 hours. Most PEAs had lifetimes of 2-6 hours.

6.2.2 Heliographic Positions, Spatial Lengths and Latitude Variations

For each identified PEA, two extreme points (b_1, l_1) and (b_2, l_2) of the loop system's long axis were estimated as described in Chapter 5. The derived values are listed in the table of appendix A. Fig. 6.4 displays the calculated heliographic positions

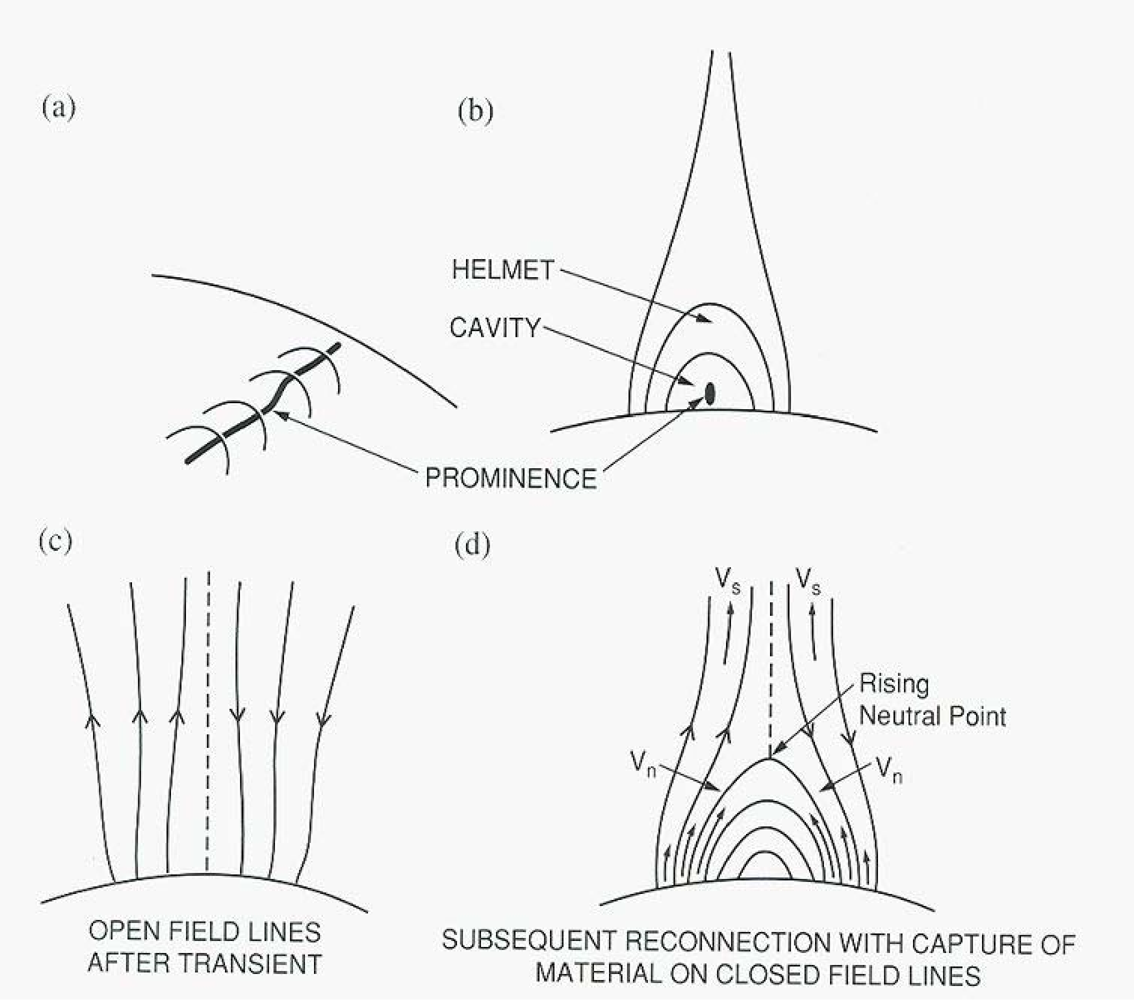
(a)
(b)
HELMET
CAVITY
PROMINENCE
(c)
(d)
V_s
V_s
Rising Neutral Point
V_n
V_n
OPEN FIELD LINES AFTER TRANSIENT
SUBSEQUENT RECONNECTION WITH CAPTURE OF MATERIAL ON CLOSED FIELD LINES

Figure 6.2: A possible interpretation of the post-eruptive arcades. (a, b) Two different views for pre-eruption configuration when a filament (prominence) extends along a polarity inversion line and is embedded in a closed magnetic structure. (c) Opening of magnetic field lines during the eruption. (d) Closing down of the magnetic fields and the formation of post-eruptive arcades (after Kopp and Pneuman 1976; adopted from Svestka 2003).

of all PEAs identified during the years 1997 to 2002 in a single Carrington map. Most of the PEAs formed in the heliographic latitude range ±40° North and South with respect to the equator, transequatorial cases were extremely rare. No PEA was observed at latitudes above ±60° North or South. The orientation of the PEA axes is similar Joy's law derived for the tilt of the magnetic axis[1] of sunspots (Hale et al. 1919), i.e. the tilt angle of sunspots is half of the corresponding latitude at which they are located. For example, a sunspot at 60° North would be expected to have a tilt of about 30°, as measured from East towards North. The tilt angles in sunspots are measured positively from the equator towards North in the northern hemisphere and vice versa in the southern hemisphere.

---

[1] Sunspots generally form in magnetically-linked bipolar groups, with each end being one pole of a localized magnetic field. The polarity inversion line between two polarities is called the magnetic axis of sunspot.

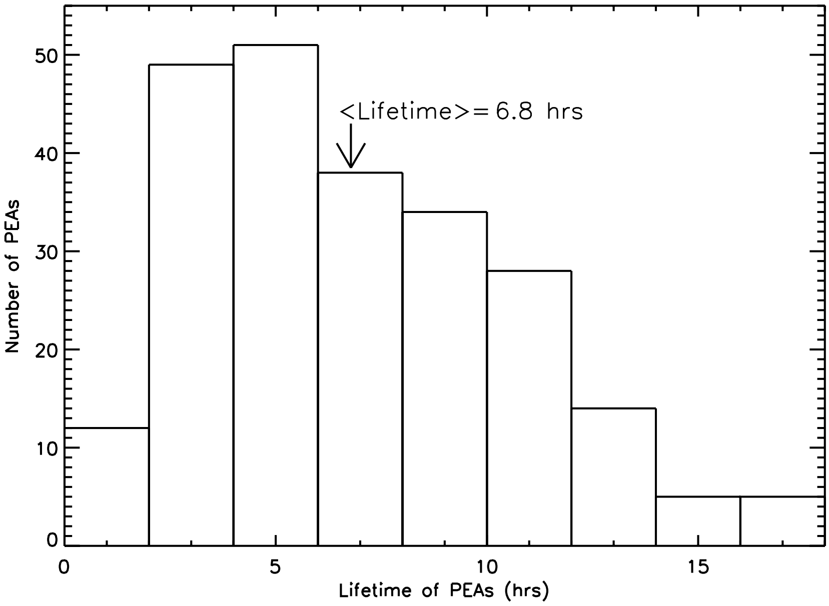

Figure 6.3: Frequency distribution of the lifetimes of the identified PEAs during 1997-2002 based on SoHO/EIT 195 Å observations in bins of 2 hours. The average value for the lifetime was about 6.8 ± 2 hours (From Tripathi et al. 2004).

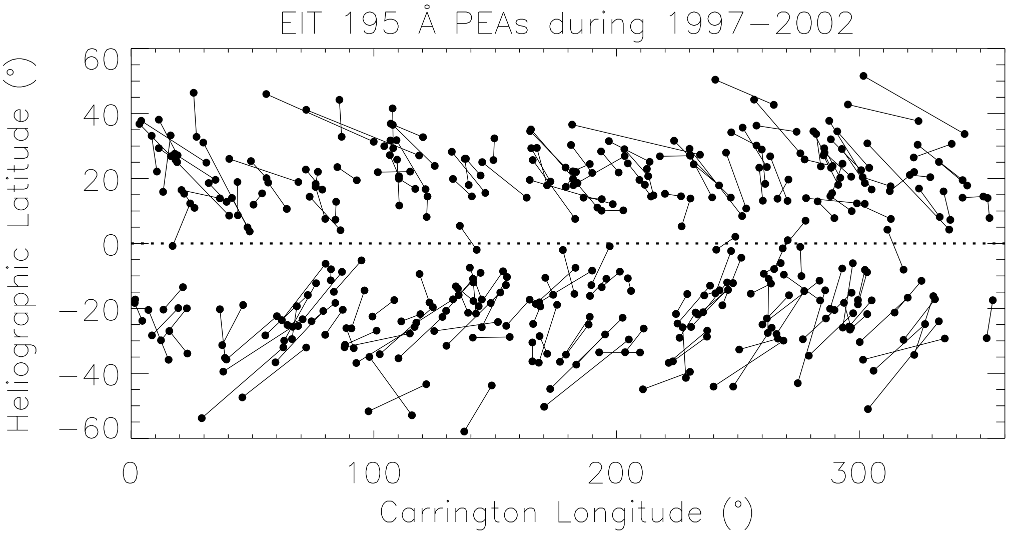

Figure 6.4: Carrington synoptic map representing the positions of all identified PEAs during 1997-2002 based on the analysis of SoHO/EIT 195 Å observations (From Tripathi et al. 2004).

Based on the heliographic coordinates (b_1, l_1) and (b_2, l_2) of the two end points of PEAs the length (L) of a given PEA event was calculated by applying the cosine formula in a spherical triangle (Smart 1944).

The length (L) of a given PEA event is give as:

$$L = \arccos\left(\sin(b_1)\ \sin(b_2) + \cos(b_1)\ \cos(b_2)\ \cos(l_1 - l_2)\right)$$

Fig. 6.5 shows the frequency distribution of the calculated lengths of the PEAs.

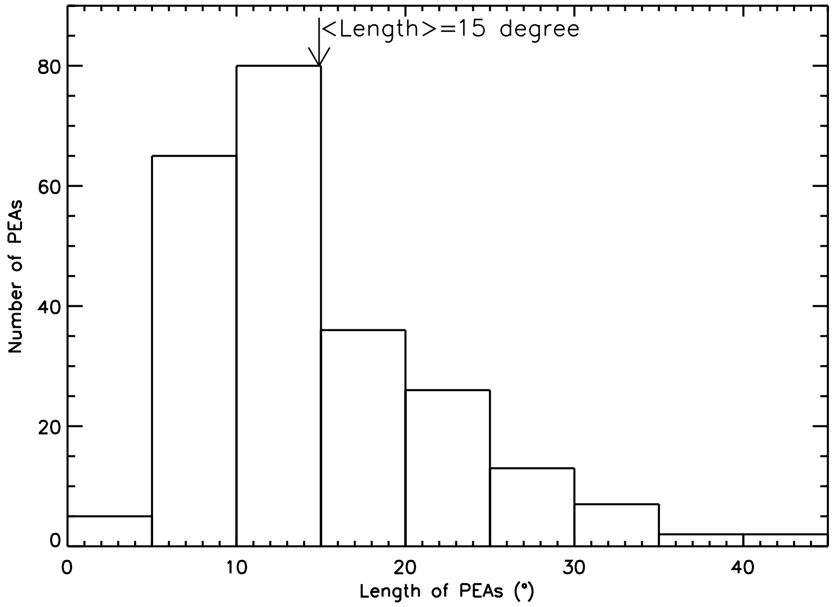

Figure 6.5: Distribution showing the frequencies of the heliographic lengths of PEAs identified from SoHO/EIT 195 Å images during 1997-2002 in bins of 5°. The average length of the identified PEAs was 15° ± 4° (From Tripathi et al. 2004).

For the calculation of lengths, the PEAs were considered to first order as linear features. The length of the PEAs varied from less than 2 degrees to more than 40 degrees, with an average value of 15° ± 4°. Most of the PEAs had lengths of 5 to 15 degrees. As indicated by Fig. 6.4, PEAs substantially exceeding the average length seemed to have formed preferentially at higher heliographic latitudes. The length variation with heliographic latitude in both solar hemispheres is shown in Fig. 6.6. When plotting the heliographic latitude in Fig. 6.6 the mid point of the PEA axes was taken into account. From a linear polynomial fit it is found that the length (L) of PEAs increases with latitude in the northern hemisphere as L_N(deg) = 2.9 (b - 17.1) and in the southern hemisphere as L_S(deg)= - 1.6 (b + 13.4), with b being the heliographic latitude. For latitudes of 20, 30 and 40 degrees North and South this corresponds to PEA lengths of 8, 37 and 66 degrees in the North, and 11, 27 and 43 degrees in the South. Since PEAs can be considered as tracers of the source regions of CMEs, this finding may imply that the longitudinal extension of CMEs increases with heliographic latitude (see Chapter 7). The increase of the PEA length with latitude appears to be associated with the larger sizes of disappearing filaments at higher latitudes.

6.3 Photospheric Source Regions and Solar Cycle Dependence

The estimated heliographic position for each PEA was used to locate its photospheric source region in the SoHO/MDI magnetogram synoptic charts taken during the

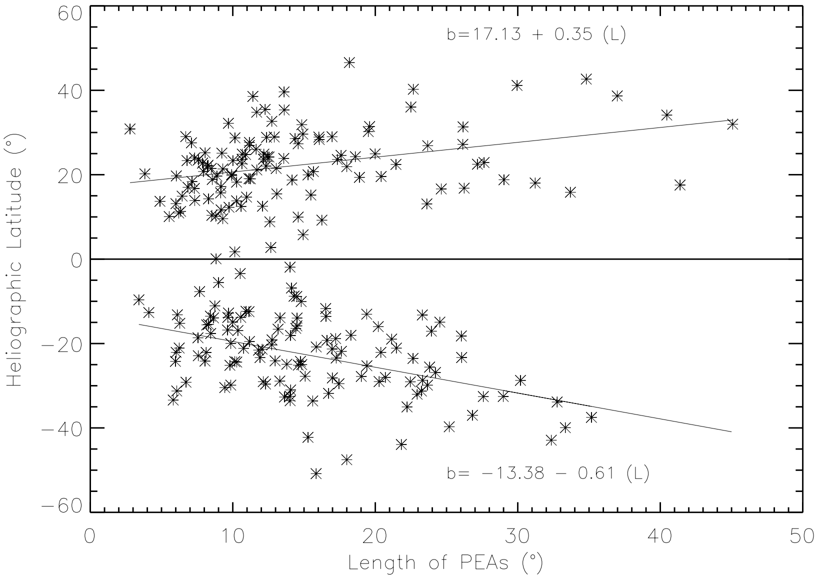

Figure 6.6: Variation of PEA length with heliographic latitude during 1997-2002. The data points represent the latitude for the midpoint of the PEA axes. Note that no events were identified above 60° latitude. The straight lines represent the fitted latitudinal trends in both solar hemispheres in the range 20 to 40 degree latitude: L_N(deg) = 2.9 (b -17.1) and L_S(deg)= - 1.6 (b + 13.4), with b being the heliographic latitude of the mid point of a PEA axis. Positive values of the latitude correspond to the northern hemisphere (From Tripathi et al. 2004).

corresponding CR (Carrington Rotation) as explained in Chapter 5. Fig. 6.7a,b show the positions of the ten EUV arcades identified in CRs 1928 and 1963. White and black colors in the magnetograms represent positive (field lines pointing away from the photosphere) and negative (field lines pointing towards the photosphere) magnetic polarities. The solid and dashed lines in Fig. 6.7 mark the calculated PEA long axis positions of the three identified PEAs of CR 1928 and the seven of CR 1968. The axes positions matched the positions and orientations of polarity inversion lines (PILs, neutral lines) separating regions of opposite magnetic polarities in bipolar regions in both solar hemispheres similar to the finding of Subramanian & Dere (2001) who studied the photospheric source regions of a number of CMEs detected by SoHO/LASCO.

Fig. 6.7a shows data from October 1997, i.e. at times of the rising phase of solar cycle 23, and Fig. 6.7b shows data for June 2000, i.e. during time period around solar maximum. The number of active regions and the photospheric magnetic flux is considerably higher near solar maximum. This difference is also reflected by the much higher number of PEAs identified in CR 1968. The comparison of the EIT and MDI observations yielded that PEAs either comprised an entire PIL (Polarity Inversion Line) of a bipolar region (Fig. 6.7a, case i) or just a fraction of it (Fig. 6.7a, case j). Besides the cases in which PEAs had formed associated with specific single BPRs, some PEAs were also found to be located in between two neighboring bipolar regions (see Fig. 6.7a(k)).

The different underlying magnetic configurations are sketched in Fig. 6.8, in analogy to the configurations suggested by Tandberg-Hanssen (1974, p. 118). The

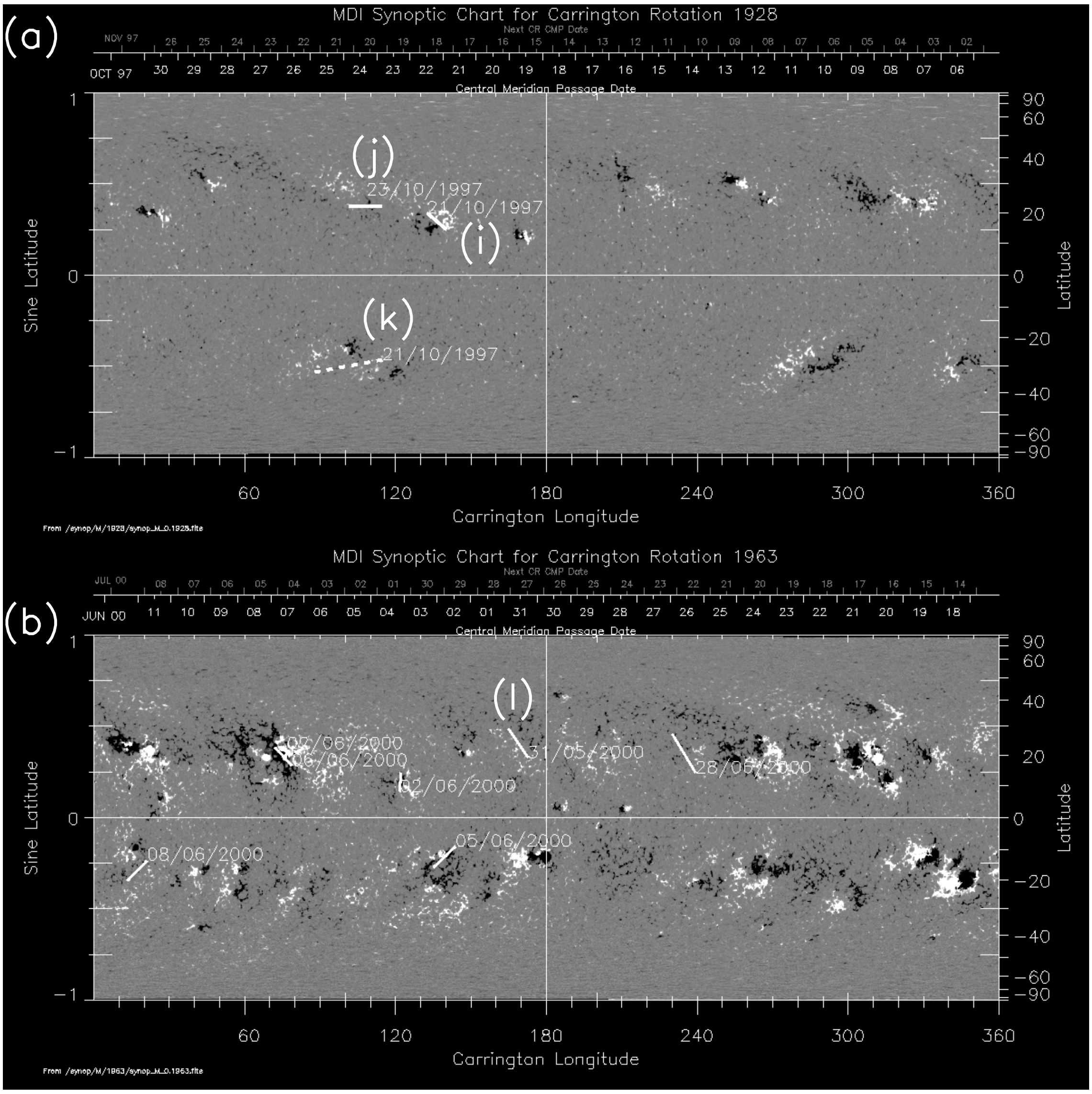

Figure 6.7: SoHO/MDI Carrington synoptic charts for rotations 1928 (a) in 1997 and 1963 (b) in 2000 and identified source regions of ten post-eruptive arcades (PEAs), marked by solid and dashed lines. In the synoptic charts, white colors represent areas of positive magnetic polarity, black colors those of negative polarity. Note, that in the North the leading areas of bipolar regions reveal predominantly positive magnetic polarities in this cycle and vice versa in the South. The solid and dashed lines represent the individual PEA axes. Cases i) & j) indicate linear shaped PEAs. A PEA located in between two bipolar regions is labeled as k) and a case untypical for the dominant polarity in the northern hemisphere in cycle 23 as l) (From Tripathi et al. 2004).

presence of a filament is assumed in both configurations, although it is not necessarily required. The magnetic polarities on both sides of the PILs were predominantly the ones expected for cycle 23, with leading positive polarities in the sense of solar rotation in the North and leading negative polarities in the South. However some of the PEAs formed in regions of reverse polarity configurations as compared to the dominating pattern in this solar cycle (e.g., Fig. 6.7b(l)).

Out of the 236 PEA events studied, in 216 cases the magnetic polarities on both sides of the arcade's axis could be uniquely identified. The remaining events occurred at latitudes above 40° or in regions with very diffuse as well as highly complex photospheric fields that made the field determinations doubtful. In other cases MDI data were not available. The spatial distribution of the 216 PEAs in heliographic coordinates and their magnetic polarities between 1997 and 2002 are displayed as yearly Carrington maps in Fig. 6.9. The color of each point at the lower latitude end of each PEA axis represents the magnetic polarity to the West of the polarity inversion line in the sense of solar rotation, with the red color labeling positive (N) magnetic polarity and the blue color labeling negative (S) magnetic polarity.

Fig. 6.9 shows that the number of PEA events increased until solar maximum in 2000 and then remained at a higher level in 2001 and 2002. However, it should be noted that high latitude PEAs are probably lacking because of the selection criteria for the events which require the PEA to be observable over their full spatial extent. The clustering of PEAs in some years at specific Carrington longitudes (e.g., near 250 degrees in 2000) may be compared with the clustering of active regions in the rising to maximum phase of solar cycle 23 as pointed out by Pojoga & Cudnik (2002) and the appearance of longitudinal bands of active regions as reported by Benevolenskaya et al. (1999).

The yearly variation of the respective magnetic polarities found West of the neutral lines (PILs) in each solar hemisphere during 1997-2002 is presented in Fig. 6.10. As noted earlier, the expected sign of the leading magnetic polarities of BPRs is expected to be positive in the northern hemisphere and vice-versa in the southern hemisphere (compare with Fig. 6.7a,b). Out of the 216 events in Fig. 6.10a, 111 events were seen in the North (solid black line) and 105 in the South (solid black line), i.e. the distribution was about equal in both hemispheres. In the plot, NH stands for northern hemisphere and SH for southern hemisphere. The maximum number of PEAs peaks in both hemispheres at times of solar maximum in 2000. In the northern hemisphere 81 (73%) out of 111 PEAs and in the southern hemispheres 63 (60%) out of 105 matched the expected magnetic polarity (dashed lines in Fig. 6.10a). However, a fraction of the events showed reversed polarities (dotted lines). Some of the PEA events with reversed polarities were formed in the magnetic regions with quadru-polar configurations (QPS). QPS cases have been subtracted in the numbers provided in Fig. 6.10(b). The refined consideration reveals, that the expected magnetic polarity dominance for cycle 23 is getting more close to the total number of events, but still with a minority of reversed cases in both hemispheres. It should be noted that a hemispheric asymmetry in the distribution of evolving photospheric magnetic flux, as supported by the results of Li et al. (2002) who found more sunspot groups appearing in the northern hemisphere of the Sun in the rising

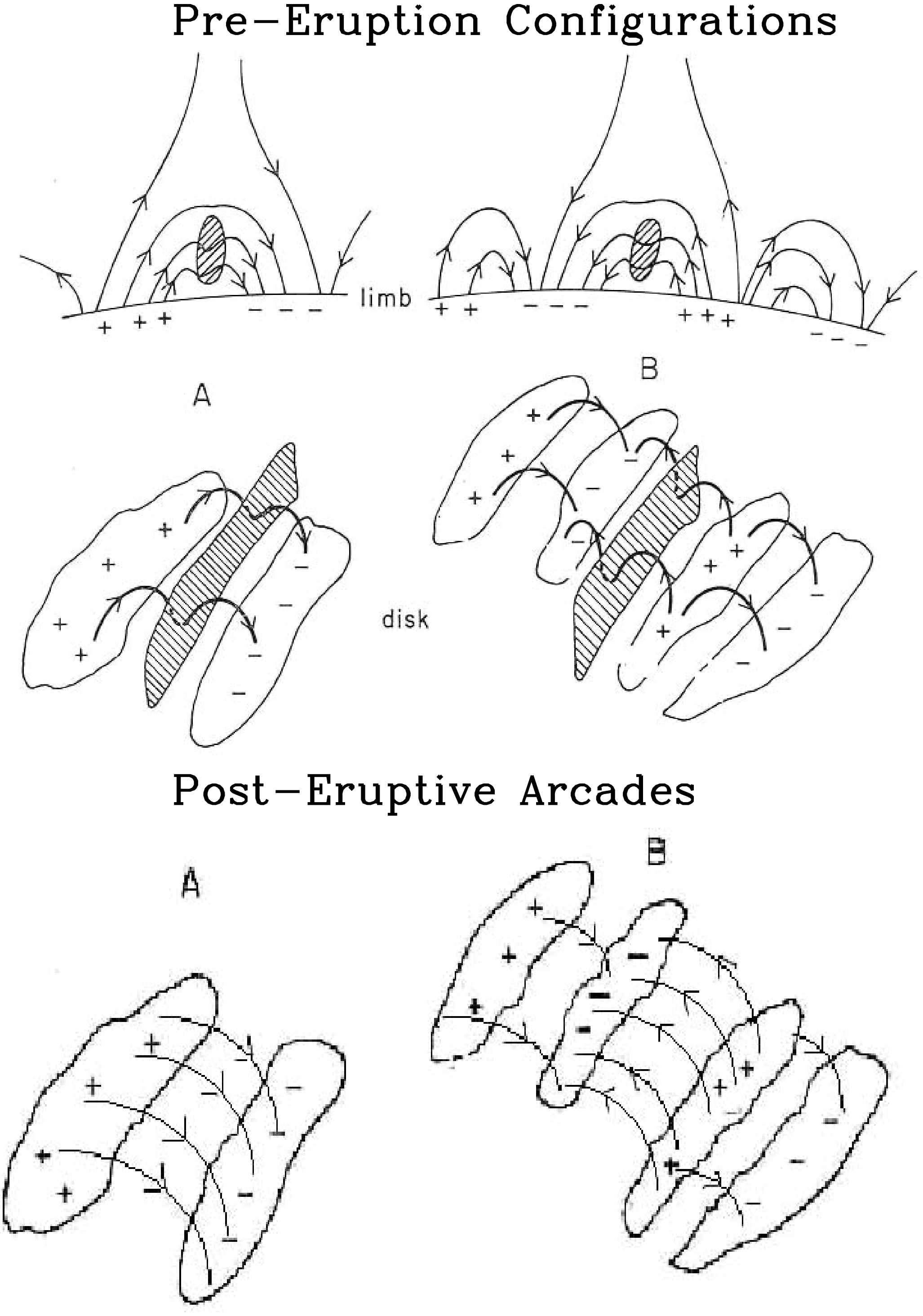
Pre–Eruption Configurations
limb
+ + +
– – –
+ +
– – –
+ + +
– – –
A
B
disk
Post–Eruptive Arcades
A
B

Figure 6.8: Sketch showing the possible pre- and post-eruption field configuration of PEAs forming along neutral lines/filament sites in single bipolar regions (A) and in between pairs of them (B). The pre-eruption configuration is adapted from Tandberg-Hanssen (1974) (From Tripathi et al. 2004).

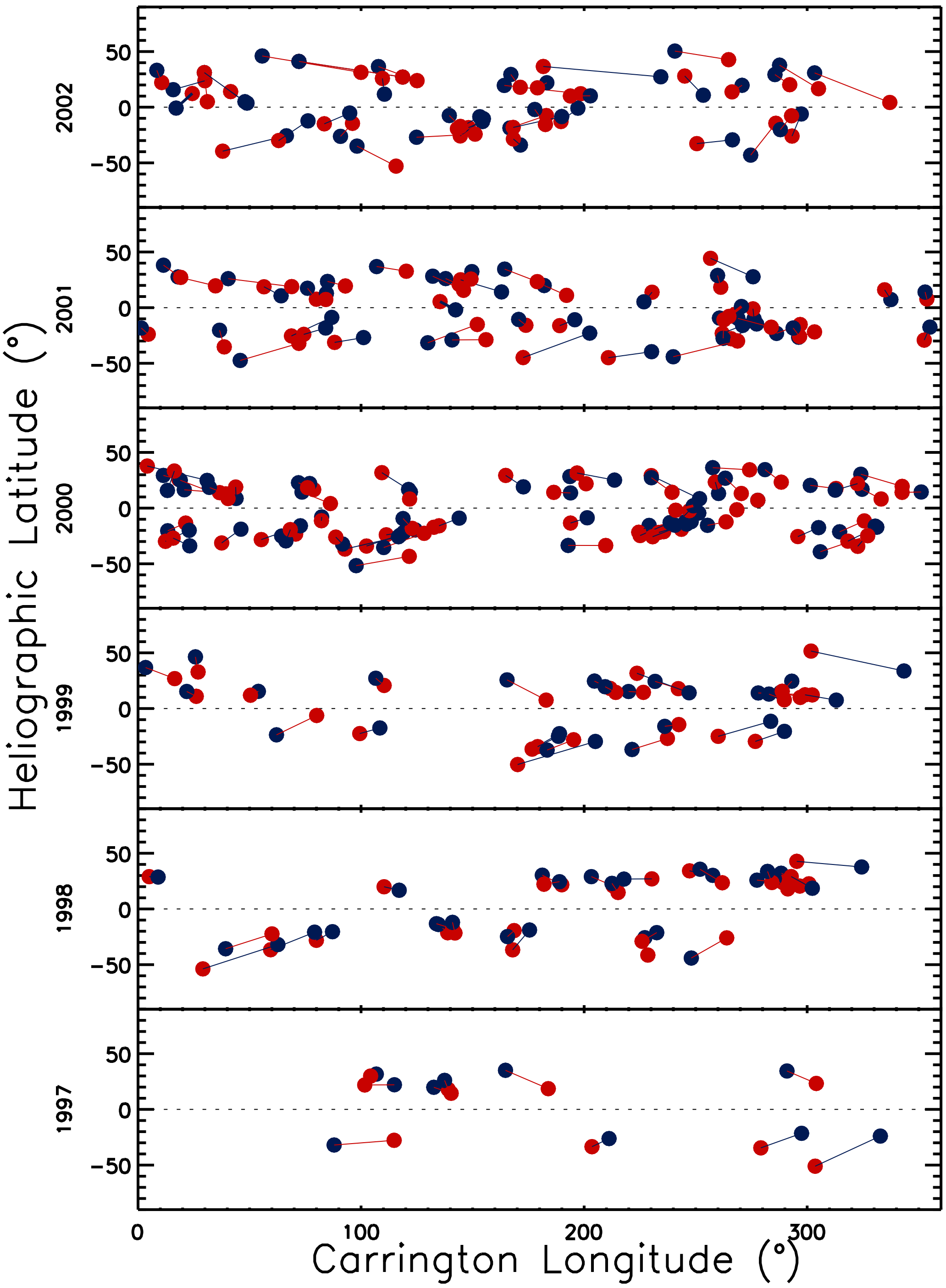

Figure 6.9: Carrington synoptic charts of the heliographic positions of post-eruptive arcades identified during 1997-2002 for which the magnetic polarities of the source regions were identified from MDI synoptic charts. The colors at the equatorward ends of the PEAs denote the magnetic polarity to the West of the individual polarity inversion lines, with the red color being assigned to the positive magnetic polarity and the blue color assigned to the negative one (From Tripathi et al. 2004).

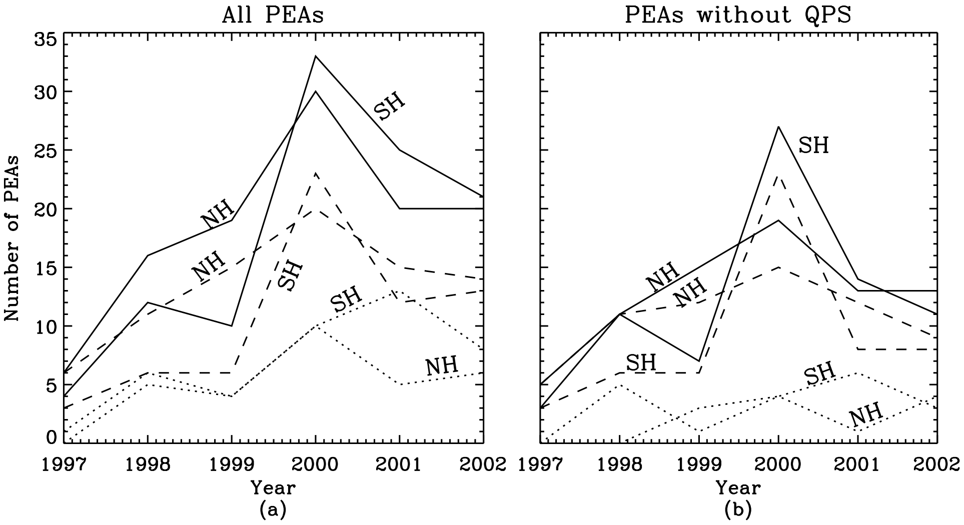

Figure 6.10: **a)** Total number of PEAs identified in the Sun's northern and southern hemispheres (solid lines) during 1997-2002 based on SoHO/EIT 195 Å observations displayed together with the number of events with positive and negative magnetic polarities (dashed lines) to the West of the neutral line in both hemispheres. The dotted lines represent the number of events with reversed polarities in both hemispheres. **b)** Same notation as in a), but with PEAs exhibiting quadrupolar-like (PEAs that formed in between pairs of BPRs) photospheric field source regions removed. Note that no events were recorded by EIT during the SoHO recovery phase in the second half of 1998 so that the frequency during this year appears under-represented (From Tripathi et al. 2004).

to maximum phase of cycle 23, from 1996 until 2000, seems not be obvious in the PEA frequency distribution.

In order to investigate the solar cycle variation of the PEAs heliographic locations, the variation of the midpoints of the PEA axes during 1997-2002 were investigated. Fig. 6.11 shows, that the PEAs locations follow, as expected, the butterfly pattern of sunspots. Similar to active regions, the PEAs move in latitude from shortly before solar minimum until sometime shortly after the following minimum from the higher latitudes towards the solar equator. Some PEA events at higher latitudes seem to coincide with periods when strong pulses of new magnetic flux caused a migration of the magnetic flux towards the Sun's poles in agreement with the findings of Benevolenskaya et al. (2002).

A linear polynomial fit yielded for the latitude variation of the PEA locations in the two hemispheres: b_N(deg) = 3713.26 - 1.85 t for the North and b_S(deg) = -5990.09 + 2.98 t for the South, with the time t given in years during 1997-2002. The source regions of the PEAs on average occurred at higher latitudes in the Sun's southern hemisphere compared to those in the northern hemisphere. The difference between 1997-2000 is about 15° in latitude. The stronger patchy pattern of evolving photospheric flux in BPRs in the Sun's southern hemisphere might have led to frequent appearance of reversed polarity PEAs.

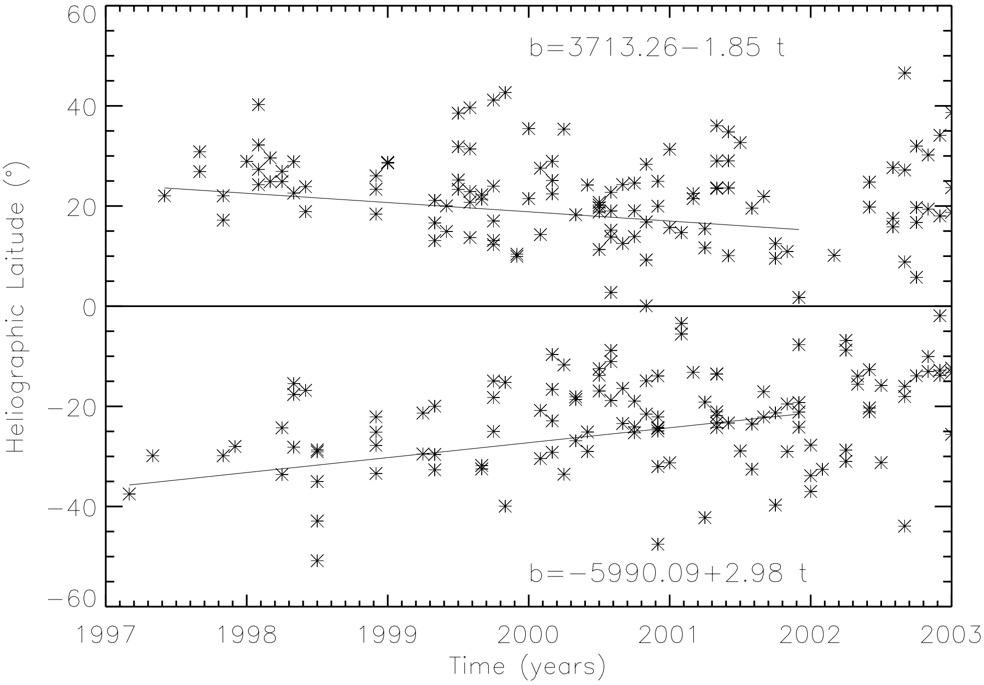

Figure 6.11: Variation of the heliographic latitude of post-eruptive arcades in solar cycle 23 from 1997 to 2002. The straight lines represent fits for the Sun's northern (positive latitudes) and southern (negative latitudes) hemisphere. Note that no events were detected above 60° latitude (From Tripathi et al. 2004).

6.4 Summary and conclusions

From a careful inspection of the full set of SoHO/EIT 195 Å observations taken during the period 1997-2002, a set comprising 236 post-eruptive arcade (PEA) events has been identified, with the requirement that each PEA was observable over its full spatial extent on the visible solar disk. The selected PEA events were correlated with their photospheric source regions as located in the SoHO/MDI magnetogram synoptic charts.

The derived basic characteristics of EUV PEAs over the years 1997-2002 can be summarized as follows:

1. EUV PEAs had 195 Å emission lifetimes in the range 2 to 20 hours, with an average lifetime of 7 ± 2 hours, i.e. PEAs still existed at times when the corresponding CME already reached distances of a couple of solar radii from the Sun, depending on the individual speed of propagation (see Chapter 7).

2. The length of the long axis, L, of a PEA varied in the range 2 to 40 degrees, with an average value of 15 ± 4 degrees.

3. The heliographic positions were found to match the locations of the active region belts in both hemispheres, with no events identified at latitudes higher than 60° N or S and with an extremely rare (<1%) number of transequatorial cases.

4. The orientations of the axes of the PEAs followed Joy's law, being commonly NE to SW oriented in the Sun's northern hemisphere and SE to NW in the southern hemisphere.

5. The lengths of the PEA axes increased with latitude by a factor of 3 to 4 in each hemisphere. The exact latitudinal variation during the period 1997 to 2002 was: L_N(deg) = 2.9 (b - 17.1) in the northern and L_S(deg)= - 1.6(b + 13.4) in the southern hemisphere respectively, with b being the heliographic latitude.

6. The PEAs spanned polarity inversion lines (PIL) separating regions of opposite magnetic polarities in the SoHO/MDI synoptic charts of the photospheric magnetic field. 149 (68%) out of 216 PEAS, for which MDI data were available, formed in individual bipolar regions (BPRs), the remaining ones originated from neighboring pairs of BPRs as QPS cases.

7. The dominant polarity found to the West of the PEA axes overlying the polarity inversion lines separating the opposite field polarities, was as expected predominantly positive (N) in the northern hemisphere and predominantly negative (S) in the southern hemisphere during 1997-2002. However, a significant number (31% out of 216 events) showed the reversed polarity being randomly distributed over the investigated time period.

8. The heliographic latitude variation of the PEA positions at the Sun followed the active region locations during 1997-2002, with b_N(deg) = 3713.26 - 1.85 t in the North and b_S(deg) = -5990.09 + 2.98 t in the South, where t is given in years from 1997 to 2002. During the analyzed time interval, PEAs in the southern hemisphere were found on average to be located about 15° further away from the solar equator compared to the position of PEAs in the northern hemisphere.

7 EUV PEAs and CMEs

The formation of large-scale magnetic loop systems, called post-eruptive arcades, has often been found to be some what associated with coronal mass ejections. In this chapter we present for the first time a long-term systematic study of the association of post-eruptive arcades identified in EIT 195 Å data set with white-light coronal mass ejections detected by the LASCO/C2 coronagraph.[†]

7.1 Introduction

The development of post-eruptive arcades (PEAs) sometimes following a sudden brightening in S- or reversed S-shaped structures, called sigmoid (see Chapter 2, section 2.3.4), has recently been observed in association with CMEs (Hudson et al. 1998). Canfield et al. (1999) showed that active regions associated with such sigmoidal patterns are more likely to erupt. The sigmoidal structures were thus considered as CME precursors.

The main goal of this chapter is to explore for the first time a detailed statistical relationship between the derived EUV PEA data set with white-light CMEs detected by the LASCO coronagraphs.

7.2 Association of PEAs with CMEs

The association of a PEA with a white-light CME was investigated for every identified PEA listed in the table of appendix A based on LASCO/C2 observations. Fig. 7.1 shows an example of a PEA located near the central meridian (CM) in the southern solar hemisphere and its associated white-light CME first detected in the FOV of C2 on 12-Sep-2000, at 12:30 UT. The detection of the CME in C2 was preceded by a filament eruption observed by EIT at around 11:48 UT, becoming visible in C2 at 12:54 UT. The estimated onset time of the CME was 11:45 UT according to the h-t diagram (see Fig. 7.2), which in this case is in good agreement with the onset time of the prominence eruption imaged by EIT. However, the validity of the estimated CME onset time based on the extrapolation of the h-t diagram can sometimes be misleading, e.g., for CMEs that were slowly accelerated in their initiation phase or in case of halo CMEs. The identified onset time of the corresponding PEA at

---

[†] The content of this chapter has been published in Astronomy and Astrophysics, V. 422, p. 337-349, 2004.

195 Å in the EIT images was 12:24 UT, showing its maximum development around 13:48 UT and disappearing at about 17:48 UT. The EUV PEA formed about 39 minutes after the eruption of the prominence and CME lift-off, and was still lasting when the CME had already reached a height of more than 40 $R_{\odot}$. The timing of the individual phenomena is summarized in Fig. 7.2.

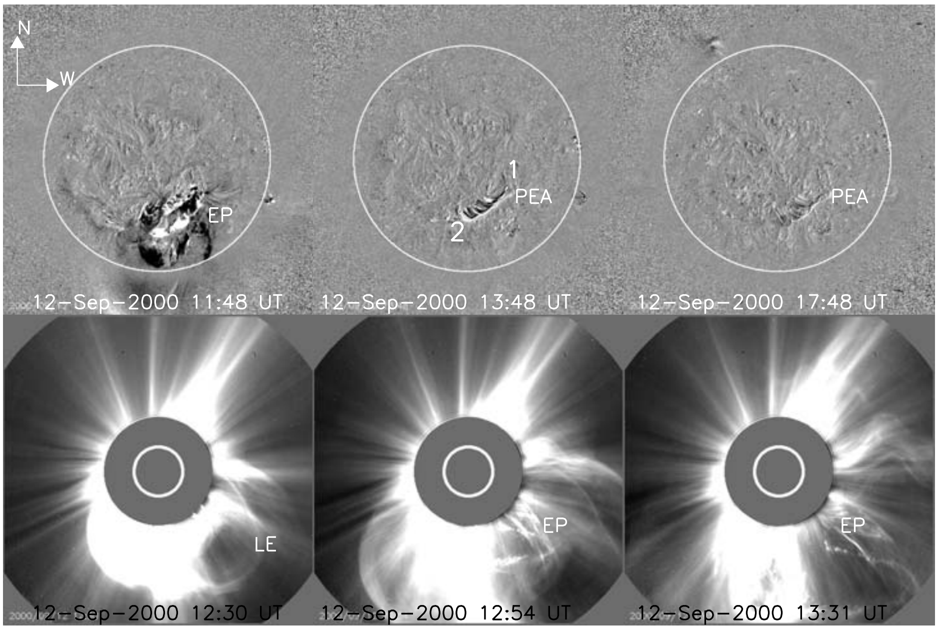

Figure 7.1: Top panel: Running difference images taken by EIT 195 Å on 12-Sep-2000. The first two images show the erupting prominence (EP) event and consequent post-eruptive arcade (PEA) formation in the southern hemisphere near CM. Points 1 and 2 represent the start and end points of the PEA. The last figure reveals the dimming of the arcade. Bottom panel: LASCO/C2 images showing the evolution of the associated CME in white-light. LE denotes the leading edge of the CME and EP the erupting prominence. In all figures, north is up and west is towards the right. The speed of the CME in the plane of the sky was 1550 km/s at PA 220 (From Tripathi et al. 2004).

A remarkable feature of Fig. 7.1 is the apparent similarity between the shape of the CME core and structure of the erupting prominence and PEA system. As can be inferred from the bottom panel of Fig. 7.1, the CME resembles a large-scale curved cylindrical flux tube that has originated from a source site bounded by the PEA's two extreme points which are likely to be considered as the two legs of the CME.

The systematic investigation of the association of the entire set of PEA events listed in appendix A, with white-light CMEs detected by LASCO in close spatial and temporal relationship, showed that 210 (92%) out of 236 events identified from 1997 until the end of 2002 had clear CME associations. In seven out of 26 events there were no LASCO data taken, so that only 19 PEAs were found to be lacking an associated CME.

Figure 7.3 shows the distribution of all identified PEAs in heliographic longitude presented in bins of ten degrees. As expected, the distribution peaks near CM, where PEA events can best be observed over their full extent. The few PEAs without associated LASCO/C2 CMEs were all observed around disk center in the

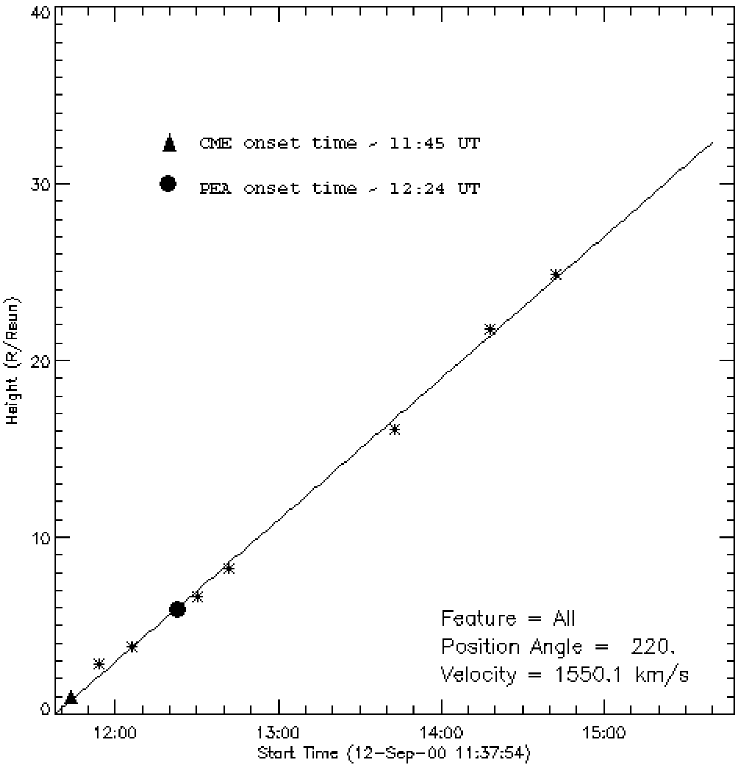

Figure 7.2: LASCO C2/C3 h-t diagram for the CME detected on 12-Sep-2000, around 12:30 UT. The solid triangle marks the estimated CME onset time at 1 solar radii and the solid circle represents the identified onset time of the PEA based on EIT 195 Å images. The h-t diagram was taken from the CME catalogue at http://cdaw.gsfc.nasa.gov/CME_list/ (From Tripathi et al. 2004).

range 40° East to 30° West.

Taking into account, that front-side halo CMEs originating from near disk center are often hard to detect because of the dependence of the efficiency of Thomson scattered light on the viewing angle of the CME with respect to the line of sight (e.g., Plunkett et al. 1998; Brueckner et al. 1998), it seems reasonable to assume that the small number of PEAs without CME association may have been caused by sensitivity limitations of LASCO. Hence it thus seems plausible to assume that PEAs are definite indicators of CMEs that originated from the corresponding regions of the visible disk.

7.3 Comparison with Ground-Based Hα Data

Disappearing filaments (prominence eruptions) are considered as one of the best signatures of CMEs (e.g., Bothmer & Schwenn 1994; Gopalswamy et al. 2003). As an example for this connection, Fig. 7.4 shows that the front-side halo CME on 17-Feb-2000, that originated from the SE (south-eastern) part of the Sun near CM, was accompanied by a disappearing filament in Hα (Fig. 7.4, middle and right images in top panel).

A PEA event associated with a disappearing filament, but without corresponding

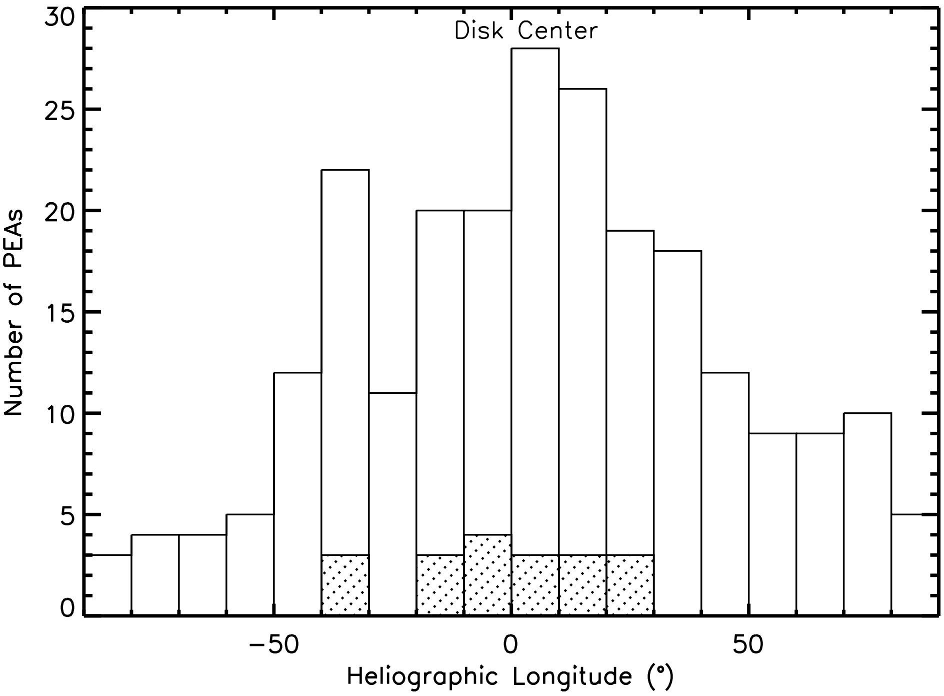

Figure 7.3: Distribution of PEAs in heliographic longitude in bins of 10 degrees as identified in EIT 195 Å images from 1997 to 2002. The portions of the bars represented as spotted areas represent those PEAs for which no white-light CME had been detected by LASCO/C2 (From Tripathi et al. 2004).

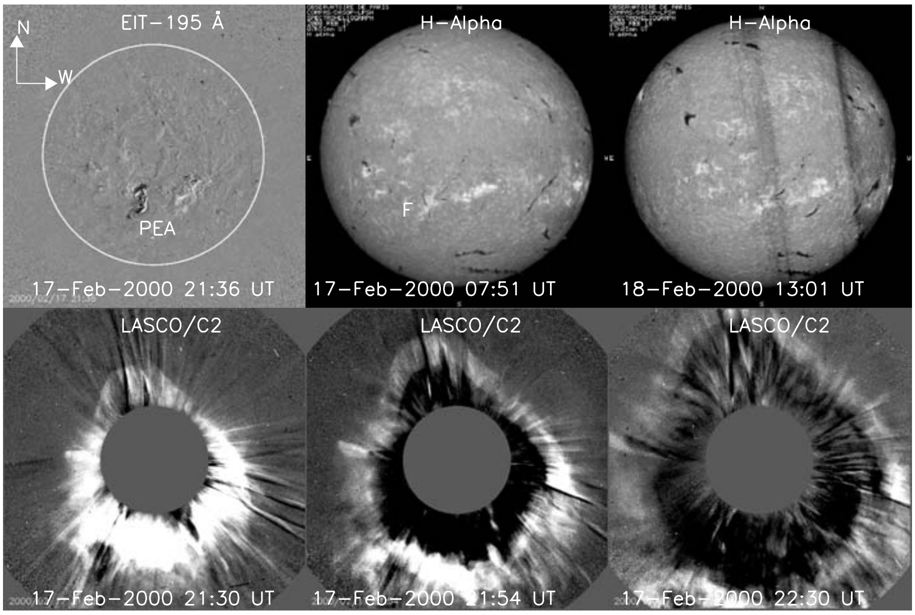
EIT-195 Å
N
W
PEA
17-Feb-2000 21:36 UT
H-Alpha
F
17-Feb-2000 07:51 UT
H-Alpha
18-Feb-2000 13:01 UT
LASCO/C2
17-Feb-2000 21:30 UT
LASCO/C2
17-Feb-2000 21:54 UT
LASCO/C2
17-Feb-2000 22:30 UT

Figure 7.4: Top panel: The first image shows a running difference image taken by EIT at 195 Å on 17-Feb-2000 displaying the PEA that had formed in the southern hemisphere. The second and third images show that a filament (F) disappeared from this solar region based on Hα observations taken on 17 & 18-Feb-2000 (courtesy Paris/Meudon Observatory). Bottom panel: The associated halo CME on 17-Feb-2000 as detected by LASCO/C2 around 21:30 UT. The speed of the CME was 600 km/s at PA 196 (From Tripathi et al. 2004).

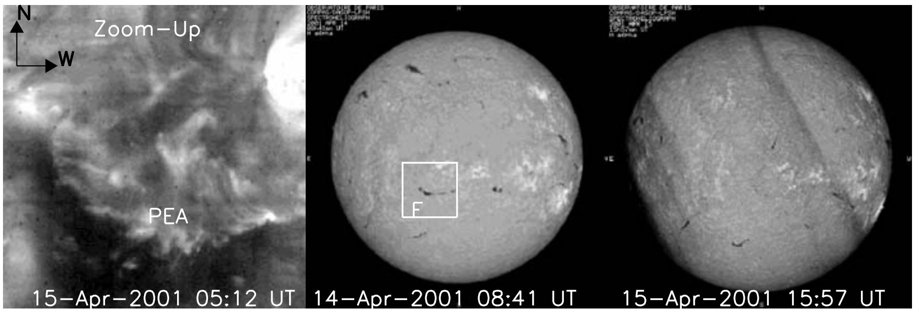

Figure 7.5: Left to right: Zoomed view of the post-eruptive arcade (PEA) observed by EIT at 195 Å on 15-Apr-2001 at 05:12 UT followed by two Hα images taken on 14 and 15 April showing the position of the corresponding disappearing filament (F) on the solar disk (From Tripathi et al. 2004).

LASCO white-light CME is shown in Fig. 7.5. For better visibility, only a portion of the full disk EIT image, comprising the full spatial extent of the PEA is displayed. The Hα and EIT features are basically the same as observed for the event on 17-Feb-2000, visualized in Fig. 7.4 except that a CME was not identified in the LASCO data.

If one considers Hα filament eruptions as valid CME proxies, 14 more events out of the 19 cases where no white-light CME was detected, can be clearly considered as CME-associated. Unfortunately, in 3 cases no Hα data were available and in 2 cases the events were very complex so that the interpretation of the data was difficult. If one takes into account these informations, the total number of PEAs associated with CME increases to 98% (224 out of 229 events) i.e., almost a one-to-one correspondence between EUV PEAs and CMEs. But the correlation is only uni-directional i.e., every EUV PEA seem to have an associated CME, however this result does not imply that each CME is followed by a PEA.

7.4 Multi-Wavelength Investigation of PEAs

Table 7.1: The columns from left to right are: Date of observation; start-, end of rising- and peak-time of GOES X-ray flares; flare locations on the solar disk in heliographic coordinates; times of coronal brightenings observed by Yohkoh/SXT, onset times of PEAs observed by SoHO/EIT at 195 Å; estimated onset times of the associated CMEs based on the investigation of h-t diagrams.

Date	*GOES X − Ray (UT)*	*Flare Location* (deg)	*Flare Class*	*CB* *(UT)*	*PEA Onset (UT)*	*CME Onset (UT)*
9-Feb-00	19:10-19:18;19:40;20:00	S17 W40	C74	(19:43)	20:12	19:26
17-Feb-00	20:10-20:15;20:30;20:32	S29 E07	M13	(20:23)	20:36	20:19
2-Jun-00	08:50-09:00;09:30;09:36	N10 E23	C24	(09:22)	09:36	09:12
6-Jul-00	12:15-12:20;12:35;12:36	N18 E25	C43	(13:15)	13:25	12:30

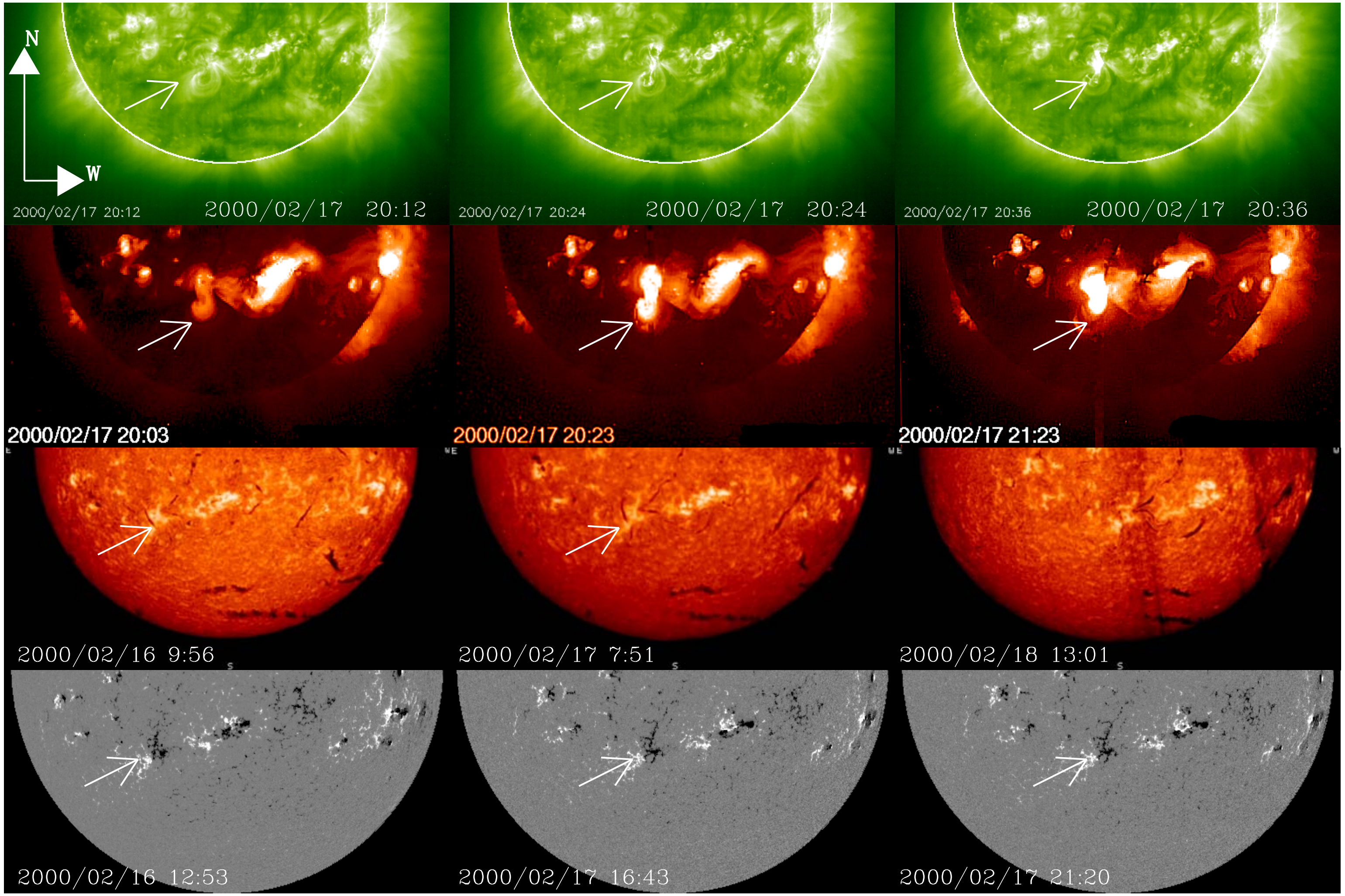
N
W
2000/02/17 20:12
2000/02/17 20:12
2000/02/17 20:24
2000/02/17 20:24
2000/02/17 20:36
2000/02/17 20:36
2000/02/17 20:03
2000/02/17 20:23
2000/02/17 21:23
2000/02/16 9:56
2000/02/17 7:51
2000/02/18 13:01
2000/02/16 12:53
2000/02/17 16:43
2000/02/17 21:20

Figure 7.6: Multi-wavelengths observations of the source region of the 17-Feb-2000 PEA event around 21:30 UT. Top to bottom: First panel: EIT 195 Å images taken at 20:12 UT, 20:24 UT and 20:36 UT on 17-Feb-2000 showing the pre-eruption configuration of the halo CME detected later by LASCO and the initial phase of the arcade formation. Second panel: Yohkoh/SXT images taken at 20:03 UT, 20:23 UT and 21:23 UT on the same day showing the brightening of an S-shaped sigmoid in the S-hemisphere in the CME source region. Third panel: Hα observations taken on 16, 17 and 18-Feb-2000 showing that a filament had disappeared from the corresponding source region. Fourth panel: MDI magnetograms taken at 12:53 UT on February 16, 16:43 UT and 21:20 UT on 17-Feb-2000, showing the photospheric magnetic field structure of the CME's source region (From Tripathi et al. 2004).

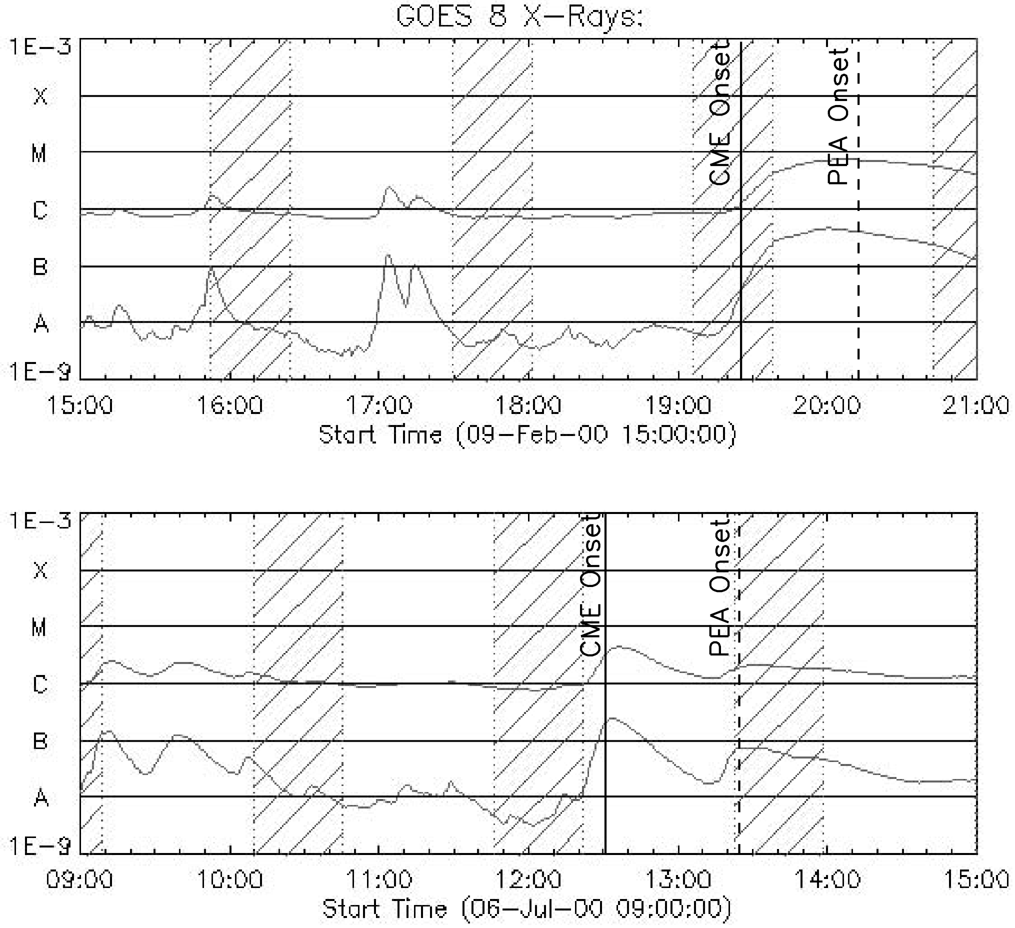

Figure 7.7: GOES 8 X-ray plots for the CME and PEA events on 09-Feb-2000 (top) and 6-Jul-2000 (bottom). The approximate onset times of the CMEs and PEAs are labeled (From Tripathi et al. (2004).

Fig. 7.6 shows a multi-wavelength view of the CME's source region based on SoHO/EIT and MDI, Yohkoh/SXT, and ground-based Hα observations from Paris/ Meudon. The filament closely followed the orientation of the neutral line which separates regions of opposite magnetic polarity as inferred from the SoHO/MDI data. Bright loops in form of an S-shaped sigmoid, prominent in the Sun's southern hemisphere, are often visible shortly before the eruption of a CME (e.g., Canfield et al. 1999), visible here at around 20:00 UT on February 17 (Fig. 7.6, second panel from top, first image). A strong brightening of the sigmoidal system occurred near the CME's lift-off time at around 20:23 UT (see Yohkoh/SXT images in Fig. 7.6), followed by the onset of the EUV arcade around 21:36 UT. The X-ray flare observed by GOES 8 started between 20:10 and 20:15 UT (see Table 7.1), increasing in intensity and reaching its peak value near 20:32 UT. The onset of the PEA seen by EIT follows in time the peak of the X-ray flare. The CME onset time corresponds to the rising phase of the X-ray flare, coinciding with its acceleration phase, in agreement with the findings of Zhang et al. (2001). Assuming that the peak intensity of the flare indicates the CME's lift-off from the Sun, the PEA may be interpreted as a consequence of magnetic reconnection processes that were initiated underneath the

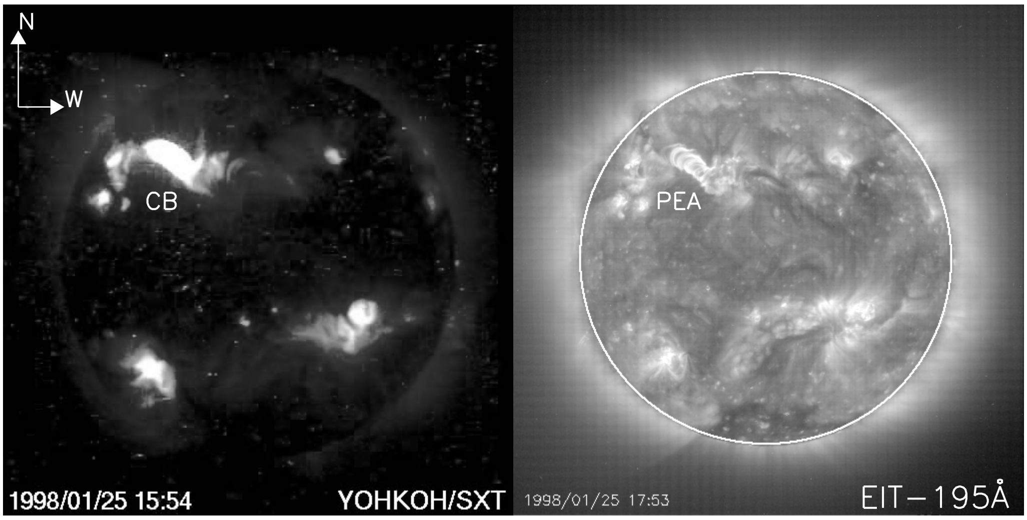

Figure 7.8: YOHKOH/SXT image taken on 25-Jan-1998 at 15:54 UT showing the coronal brightening (CB) that was detected on the NE part of the solar disk and the corresponding post- eruptive arcade (PEA) observed by EIT at 195 Å at 17:53 UT (From Tripathi et al. 2004).

rising CME as suggested by Kopp & Pneuman (1976).

For three more PEA events, the flare position, as provided by the GOES catalogue was located not further away from the PEA location than ± 5° in heliographic latitude and longitude. These were observed within a time interval of three hours prior to the onset of the PEA. The chronological evolution of the coronal features seen by EIT 195 Å and SXT were compared with the GOES 8 X-ray flare timings (see Table 7.1). The time evolution in the events is similar: A rising phase in soft X-ray intensity during the acceleration phase of the CME, its consequent lift-off and propagation phase, followed some minutes later by the peak in X-ray intensity, finally followed by the formation of the PEA underneath it. Fig. 7.7 shows the time evolutions of the GOES 8 X-ray flares for the PEA and CME events observed on 09-Feb-2000 and 06-Jul-2000. Whereas on 06-Jul-2000, the PEA caused a second increase of the X-ray intensities, it can not be distinguished as a separate feature in the GOES 8 X-rays on 17-Feb-2000. The coronal brightenings observed by SXT preceded the onset of the EUV PEAs by about 5 to 30 minutes (see Table 7.1), but due to the irregular cadence of the SXT observations, no detailed statistics could be performed. Fig. 7.8 shows an example of a transient coronal brightening detected by SXT on 25-Jan-1998 and PEAs seen by EIT.

7.5 Summary and Conclusions

The main goal of this chapter was to identify the relationship between EUV PEAs and white-light CMEs. The images taken by EIT at 195 Å and LASCO/C2 were used for this analysis. Further in some cases ground-based Hα observations, images by Yohkoh/SXT and data from the X-ray flare catalogue provided by GOES-8 satellite were used as complementary data. The systematic comparison of EUV and white-light observations yielded the following results:

1. A near one-to-one (uni-directional) correspondence between PEAs observed by SoHO/EIT at 195 Å and white-light CMEs detected by SoHO/LASCO was found for the identified events. PEAs can thus be considered as reliable disk tracers of CMEs, i.e. EUV images taken at 195 Å can provide information on CME events even without the availability of simultaneous coronagraph observations.
2. A systematic study of the chronological evolution of the EUV and X-ray signatures in four events shows, based on SoHO, Yohkoh and GOES 8 measurements, that the rising phases of the X-ray flares coincided with the acceleration and lift-off phases of the corresponding CMEs, followed by the peaks in flare intensities and subsequent coronal brightenings visible in soft X-rays and at EUV wavelengths. PEAs thus represent a coronal signature for the aftermath of a CME in the course of its magnetic restructuring.

8 Plasma Downflows above PEAs after CME Eruptions

In this chapter we study the dynamics of a CME event detected by LASCO/C2 coronagraph on 05-Mar-2000 associated with a prominence eruption and EUV post-eruptive arcade. The most interesting phenomenon associated with this particular CME event was the detection of sunward-moving plasma (downflow) above the post-eruptive arcade after the CME lift-off. An attempt will be made to provide explanations for the observed downflow. [†]

8.1 Introduction

Observations of downflows above large-scale post-flare arcades (supra-arcades) were first reported by McKenzie & Hudson (1999) on the basis of soft X-ray observations. These downflows manifest themselves as dark structures moving through the corona towards the Sun with speeds in the range 45-500 km/s. All events with sunward plasma motions were associated with coronal mass ejections (CMEs). One very simple explanations of these downflows could be that some portion of the CME material fails to achieve the escape velocity and consequently falls back towards the Sun under the force of the Sun's gravitational field. In that case the downflowing hot material eventually cools down and becomes visible in lines such as Hα. Material falling back due to the Sun's gravitational field is termed as "coronal rain", originally based on Hα observations (Tandberg-Hanssen 1974, p. 29). The physical explanation generally given for coronal rain is that the plasma which was evaporated into the tops of flaring loops (Forbes & Malherbe 1986; Svestka 1998) radiates away its energy and cools down. Since no cooler counter-part was detected in Hα and at EUV wavelengths for the downflows observed in SXRs (Soft X-rays), McKenzie & Hudson (1999) and McKenzie (2000) interpreted these downflows as plasma voids with low densities and high temperatures. These "voids" were thought to be the direct observational evidence for magnetic reconnection processes which had occured higher up in the corona.

White-light features moving towards the Sun's surface after CME lift-off have first been detected by Wang et al. (1999) and Sheeley & Wang (2002) based on LASCO/C2 observations. These coronal inflows occured at altitudes of 3-5 $R_\odot$ with speeds in the range of 50-200 km/s. The inward moving features in white-light were observed as dark trails behind barely visible density enhancements with a cusp like appearence. These features were interpreted as observational signatures of the closing down of magnetic field lines which were dragged outward by CMEs, providing plausible evidence for the occurrence of magnetic reconnection processes.

[†] The content of this chapter is to be submitted in Astronomy and Astrophysics, 2005

Recently, Innes et al. (2003a, 2003b) reported similar features detected in EUV by the Transition Region And Coronal Explorer (TRACE; Handy et al. 1999) and SoHO/Solar Ultraviolet Measurements of Emitted Radiation (SUMER; Wilhelm et al. 1995). Here the inflow was observed as a dark trail of plasma moving towards the Sun at 195 Å in TRACE and in the Fe-XXI & UV continuum by SUMER. These inflows were not seen in C-II and Fe-XII lines. Based on these observations, Innes et al. concluded that the dark trails of the plasma are likely the plasma voids introduced by McKenzie & Hudson (1999). Using complementary observations from TRACE and RHESSI, Asai et al. (2004) identified a time correlation between non-thermal radiation in the hard X-ray spectra taken by RHESSI and the times of downflows observed by TRACE at 195 Å. Based on these observations Asai et al. (2004) concluded that the downflow motions occurred when large amounts of magnetic energy was released, suggesting a relation of downflows with reconnection outflows.

In this chapter we present an observation of a distinct downflow observed by SoHO/EIT at 195 Å on 05-Mar-2000. The downflow was observed above post-eruptive arcades (PEAs) ∼90 minutes after the eruption. The formation of a post-eruptive arcade observed on the disk was probably related to shrinking magnetic field lines as a consequence of magnetic reconnection after the CME eruption (Kopp & Pneuman 1976). The data set clearly showed material flowing downward at heights below 0.5 $R_\odot$ above the solar surface. Contrary to the earlier observations of dark downflows by SXT, TRACE and LASCO, the downflow observed in this event at 195 Å was bright.

8.2 Observations

The eruption of two large prominences marked with P1 & P2 in Fig. 8.1, and a barely discernable prominence marked with P3 was recorded 05-Mar-2000 by EIT at 195 Å. The sequence of the running difference images in Fig. 8.1 shows the almost simultaneous eruption of P1, P2 and P3. The running difference images reveal the proper motion of the features in the direction of motion (Sheeley et al. 1999). The formation of a PEA starts at approximately 16:12 UT underneath P1. The PEAs evolve in height with time as can be seen in Fig. 8.1 and also in Fig. 8.3.

The associated CME was first seen at 16:54 UT in the LASCO/C2 field-of-view (FOV), (see Fig. 8.2). The CME later, after 17:06 UT, exhibited the typical three part structure being comprised of a bright front, a dark cavity and a bright core. Possible individual CMEs associated with prominence eruptions P1, P2 and P3 cannot be uniquely distinguished in the coronagraphic images. The prominence P1 and P2 was later seen as core of the CME at 17:06 UT. The prominences P1 and P2 are clearly discernable until 17:54 UT in LASCO/C2 observations marked by arrows

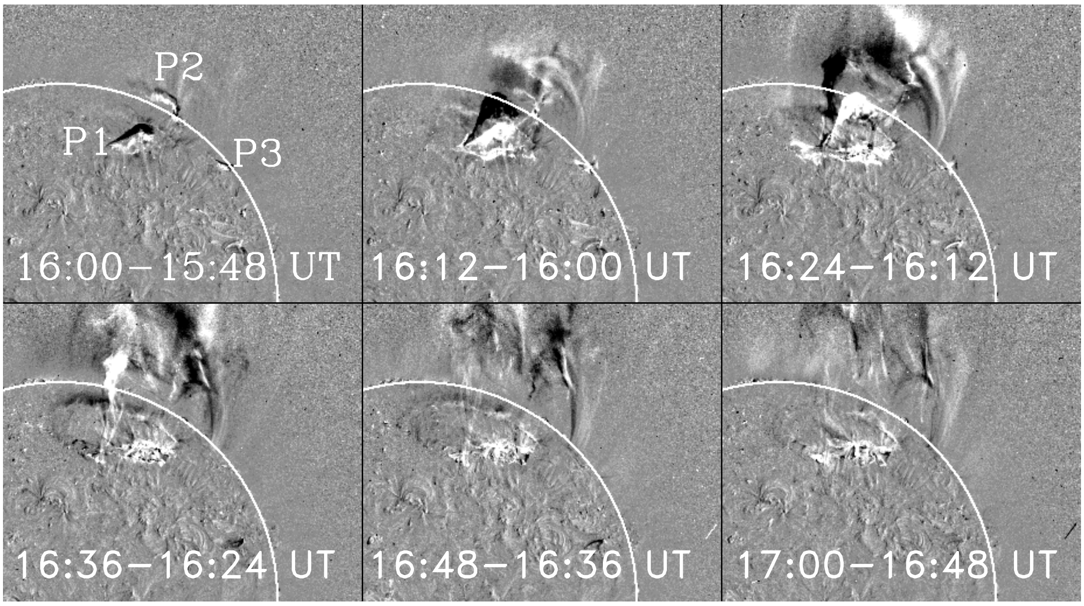
P2
P1
P3
16:00−15:48 UT
16:12−16:00 UT
16:24−16:12 UT
16:36−16:24 UT
16:48−16:36 UT
17:00−16:48 UT

Figure 8.1: Sequence of running difference images taken by SoHO's Extreme-ultraviolet Imaging Telescope (EIT) at 195 Å on 05-Mar-2000. The images show the simultaneous eruption of three prominences marked as P1, P2 & P3. In the images North is pointing upwards and West towards the right.

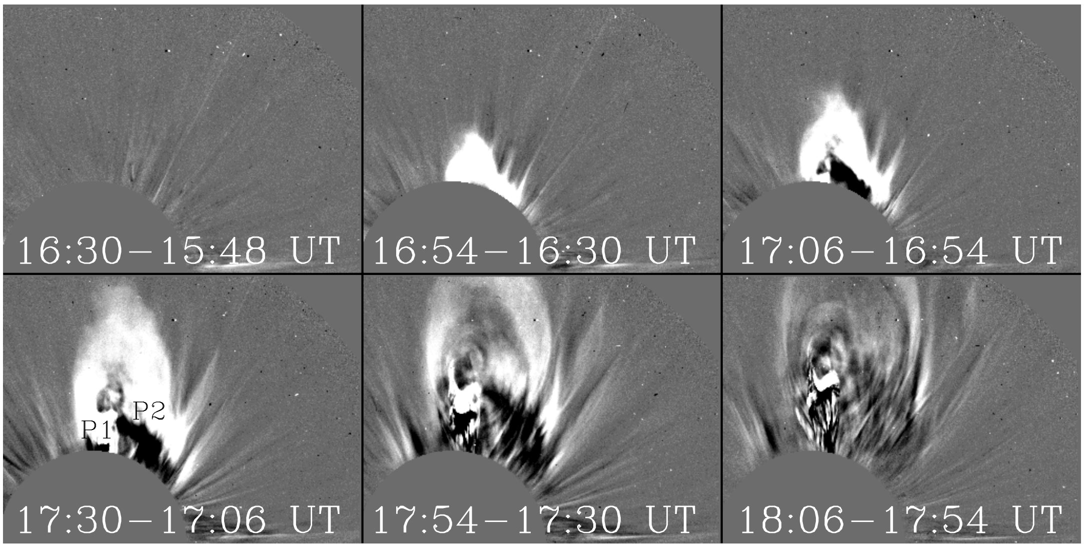
16:30−15:48 UT
16:54−16:30 UT
17:06−16:54 UT
P2
P1
17:30−17:06 UT
17:54−17:30 UT
18:06−17:54 UT

Figure 8.2: Series of running difference images showing the evolution of a white-light CME detected by the LASCO/C2 coronagraph on 05-Mar-2000. The CME followed the prominence eruptions shown in Fig 8.1. The first appearence of the CME in the LASCO FOV is shown in the upper middle image. In later images the leading edge, dark cavity and bright core of a typical three-part CME can be seen. P1 & P2 mark the prominence material.

in the bottom left panel of Fig. 8.2. Later on at 18:06 UT, only P1 can be uniquely distinguished.

At 17:36 UT, i.e., ~90 minutes after the onset of the eruption, a bright sunward moving feature, hereinafter referred to as the downflow, was detected by EIT at 195 Å. Fig. 8.3 displays the running difference images taken by EIT at 195 Å starting

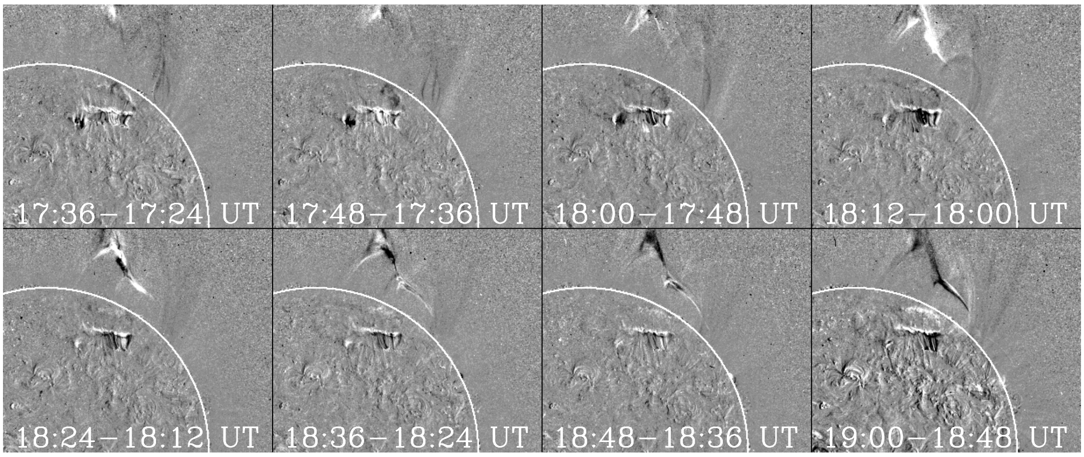

Figure 8.3: Series of running difference images taken by EIT at 195 Å showing the morphology of the sunward moving material (inflow) on 05-Mar-2000.

from the first detection (top left corner image) of the downflow until the time it vanished (bottom right corner image). The downflow is visible as the bright dot at the top edge of the top left image in Fig. 8.3. With passing time the bright structure extended downward, branching into two streams during the process. At least the right branch did not follow a straight or even regularly curved path, but showed a kink, clearly seen in the difference images at 18:24 UT. Since coronal plasma cannot cross magnetic field lines, it is either following a kinked field line or bright downward moving plasma is outlining the loops that the plasma is sliding down along. According to Fig. 8.3 the left branch of the downflow seemed to be linked to the eastern foot-point of P1 whereas the right branch seemed to be headed towards P3. Since we have no Doppler shift measurements we cannot rule out that we are only observing a brightening front moving downward, without any associated material flow.

The images taken by EIT and LASCO were further processed in order to enhance the contrast of fine-scale features by applying a wavelet decomposition technique established by Stenborg and Cobelli (2003) which is based on the work of Fligge & Solanki (1997). This technique involve multiple application of the wavelet transform and corresponds to a wavelet packet analysis, which leads to a better separation between signal and noise, thus allowing structure with finer details to be processed. The algorithm used in the processing of the images was the 2D-á trous transform. Most of the noise in the image is concentrated in the high frequency scale in the wavelet plane. A weighted reconstruction scheme is employed in which during the process of reconstruction considerably less weight can be given to the scale containing noise. More details about the algorithm can be found in Stenborg & Cobelli (2003).

The left panel of Fig. 8.4 displays the stack plot of the strips of the solar corona cropped from the wavelet processed EIT images. The figure was produced by cutting an arch-shaped strip of the solar corona above the limb (see Fig. 8.4, right panel) for the position angle (PA) between 290° and 360°. The PA was measured starting from the north pole in counter-clockwise direction as illustrated in the right panel of Fig. 8.4. A bi-linear interpolation was performed in order to transform the arch-

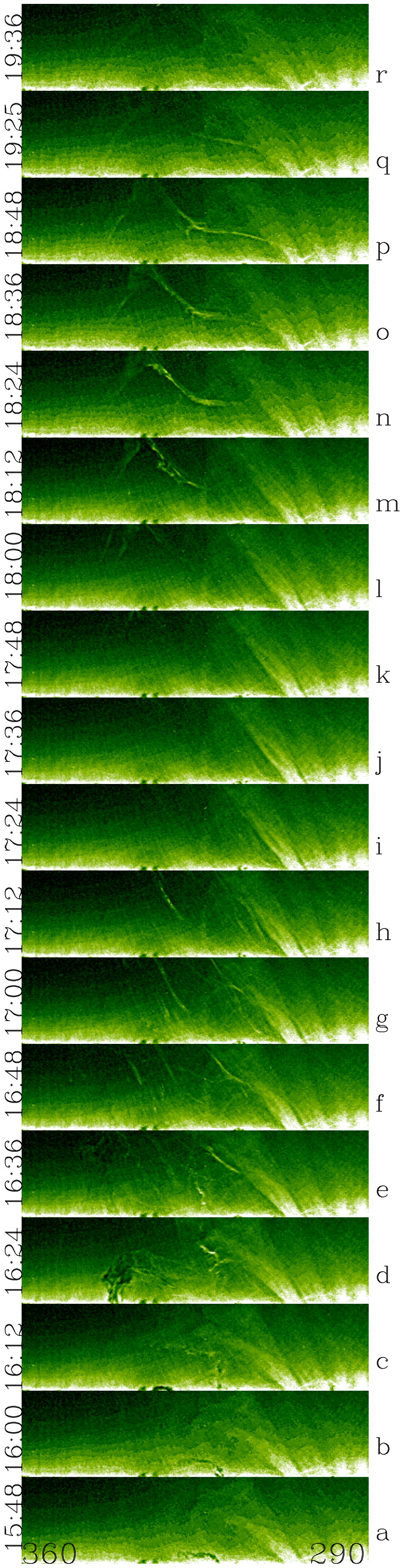
19:36
r
19:25
q
18:48
p
18:36
o
18:24
n
18:12
m
18:00
l
17:48
k
17:36
j
17:24
i
17:12
h
17:00
g
16:48
f
16:36
e
16:24
d
16:12
c
16:00
b
15:48
a
360
290

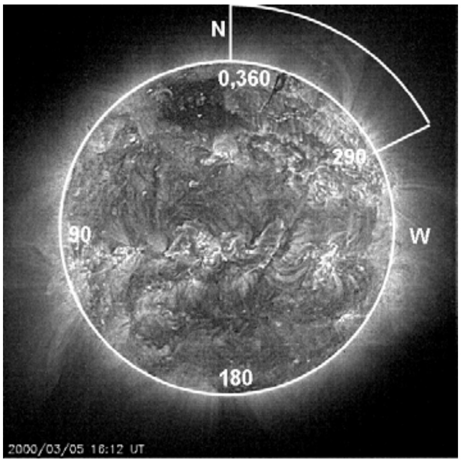
N
0,360
290
90
W
180
2000/03/05 16:12 UT

Figure 8.4: Left panel: Stack plot of cropped strips of the solar corona above the limb in EIT images. Time is running from bottom to top. The frames start at 15:48 UT ('a') and finishes at 19:36 UT ('r'). Each frame corresponds to the arch shaped strip marked in the right panel. The right corner denotes the position angle 290° and the left denotes 360°. Right panel: Wavelet processed EIT image taken on 05-Mar-2000 at 16:12 UT. The area marked with the arch-shaped strip is shown in the left panel. The convention for measuring position angle is marked.

shaped images into a rectangular shape. The eruption that started at ∼15:48 UT is best visible at 16:24 UT (see 'd') when a prominence is in the center of the FOV. By 17:24 UT ('i') the entire material had passed out of the EIT FOV. No visible plasma-motion associated with the erupted features are seen in images 'i' to 'k', although careful inspection of frame 'k' reveals a faint brightening at the top edge which is the first sign of the downflowing material. At 18:00 UT ('l') and very clearly at 18:12 UT ('m') plasma moving towards the Sun's surface was detected. The path of the downflowing plasma suggests that it was channeled by the magnetic field configuration of the corona (see images from 'm' to 'q'). Interestingly, in frames 'g' & 'h' a bright filamentary structure is seen at a similar location as one branch of the downflowing material approximately an hour later.

There was no clear evidence for a downflow of plasma in white-light images taken by LASCO/C2. In order to verify this, we produced height-time diagrams using running difference images taken by EIT at 195 Å and LASCO/C2 at a specified position angle (PA). Fig. 8.5 shows the height-time (hereafter h-t) diagrams for LASCO/C2 (upper panel, PA=347°) and EIT (lower panel, PA=345°). The h-t diagram were produced by cropping a thin strip at the specified position angle, starting above the limb at 1.02 $R_\odot$ in the case of EIT and starting above the occulter at $2_\odot$ in the case of LASCO/C2. The strips extended to 1.36 $R_\odot$ for EIT and to $6.0R_\odot$ for LASCO/C2. In the lower panel (h-t diagrams for EIT) of Fig. 8.5, both the outflow as well as the inflow were detected. They are marked by arrows. Whereas the inflow can be easily recognized by the fact that the bright structure moves down as time progresses, the outflow is so rapid that it appears as a vertical streak. The EIT height-time diagram allows us to measure the speed of the inflow by following the trajectory along the boundary of the moving dark and bright features. The inflow speed obtained at the position angle of 345° was 25 km/s. The bottom panel of Fig. 8.5 reveals that the downflow started at the height of $1.36R_\odot$, i.e., at the edge of the FOV and was seen until the height of $1.24R_\odot$ at this particular position angle. In the upper panel of Fig. 8.5 (h-t diagram for LASCO/C2) plasma outflow only could be definitely identified. A specific white-light feature in the h-t diagram of LASCO/C2, whose behavior could not be uniquely interpreted, is marked by the question mark in the upper panel. It may conceivably be the start of a downflow, but the backward extrapolation of the trajectory of the downflow seen in EIT does not match with this feature in time. Also, no outward motion of this feature in the h-t diagram was seen in LASCO/C2. Because of the lack of the observation from 1.35 to 2.0 $R_\odot$, it becomes difficult to make any substantial conclusion about the feature marked with the question mark.

8.3 Evolution of Prominence, CME and Downflow

The wavelet sharpening of EIT and LASCO/C2 & C3 coronagraphic images provided an opportunity to track the same feature in the FOV of different instruments. Fig. 8.6 shows the EIT 195 Å (top panel) image taken at 16:12 UT, LASCO/C2 (middle panel) and LASCO/C3 (bottom panel) images taken in white-light at 17:06

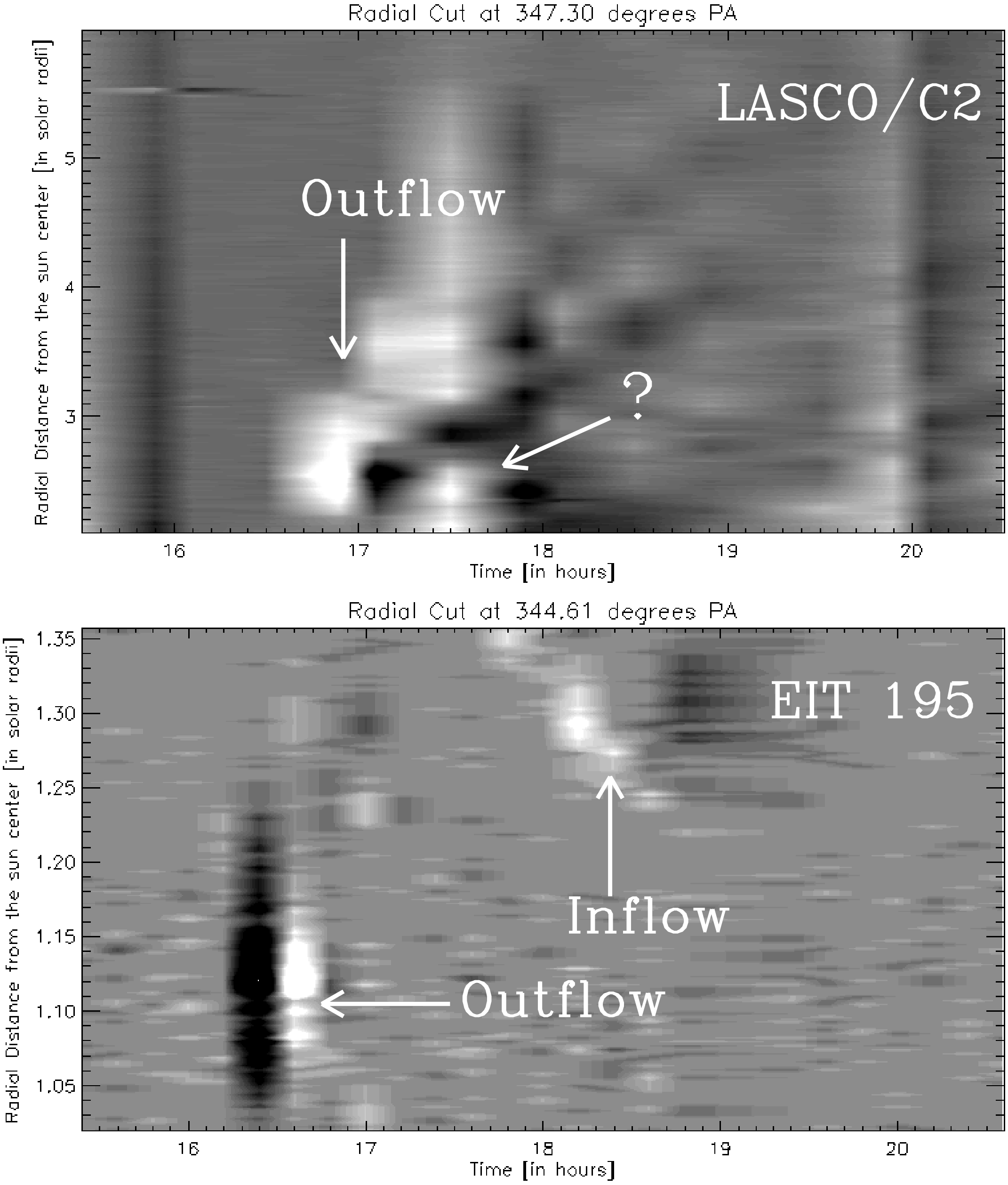

Figure 8.5: Top panel: Height-time diagram for LASCO/C2 running difference images at position angle 347° from 15:00-20:30 UT. Bottom panel: Height-time diagram for EIT 195 Å running difference images at position angle 345°. Note that the position angles are measured starting from solar north in counter clock wise direction as shown in Fig. 8.4. Outflows and inflows of the coronal material are labeled.

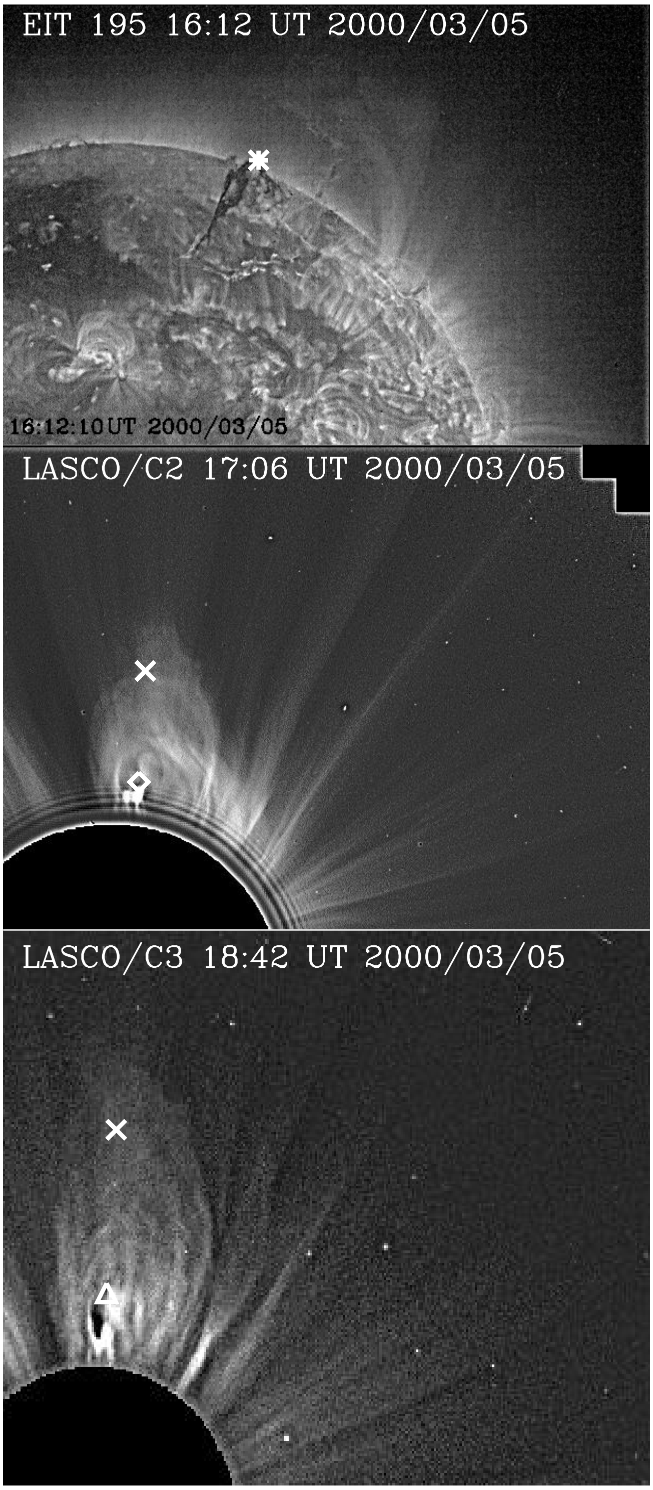
EIT 195 16:12 UT 2000/03/05
16:12:10UT 2000/03/05
LASCO/C2 17:06 UT 2000/03/05
LASCO/C3 18:42 UT 2000/03/05

Figure 8.6: Wavelet processed images taken by EIT (top panel, 16:12 UT), LASCO/C2 (middle panel, 17:06 UT) & C3 (bottom panel, 18:42 UT). The asterisk in the top panel, diamond in the middle panel, and the triangle in the bottom panel indicates the features of the prominence and CME core respectively which was tracked for the evolutionary studies. The cross in the middle panel and in the bottom panel indicates the feature of the leading edge of the CME.

UT and 18:42 UT respectively. The images shown in Fig. 8.6 were processed by the wavelet decomposition technique. The EIT image shows the prominence, which was later identified as the core of the CME shown in the LASCO/ C2 & C3 images. The asterisk marked in the EIT image points out the tracked feature on the prominence. For tracking, we chose the top point of the EIT prominence, assuming that the top point seen in the EIT image would be seen first in the coronagraphic image. Thus, with the diamond in the LASCO/C2 image and triangle in the LASCO/C3 image we mark what we believe is the same feature as the one in the EIT image marked by the asterisk. The cross in the middle and bottom panel represents the LE (leading edge) of the associated white-light CME.

Fig. 8.7 displays the measurements performed for the above mentioned data points. The asterisks in the figure reflect the data points obtained for evolution of the prominence in the EIT FOV, the diamonds and triangles represent the obtained data points for the core of the CME in the LASCO/C2 & C3 FOV shown in Fig. 8.6. The crosses represent the leading edge of the CME based on LASCO/C2 & C3 observations. The leading edge was not identified in the EIT images because either they were already initially large, lying outside the EIT FOV before the CME erupted or the plasma in the loops did not radiate at 195Å. The solid dots represent the data points obtained for the downflow in the EIT FOV.

In Fig. 8.7, the top panel shows the variation of the position angle of the tracked features with time. The similar variation in the position angle of the prominence in EIT, and the CME core in C2 and C3 makes the assumption more plausible that we tracked the same features in the FOV of the different instruments. As can be seen in the plot, the prominence was deflected by an angle of about $\sim 15°$ in the early phase of its evolution. Although we do not have any measurement of the leading edge during the early phase of evolution, the trend shown by the position angle in the range of 2 to 4 $R_\odot$ reveals that it also passed through a similar deflection phase as the prominence and core of the CME. The deflection observed in the prominence and the leading edge of the CME is comparable to the results derived in a systematic study by Cremades & Bothmer (2004). The downflow seems to have started at position angle 340°-345°. The position angle profile of the downflow reflects the complex motion of the downflow seen in Fig. 8.3 and 8.4.

The middle panel represents the h-t profile of the leading edge, prominence, the core of the CME and the inflow. The different symbols have the same meaning as in the top panel of Fig. 8.7. The solid line is a linear fit to the data points for the leading edge of the CME, yielding a constant speed of 860 km/s in the LASCO/C2 & C3 FOV. The dotted line is the second order polynomial fit to the data points obtained for the prominence in the EIT FOV. The dashed line is the second order polynomial fit to the data points obtained for the core of CME based on LASCO/C2 observations and the dashed-dotted line is the linear fit to the data points for the core of CME based on the LASCO/C3 observations. The overlap in the data points of LASCO/C2 & C3 makes the assumption plausible that the same feature was tracked in the C2 and the C3 FOV. The long dashed line is the second order polynomial fit to the data points obtained for the downflow based on the EIT observations. The height-time profile of the out-flowing plasma in the EIT FOV shows a positive curvature suggesting that the prominence passed through an acceleration process in

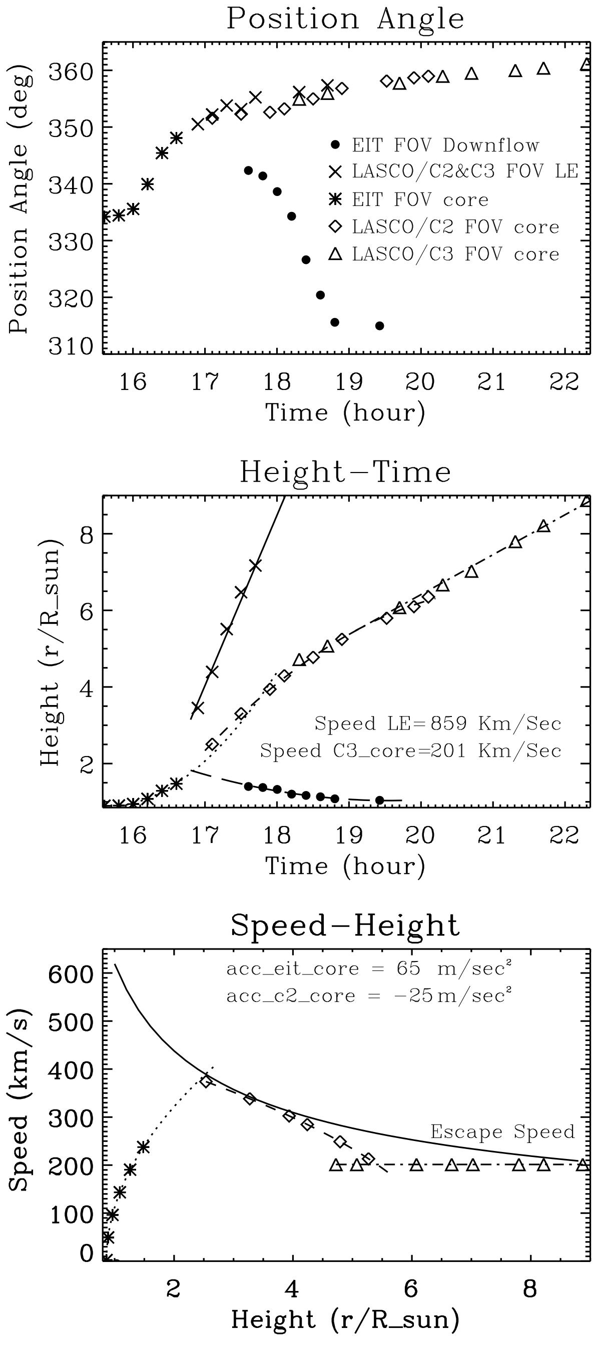

Figure 8.7: Top panel: Position angle variation for the prominence in the EIT FOV (asterisks), the core in LASCO/C2 (diamonds), the core in LASCO/C3 (triangles), the leading edge (crosses) in LASCO/C2 &C3 and the inflow in EIT FOV (solid dots). Middle panel: Height-time profile for the prominence, the core, the leading edge and the inflow. The solid and dashed-dotted lines are best linear fits to the data points. Other lines are the best quadratic fits to the data points. Bottom panel: The speed-height profiles of the features mentioned above. The speed was derived from the polynomial fits to the height-time data in the middle panel. The solid line represents the escape speed profile. The other lines are the best fits to the data points.

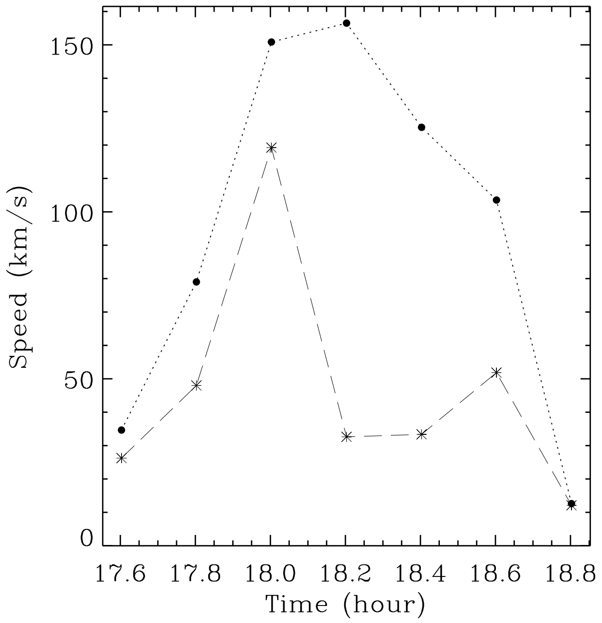

Figure 8.8: Absolute (dotted line) and vertical (dashed line) profile of the downflow.

the early phase of its evolution in agreement with the conclusion made by Webb & Jackson (1981). The measured accleration was about 65 m/s^2. Furthermore in the LASCO/C2 FOV it shows a negative curvature, suggesting a deceleration (25 m/s^2) phase. Finally, the h-t profile of the core of the CME becomes nearly a straight line corresponding to a constant speed of 200 km/s higher up in the corona. Note that there was a big difference in the speed of the core (associated prominence) and the leading edge of the CME, which travelled with a nearly constant speed of 860 km/s during the whole time that it was observed.

The h-t profile of the downflow intersects the h-t profile of the outflow at a height of about 1.8 $R_\odot$ during its deceleration phase by a simple extrapolation back in time. Therefore, it cannot be ruled out that the downward moving plasma is a part of the outward moving plasma seen earlier by EIT and the downflow started during the deceleration phase of the outflow in the height range of $1.5 - 1.8$ $R_\odot$.

The bottom panel of Fig. 8.7 displays the speed-height profile of the outflow in LASCO/C2 & C3 FOV derived from the fitted height-time polynomials in the middle panel. The symbols have the same meaning as in the top panel of Fig. 8.7. The solid line is the escape speed profile calculated for a ballistic body, only taking into acount the gravitational acceleration. By a simple extrapolation, the speed height profile of the filament intersects the escape speed profile at $\sim 2.5 R_\odot$.

Taking into account that the measured radial speed in the plane of the sky is a lower limit for the real radial speed, it seems plausible that the speed-height profile with constant acceleration of 65 km/s^2 would reach the escape speed in the height range of 1.5 to 2.0 $R_\odot$. We expect that it is measurement inaccuracies which lead the diamonds and triangles from lying below the escape speed at some heights. The observations leads us to conclude that the out-flowing plasma travels with sufficient speed to escape the Sun's gravitational field.

Further we plot in Fig. 8.8 the vertical (dashed line) and absolute projected speeds (dotted line) of the downflow as a function of time. The downflow shows a rapid acceleration in its early phase until 18:12 UT before it arrives at the kink location (see Fig 8.3). The vertical component decrease more rapidly than the absolute speed meaning that the downflow moves in the horizontal direction with decreasing altitude.

8.4 Discussion and Conclusions

A downward moving brightening was observed above post-erupitve arcades by the Extreme-ultraviolet Imaging Telescope (EIT) at 195 Å which we refer to in short as the downflow. This is the first time to our knowledge that a bright downflow has been observed at coronal temperatures. Previously observed downflows have all been dark and have been interpreted as voids. This explanation obviously does not apply to the current observations. The downflow was observed about 90 minutes after the onset of a prominence eruption (marked P1 in Figure 8.1). As seen in EIT the prominence started to erupt at around 16:00 UT and was later observed as the core of a CME after 17:06 UT by the LASCO/C2 coronagraph in white-light. Detailed analysis of the images revealed that:

1. A deflection of ∼15° towards the north pole was seen in the early phase of the prominence (P1) eruption.

2. The prominence (P1) first accelerated with a constant acceleration of about 65-70 m/s^2 in the EIT FOV (1.5 $R_\odot$), then decelerated constantly at of 25 m/s^2 in the LASCO/C2 FOV (2-5 $R_\odot$) and finally achieved a nearly constant speed of about 200 km/s higher up in the corona. The prominence is identified with the core of the CME seen by LASCO/C2 and C3.

3. The leading edge of the CME was only observed in the LASCO/C2 & C3 FOV. The leading edge moved with a speed of 860 km/s, which is much faster than the core of the CME.

4. The inflow was first seen ≈90 minutes after the eruption at a height of about 1.5 $R_\odot$ at the edge of the EIT FOV. There was no clear evidence for inflow in LASCO/C2 & C3 images.

5. The h-t profile (Fig. 8.7, middle panel) provides clear evidence that the downflow started during the deceleration phase of the core of the CME.

6. The absolute and radial projected speed of the inflow shows a rapid acceleration in its early phase before it arrives to the kink location. As soon as the inflow arrives to the kink location the radial speed shows a stronger deceleration than the absolute projected speed meaning that inflow is pushed towards the horizontal direction (see Fig. 8.8).

7. The downflow does not propagate vertically, but appears to follow paths outlining groups of loops. Two branches emanating from the same apex point are seen. The right branch shows a clear kink.

Let us now consider possible scenarios to explain these observations. Quite basically we need to distinguish between a downflow of material, downflow of energy, leading to a heating of the gas and a downward propagating cooling front. In the case of heating, a source of energy release lying outside the EIT FOV would lead to a transport of energy downwards into the field of view by conduction. The brightening occurs when the ambient gas has been heated to a temperature to which EIT is sensitive. The filamentary structure of the bright downflow requires a higher density at these filament locations or enhanced conduction along field lines. A higher density may be from gas left behind from the CME. A problem with this scenario is why the cool gas did not flow down due to gravitational attraction before it was heated up. The scale of sub-MK gas is too low for it to contribute strongly to emission at 1.5 $R_{\odot}$. The free fall time is on the order of 10^3 s, i.e. shorter than the time between the passage of the last outward bound (visible) material in the EIT FOV and the appearence of the downflow.

A cooling front provides a more viable alternative. In this case the plasma is initial too hot to be well visible in the EIT 195 Å channel. Loops at temperature 6 - 8 MK are regularly observed by Yohkoh (e.g. Nitta 2000) & SUMER (e.g. Wang et al. 2003). Cooling by radiative looses mutually propagates from regions of higher to the lower density, since radiative losses are more efficient at high density ($\sim n_e^2$). Hence the downward propagation of the cooling front would require a density excess in the higher layers, which is not straight forward to achieve. One advantage of this scenario is that the kink in the 'downflow' does not pose any problem, since the cooling front need not follow a field line.

Turning now to the actual downflow of plasma as the source of the downward propagating brightening, the plasma cannot be in free fall. The speed profile of the downflow (see Fig. 8.8) shows a rapid acceleration in the early phase which finally starts to decelerate as soon as the downflow arrives at the location of the kink. Such a behaviour would be more typically of plasma accelerated by a reconnection event taking place outside the field of view of EIT (and inside the occulting disk of LASCO C2). This interpretation is supported by the fact that in the height-time diagram (middle panel of Fig. 8.7) the extrapolations of the trajectories of the ejected prominence material and of the downflowing material intersect at around the conjectured location of the reconnection. Another argument for reconnection taking place is that the prominence material in the EIT FOV shows significant acceleration and if extrapolated along the dotted line in the bottom panel of Fig. 8.7 would reach escape speed easily. The early phase acceleration provides further evidence for magentic reconnection. Within this basic picture there are again two scenarios:

1. The plasma is flowing down freely along a field line. In this case the field line along which the right branch of the downflow moves would have to be kinked.
2. The downflow outlines the tops of an arcade of contracting loops. This model has the advantage that field lines are ejected along with rapidily flowing gas.

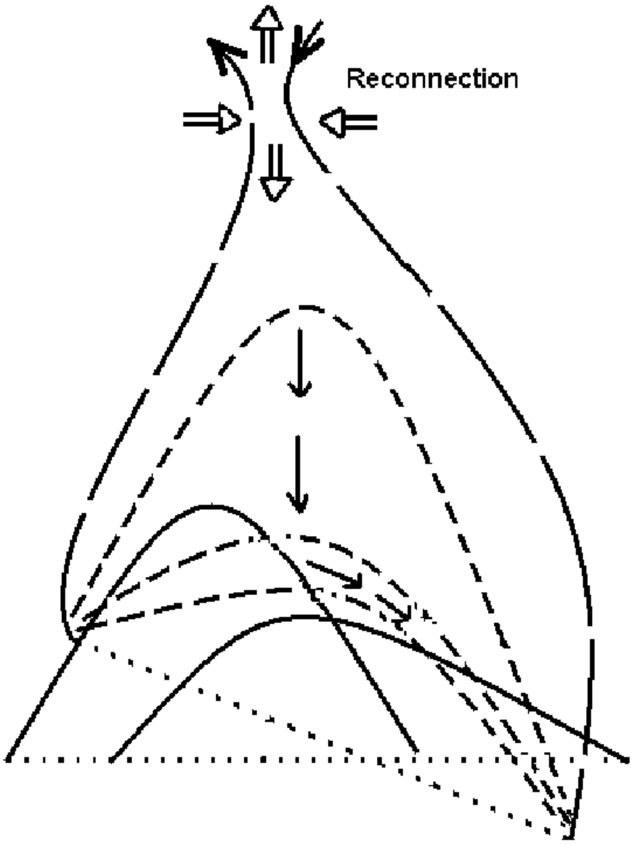

Figure 8.9: Schematic illustration of the observed downflow. The long-dashed lines are magnetic field lines initially holding the prominence. The solid field lines are post-eruptive arcades and dashed-lines are field lines after the reconnection. Arrows show the direction of motion of the downflow.

> For reconnection occuring higher up the downward accelerated field would have the right geometry.

Such loops would be aligned along the line-of-sight (making their apex brightest) and would be roughly perpendicular to the loops along which they are sliding down. The loops located on the left of the apex of the underlying loop move towards the left, those on right move down towards the right footpoint, explaining the partition into two branches. The kink is located where the contracting loop stops sliding down one loop and starts sliding down another, flatter loop with footpoints further apart.

Fig. 8.9 illustrates the magnetic field geometry associated with this scenario of the observed downflow. The long-dashed lines are field lines which were initially holding the prominence. The solid lines belong to post-eruptive arcades. The dashed lines are field lines after the reconnection which are sliding down along other field lines. The arrows indicate the direction of motion of the contracting arcade (in the illustrated case corresponding to the right hand branch of the downflow). This observation adds further evidence for the occurrence of post-CME reconnection and contraction of the drawn-out field lines.

9 Photospheric Magnetic Flux Evolution in the Source Regions of CMEs

It is believed that solar magnetic field plays an important role in the initiation of CMEs. This chapter provides a detailed and qualitative study of the evolution of the photospheric magnetic field in source regions of coronal mass ejections for a specific-set of events of the PEA database.

9.1 Introduction

One of the most interesting aspects regarding CMEs is that of their origin (Hundhausen 1999). In most of the CME theoretical models, evolution of the photospheric flux has been considered the main cause of the CME (e.g., Forbes 2000, Klimchuk 2001). In the 1970's, newly emerging flux was considered as the main trigger for solar flares and perhaps even for CMEs. Ground based observations have also shown a strong relationship between flares and the emergence of new magnetic flux (Rust 1972). Based on these observations, Heyvaerts et al. (1977) proposed a model for solar flares. In their model, a flare originates due to the sudden onset of a magnetic reconnection process between newly emerging flux and a pre-existing flux system. Later, Martin et al. (1982, 1984) found that the correlation between emerging flux and flares was not sufficiently strong to support the model. However, Feynman & Martin (1995), hereinafter F&M, argued that magnetic reconnection between newly emerging flux and pre-existing large-scale magnetic flux overlying to prominence can lead to eruption.

Based on the analysis of 30 events, F&M concluded that the eruption of the prominence/filament often occured shortly after the appearence of a new bipole in the vicinity of the filament channel. However, some cases did not fit this pattern. For example one third of the prominences erupted without detection of emerging flux and sometimes no eruption occured despite the occurrence of it.

Moreover, F&M pointed out that the orientation of a newly emerged bipole relative to the pre-existing magnetic flux did not matter if the bipole emerged inside the filament channel. However, the orientation had substantial impact when the bipole emerged outside. According to Feynman & Martin (1995), when the formation of X-line is permitted in the corona between the newly emerging bipole and pre-existing flux, then eruptions occured. This orientation was defined as the *orientation* *favorable for reconnection*. However, there were also a few cases which did not fit this pattern.

Wang & Sheeley (1999) reported three examples of filament eruptions caused through nearby emerging bipolar regions, supporting the results obtained by F&M based on EIT 195 Å and NSO magnetogram observations. However, several other examples investigated by Wang & Sheeley (1999) did not follow the suggested pattern by F&M. Therefore, Wang & Sheeley (1999) argued that an emerging bipole can contribute to the destabilization of the filament by diverting or opening up some of the magnetic flux overlying the filament. However they may not be the primary cause of the eruption.

Based on these observations, two-dimensional magnetohydrodynamic (MHD) simulations were developed (Chen & Shibata 2000; Lin et al. 2001). In these simulations flux emerged within the filament channel canceling the magnetic flux underneath a pre-existing magnetic flux-rope. The cancellation of magnetic flux causes the flux rope to rise, leaving a current sheet below. A similar kind of global restructuring of the magnetic field took place in case of bipoles emerging outside the filament channel with orientation favorable for magnetic reconnection with pre-existing flux. In either case, fast magnetic reconnection in the current sheet below the flux rope led to the its ejection. Chen and Shibata (2000) also showed that, independent of the location of flux emergence, if the orientation of the newly emerging flux was non-favorable for reconnection the eruption did not occur and the flux rope moved downwards. This contradicts the observations made by F&M (1995) that the orientation of the emerging bipole did not play a role if the bipole emerged inside the filament channel.

Recently, Linker et al. (2003) proposed a model for the process of magnetic flux cancellation. Observationally, magnetic flux cancellation is defined as the mutual disappearance of magnetic fields of opposite magnetic polarities at the polarity inversion line (Linker et al. 2003). In this model the two opposite magnetic polarities converge towards the polarity inversion line and disappear as a consequence of flux cancellation. The flux cancellation leads to production of energy where magnetic energy converts into thermal energy. Once the cancellation exceeds more than a threshold value the flux-rope violently erupts. In case of flux cancellations one would not necessarily be able to detect any flux emergence. This model probably explains filament eruptions that were not accompanied by flux emergence as observed by F&M and Wang & Sheeley (1999). There are several other models dealing with the initiation of CMEs. For a review of these models see Forbes 2000, Klimchuk 2001.

In both of the above mentioned observations the magnetograms from NSO/Kit Peak were used, which provide good spatial resolution (2 arcsec per pixel, comparable to MDI full-disk magnetogram) but poor time resolution (one image per day). High cadence (high time resolution) simultaneous observations seem to be very important in order to study the photospheric flux evolution in detail because the time-scales of CME occurrences vary from minutes to hours (Subramanian & Dere 2001). The magnetograms obtained by SoHO/MDI provide a time resolution of 96 minutes.

The list of EUV PEAs provided in appendix A offers unique opportunity to study the evolution of photospheric magnetic flux in the source regions of CMEs. This chapter explores the evolution of the photospheric magnetic flux in the source regions of CMEs associated with filament eruptions and PEAs based on MDI magnetograms.

9.2 Data Selection and Analysis

In order to study the evolution of the photospheric magnetic flux in the source regions of CMEs we selected events in which an erupting filament was seen in EIT at 195 Å and Hα filtergrams associated with an EUV PEAs and ,a white-light CME. The selected events are marked by superscript '2' in table provided in appendix A.

For the selection of the events, the spatial location and length of PEAs were considered as the main criteria. Events located near the central meridian in the heliographic latitude and longitude range between ±40° with respect to the equator and, with a length greater than or equal to 10° were selected. For these events, five-minute averaged MDI magnetograms with a cadence of 96 minutes were studied. The magnetogram data were investigated starting from the day before eruption until the day after.

The MDI magnetograms provide observations of the longitudinal component of the magnetic field. The measurements of the LOS component of the magnetic field are adversely affected by projection effects. Therefore, in order to study the characterstics of the evolution of the photospheric flux in the CME source regions, the removal of projection effects is highly important.

The full-disk images taken by MDI magnetogram were thus first remapped in order to remove the projection effects and then the region of interest was tracked by compensating for the solar rotation (see Chapter 5). For detection of the small-scale field changes we displayed the magnetograms with a threshold value of ± 200 G. The changes identified in the magnetic field pattern were then located. In summary seven events could be studied in details as described in the following sections.

9.3 Observational Summary of Events

Figures 9.1 to 9.7 display Hα, EIT 195 Å, and MDI magnetogram observations for the events on 23-Oct-1997, 24-Jun-1999, 05-Mar-2000, 29-Apr-2000, 31-May-2000, 04-Sep-2000 and 12-Sep-2000 respectively.

Top panels in all figures provide Hα (upper row) and EIT 195 Å (lower row) observations. Hα images are displayed before (left image) and after (right image) the eruption. Only a few Hα observations is provided every day and therefore some images that correspond to some earlier times. However, Hα images taken after the eruption correspond to the observation made on the day of eruption except for the event on 31-May-2000 because there was no Hα observation for this day. Boxes shown in Hα images taken before the eruption, represent the region for which the magnetogram data were studied in detail. Arrows inside the boxes locate the position of the identified flux-changes based on the MDI magnetogram observations. The lower rows in the top panel of figures display EIT 195 Å running difference images showing the eruption of a filament (left image) followed by the formation of the post-eruptive arcades (right images). The site of the filament eruptions and formations of the post-eruptive arcade is located by arrows.

The bottom panels display the portion of the full-disk MDI magnetograms corresponding to the regions inside the boxes in the upper rows of the top panels. We have analyzed MDI magnetograms taken every 96 minutes starting a day before until the day after the eruption. However the magnetograms shown are temporaly separated by about 12 hours. Arrows in the magnetograms show the location of identified changes in the magnetic field. Location shown by arrows in magnetograms corresponds to locations pointed by arrows in the Hα images. Details about particular events are provided in figure captions. Table 9.1 provides the observational characterstics for individual events.

Table 9.1: Observational summary of the analyzed events. Columns from left to right: Date of observation; onset time of associated CME based on backward extrapolation of height-time diagrams; category of the magnetic flux evolution; location of the identified change in the magnetic field with respect to (w.r.t.) the filament; site of activation of the filament; orientation of the emerging flux based on Feynman & Martin (F & M, 1995); and time of identification of major change in the magnetic field pattern.

Date	**CME onset time UT**	**Category of flux evolution**	**Location of identified change w.r.t. filament**	**Site of filament activation**	**Orientation as defined by F & M (1995)**	**Identification time of flux evolution**
23-Oct-1997	11:12	Flux cancellation	At both foot-points	Near the cancellation site	– – –	27 hours earlier
24-Jun-1999	13:10	Flux cancellation	At southern foot-point	Near the cancellation site	– – –	37 hours earlier
05-Mar-2000	07:00	Near-by AR evolution	Near southern foot-point	Near the evolution site	Favorable for reconnection	23 hours earlier
29-Apr-2000	04:19	Near-by AR evolution	Near northern foot-point	Near the evolution site	Favorable for reconnection	Emerged day before and evolved during the eruption
31-May-2000	06:36	Bipole emergence	Out-side the filament channel	– – –	Non-favorable for reconnection	16 hours earlier
04-Sep-2000	05:29	Bipole emergence	Inside filament channel	Opposite end to emergence site	Not applicable	12 hours earlier
12-Sep-2000	11:12	Bipole emergence	Inside filament channel	Near the emergence site	Not applicable	7 hours earlier

Event on 23 - Oct - 1997

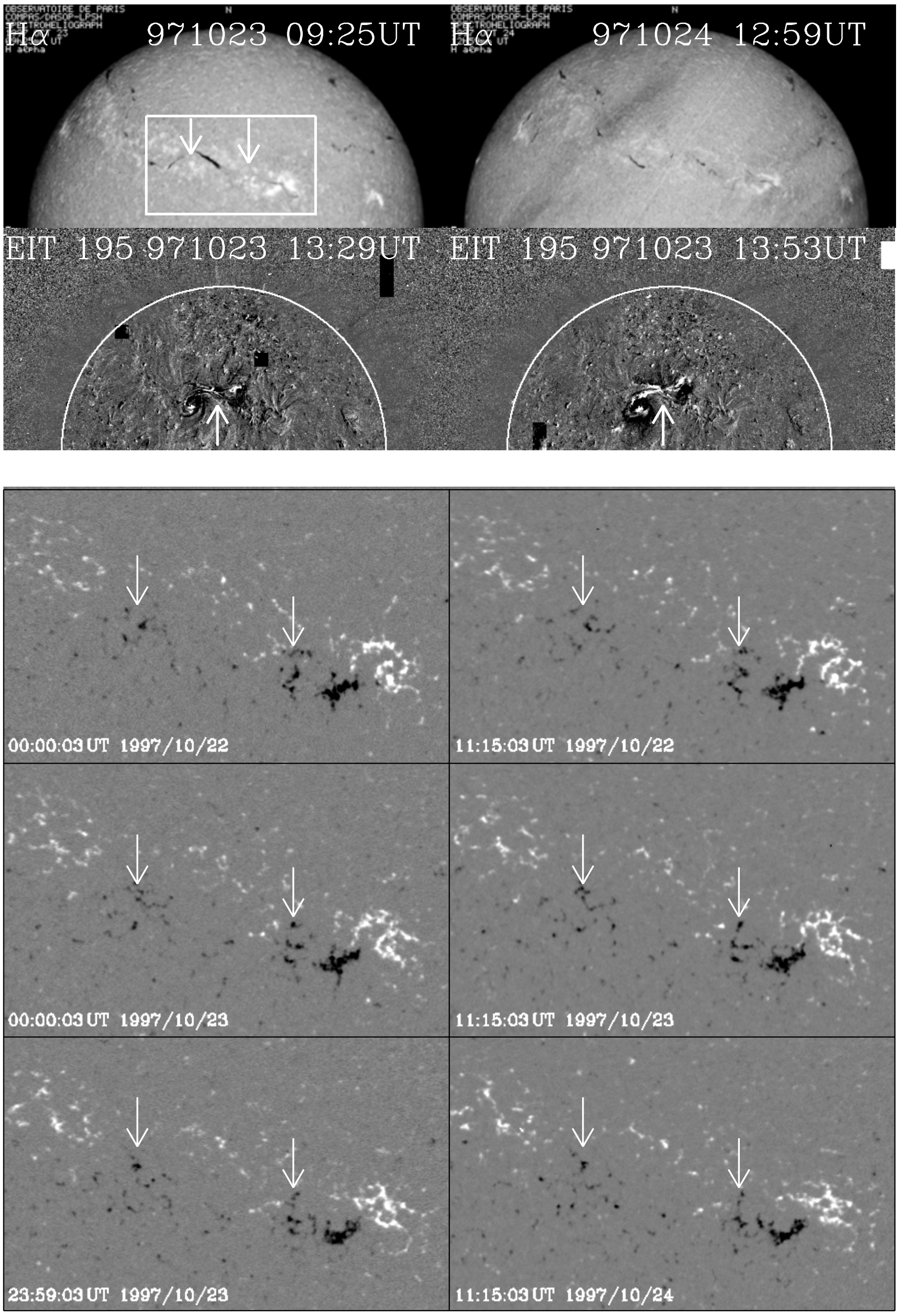
Hα 971023 09:25UT
Hα 971024 12:59UT
EIT 195 971023 13:29UT
EIT 195 971023 13:53UT
00:00:03 UT 1997/10/22
11:15:03 UT 1997/10/22
00:00:03 UT 1997/10/23
11:15:03 UT 1997/10/23
23:59:03 UT 1997/10/23
11:15:03 UT 1997/10/24

Figure 9.1: **Top Panel:** Hα (upper row) and EIT 195 Å running difference (bottom row) images for the event on 23-Oct-1997. The box in the upper left image represents the region for which MDI magnetogram data were studied in detail. Arrows in the upper left image locate identified changes in the magnetic field based on the magnetogram observations. EIT running difference images (lower row) showing the eruption of the filament followed by formation of the PEA underneath. The site of filament eruption and PEA is located by arrows. **Bottom panel:** Portion of full-disk MDI magnetograms corresponding to the box shown in top panel. Arrows demark the locations of *flux cancellations*. Arrows correspond to locations demarked by arrows in the upper left image in the top panel. Time is running from left to right and from top to bottom. In all images North points upward and West towards the right.

Event on 24 - Jun - 1999

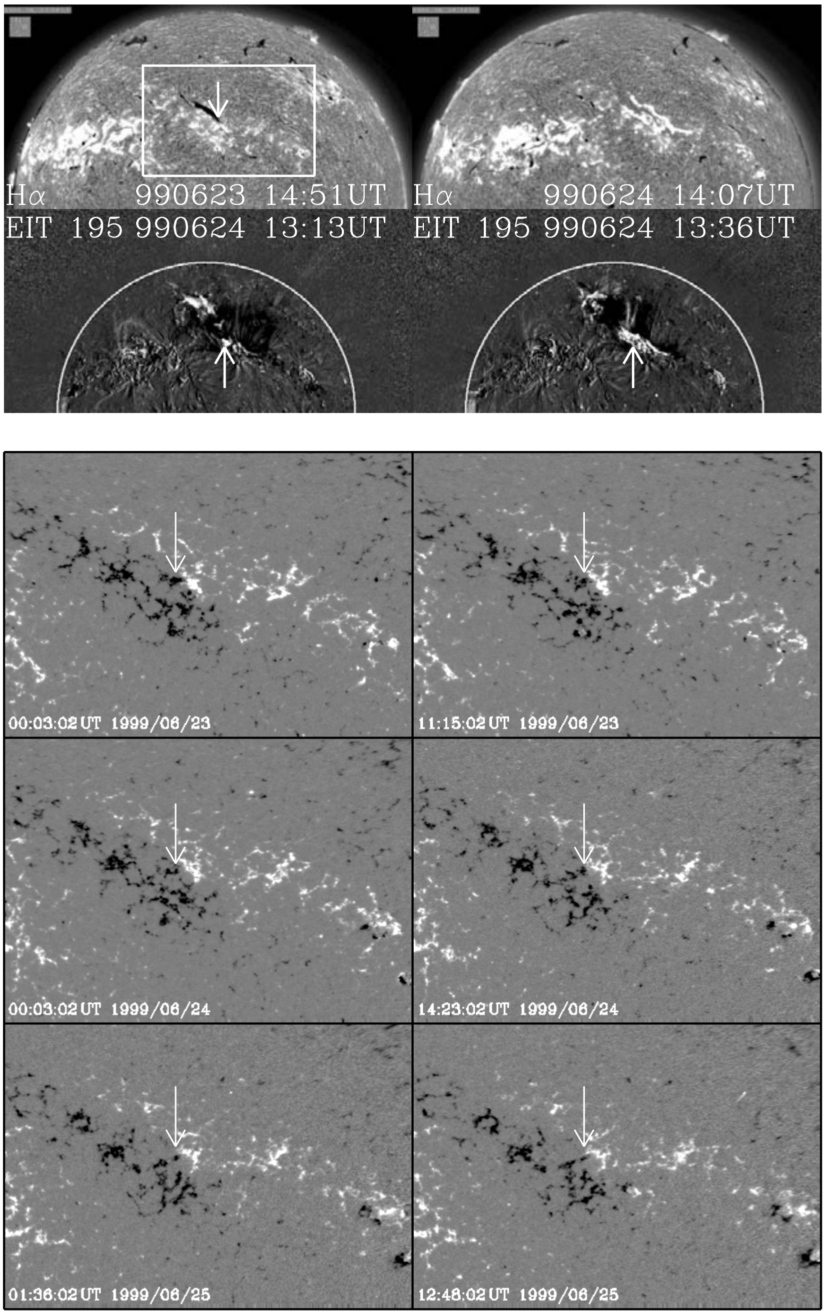
Hα 990623 14:51UT
Hα 990624 14:07UT
EIT 195 990624 13:13UT
EIT 195 990624 13:36UT
00:03:02 UT 1999/06/23
11:15:02 UT 1999/06/23
00:03:02 UT 1999/06/24
14:23:02 UT 1999/06/24
01:36:02 UT 1999/06/25
12:48:02 UT 1999/06/25

Figure 9.2: **Top Panel:** Hα images (upper row) taken before and after the eruption for the event on 24-Jun-1999. The box in the upper left image demarks the region for which the MDI magnetogram data were studied in detail. The arrow corresponds to the location of identified changes in the magnetic field based on magnetogram observations. EIT running difference images (lower panel) showing the eruption of the filament followed by formation of PEA underneath. The site of filament eruption and formations of PEA is marked by arrows. **Bottom panel:** A portion of MDI magnetogram images corresponding to the box shown in top panel. Arrows demark the location of *flux cancellations*. Arrows in magnetograms correspond to locations shown by an arrow in the upper left image in the top panel. In all images North points upward and West towards the right.

Event on 05 - Mar - 2000

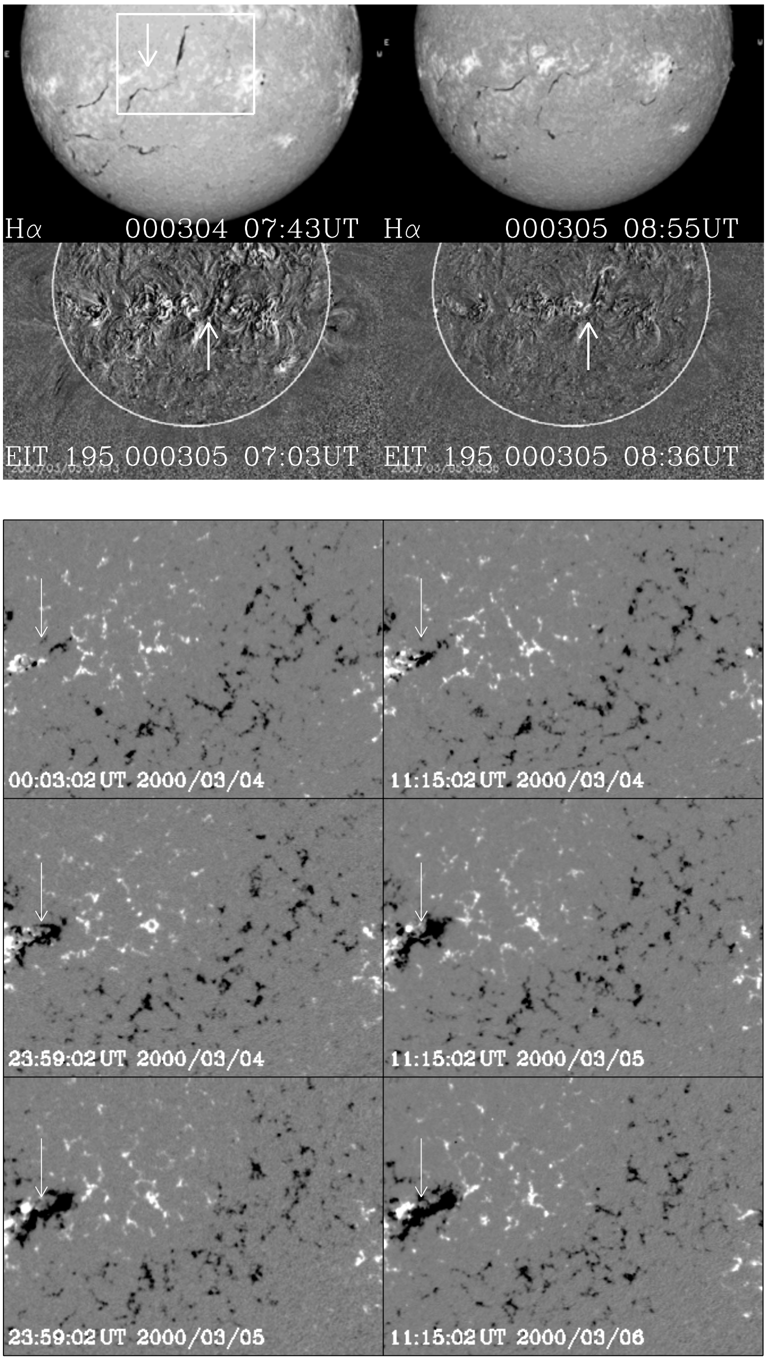
Hα 000304 07:43UT
Hα 000305 08:55UT
EIT 195 000305 07:03UT
EIT 195 000305 08:36UT
00:03:02 UT 2000/03/04
11:15:02 UT 2000/03/04
23:59:02 UT 2000/03/04
11:15:02 UT 2000/03/05
23:59:02 UT 2000/03/05
11:15:02 UT 2000/03/06

Figure 9.3: **Top Panel:** Hα images (upper row) taken before and after the eruption for the event on 05-Mar-2000. The box in the upper left image shows the region for which the MDI magnetogram data were studied in detail. The arrow corresponds to the location of identified changes in the magnetic field based on magnetogram observations. EIT running difference images (lower row) showing the eruption of the filament followed by formation of a PEA underneath. The site of filament eruption and formation of PEA is located by arrows. **Bottom panel:** A portion of MDI magnetogram images corresponding to the box shown in top panel. Arrows locate the *evolution in a near-by active region.* Arrows in magnetograms correspond to location shown by an arrow in the upper left image in the top panel. In all images North points upward and West towards the right.

Event on 29 - Apr - 2000

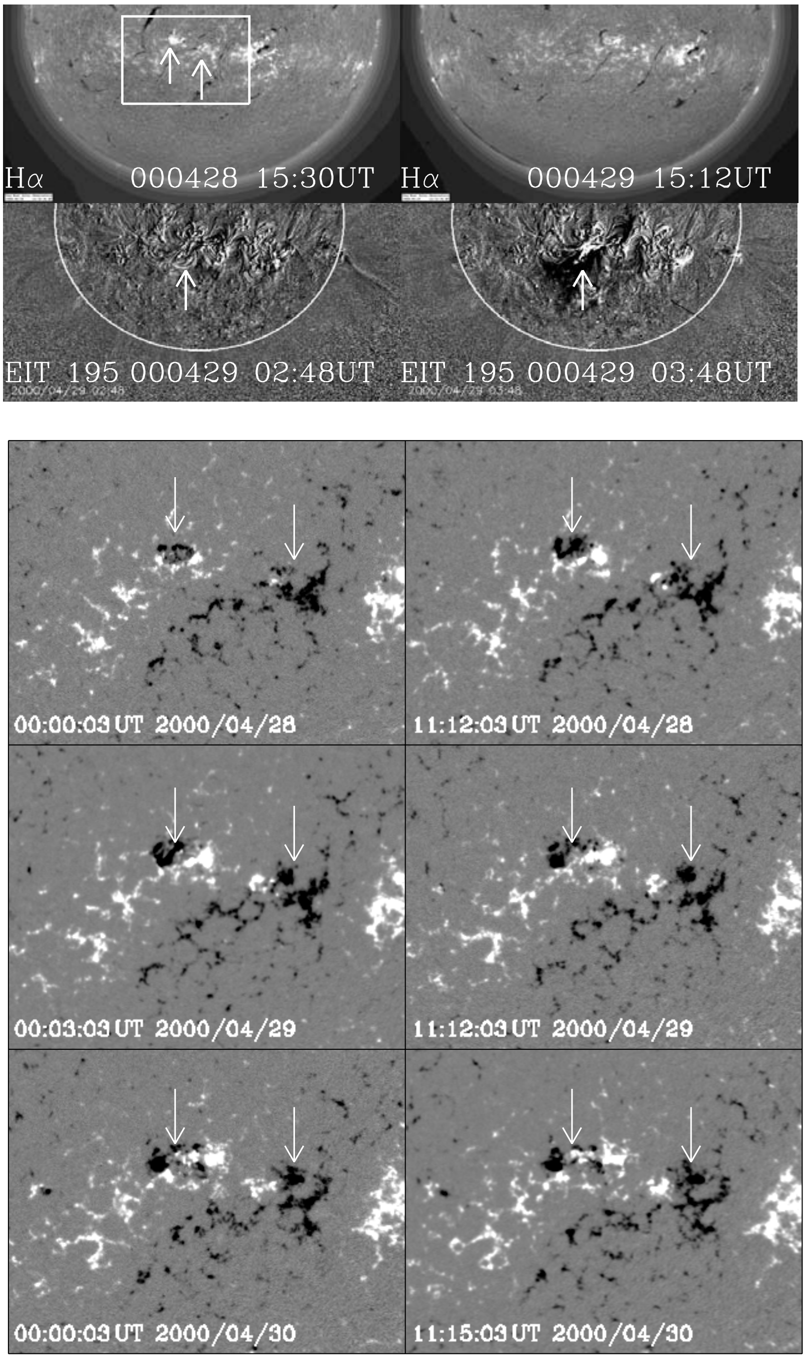
Hα 000428 15:30UT
Hα 000429 15:12UT
EIT 195 000429 02:48UT
EIT 195 000429 03:48UT
00:00:03 UT 2000/04/28
11:12:03 UT 2000/04/28
00:03:03 UT 2000/04/29
11:12:03 UT 2000/04/29
00:00:03 UT 2000/04/30
11:15:03 UT 2000/04/30

Figure 9.4: **Top Panel:** Hα images (upper row) taken before and after the eruption for the event on 29-Apr-2000. The box in the upper left image shows the region for which the MDI magnetogram data were studied in detail. Arrows correspond to the location of identified changes in the magnetic field based on magnetogram observations. EIT running difference images (lower row) showing the eruption of the filament followed by formation of a PEA underneath. The site of filament eruption and formation of PEA is located by arrows. **Bottom panel:** A portion of MDI magnetogram images corresponding to the box shown in top panel. Arrows locate the *evolution in near-by active regions on both sides of the filament.* Arrows in magnetograms correspond to locations shown by arrows in the upper left image in the top panel. In all images North points upward and West towards the right.

Event on 31 - May - 2000

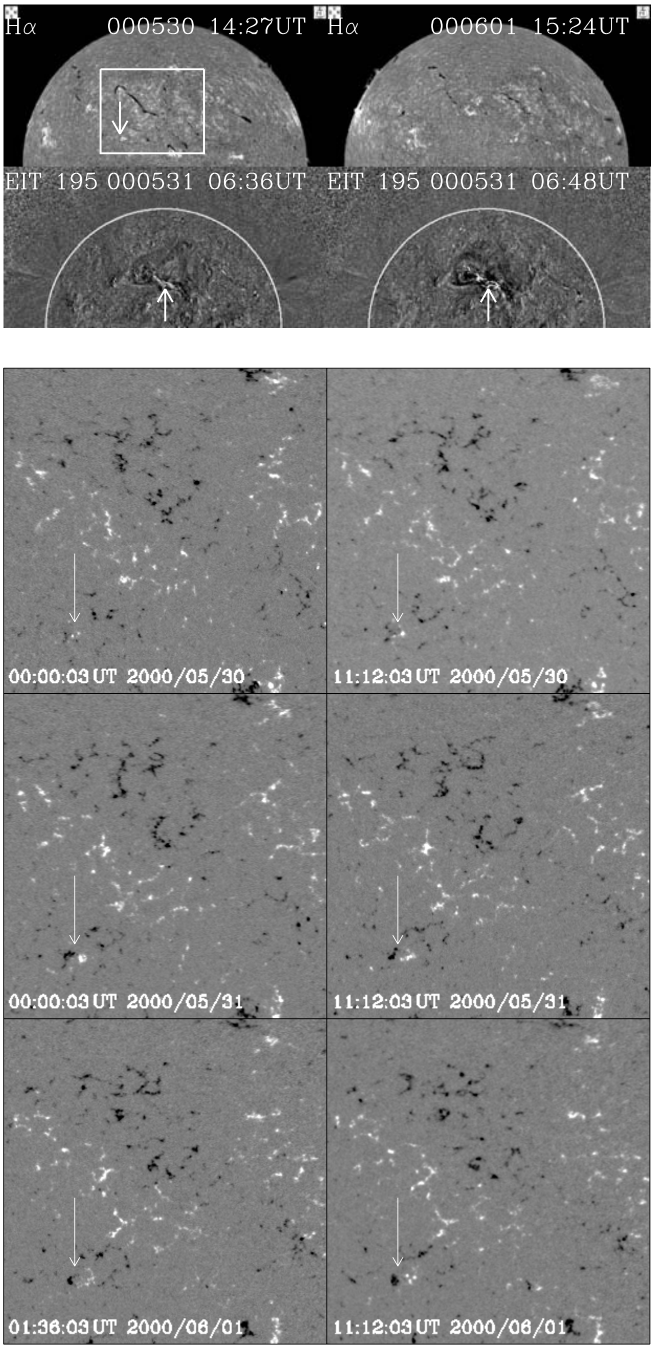
Hα 000530 14:27UT
Hα 000601 15:24UT
EIT 195 000531 06:36UT
EIT 195 000531 06:48UT
00:00:03UT 2000/05/30
11:12:03UT 2000/05/30
00:00:03UT 2000/05/31
11:12:03UT 2000/05/31
01:36:03UT 2000/06/01
11:12:03UT 2000/06/01

Figure 9.5: **Top Panel:** Hα images (upper row) taken before and after the eruption for the event on 31-May-2000. The box in the upper left image shows the region for which the MDI magnetogram data were studied in detail. Arrow corresponds to the location of identified changes in the magnetic field based on magnetogram observations. EIT running difference images (lower row) showing the eruption of the filament followed by formation of a PEA underneath. The site of filament eruption and formation of PEA is located by arrows. **Bottom panel:** A portion of MDI magnetogram images corresponding to the box shown in top panel. Arrows locate the *emergence of a new bipole out-side the filament channel.* Arrows in magnetograms correspond to location shown by arrow in the upper left image in the top panel. In all images North points upward and West towards the right.

Event on 04 - Sep - 2000

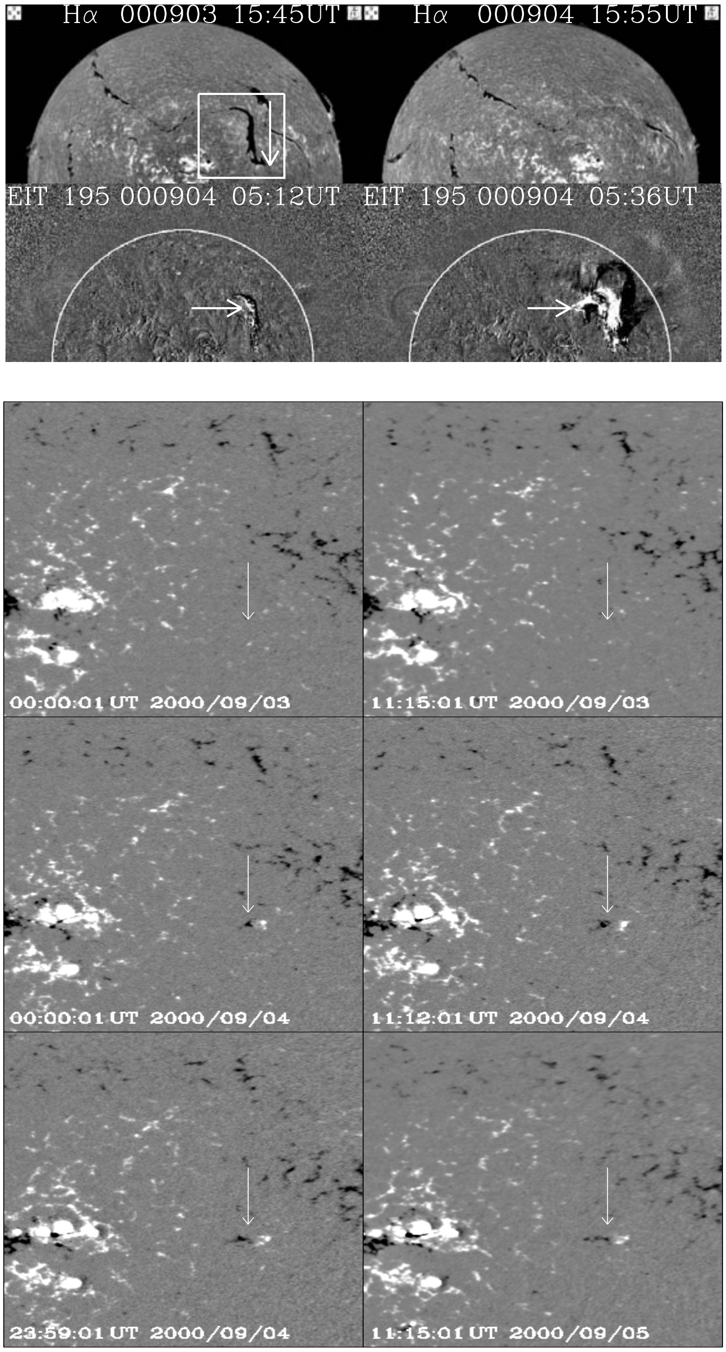
Hα 000903 15:45UT
Hα 000904 15:55UT
EIT 195 000904 05:12UT
EIT 195 000904 05:36UT
00:00:01 UT 2000/09/03
11:15:01 UT 2000/09/03
00:00:01 UT 2000/09/04
11:12:01 UT 2000/09/04
23:59:01 UT 2000/09/04
11:15:01 UT 2000/09/05

Figure 9.6: **Top Panel:** Hα images (upper row) taken before and after the eruption for the event on 04-Sep-2000. The box in the upper left image shows the region for which the MDI magnetogram data were studied in detail. Arrow corresponds to the location of identified changes in the magnetic field based on magnetogram observations. EIT running difference images (lower row) showing the eruption of the filament followed by formation of a PEA underneath. The site of filament eruption and formation of PEA is located by arrows. **Bottom panel:** A portion of MDI magnetogram images corresponding to the box shown in top panel. Arrows locate the *emergence of a new bipole inside the filament channel at one foot-point.* Arrows in magnetograms correspond to location shown by arrow in the upper left image in the top panel. In all images North points upward and West towards the right.

Event on 12 - Sep - 2000

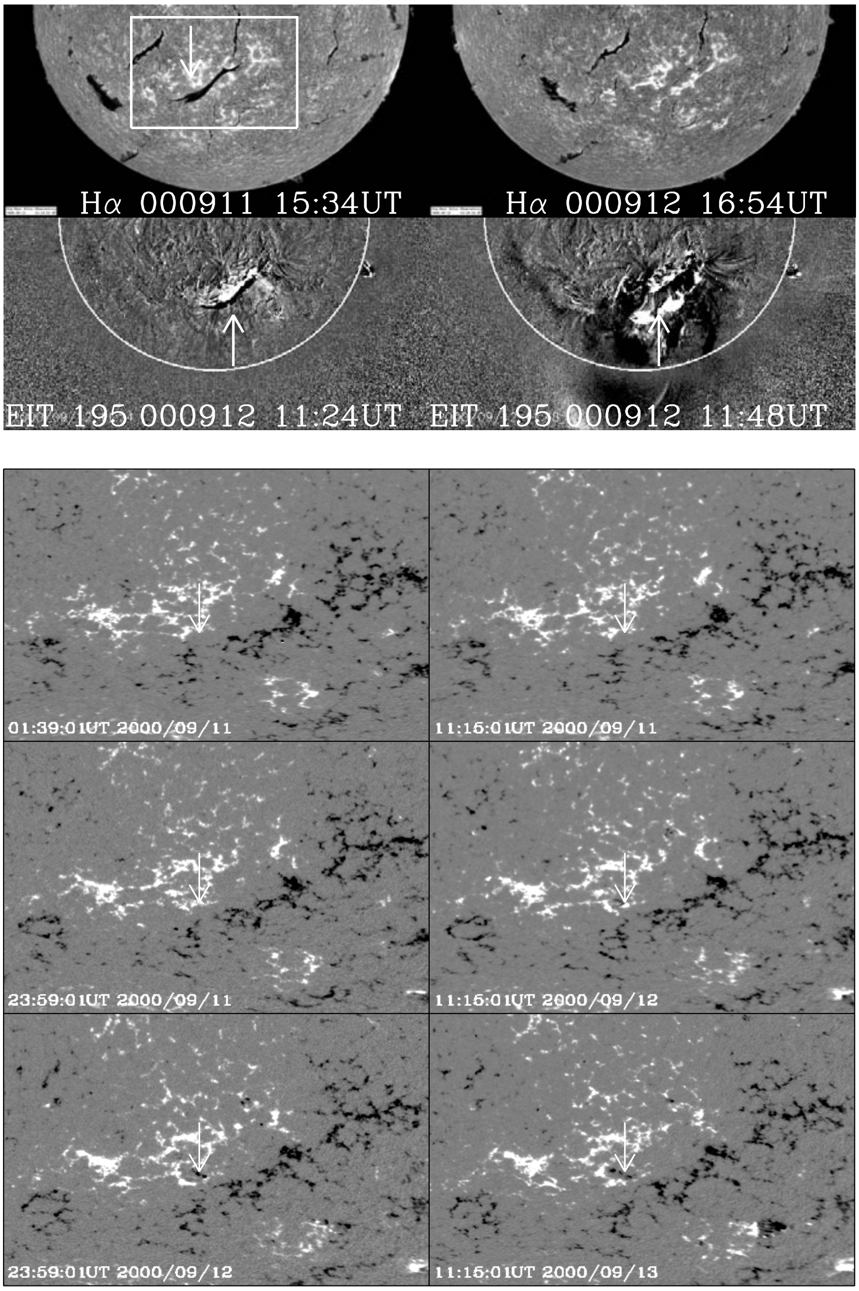
Hα 000911 15:34UT
Hα 000912 16:54UT
EIT 195 000912 11:24UT
EIT 195 000912 11:48UT
01:39:01UT 2000/09/11
11:15:01UT 2000/09/11
23:59:01UT 2000/09/11
11:15:01UT 2000/09/12
23:59:01UT 2000/09/12
11:15:01UT 2000/09/13

Figure 9.7: **Top Panel:** Hα images (upper row) taken before and after the eruption for the event on 12-Sep-2000. The box in the upper left image shows the region for which the MDI magnetogram data were studied in detail. Arrow corresponds to the location of identified changes in the magnetic field based on magnetogram observations. EIT running difference images (lower row) showing the eruption of the filament followed by formation of a PEA underneath. The site of filament eruption and formation of PEA is located by arrows. **Bottom panel:** A portion of MDI magnetogram images corresponding to the box shown in top panel. Arrows locate the *emergence of a new bipole inside the filament channel.* Arrows in magnetograms correspond to location shown by arrow in the upper left image in the top panel. In all images North points upward and West towards the right.

9.4 Discussion and Conclusions

We have analyzed seven EUV PEA events associated with Hα filament eruption events in the heliographic coordinates range from ± 40 degrees with respect to the solar equator. Based on the changes seen in the magnetic field we have classified our set of events into three different categories: flux cancellations, evolution in nearby active regions and emergences of a new bipolar regions. The cases with flux emergence have been sub-divided as: flux emergence outside, in the vicinity of the filament channel, and inside the filament channel. The observational summary for each event is provided in Table 9.1.

In two (24-Jun-1999 & 23-Oct-1997) cases flux cancellation was seen whereas in two cases (05-Mar-00 & 29-Apr-00) it seems that the eruption of the filament took place because of the perturbation created by flux evolution of the active region located near one of the foot points of the filament. Emergence of a new bipole was identified in three cases (31-May-2000, 04-Sep-2000, 12-Sep-2000). For one of the events (31-May-2000) the emergence of a bipole was seen outside the filament, and in two events (04-Sep-2000, 12-Sep-2000), the emerging flux was identifed inside the filament channel.

The magnetic flux with two different polarities shows the mutual cancellation of flux which decreases the local magnetic pressure. The resulting gradient in magnetic pressure causes the magnetic plasma on both sides of the neutral line to move towards each other. The frozen-in field lines accumulate to form a current sheet (Chen & Shibata 2000). Owing to the low-β of the corona, the cross field current is concentrated in a thin layer near the neutral line. At the same time the inflow pushes the flux-rope upward, leading to the onset of the flux ejection and perturbing the filament which was already in a metastable state in the form of a flux-rope system where the filament material is supposed to be held at the bottom of the flux-rope by the magnetic field lines. A little perturbation beneath the flux-rope or in the vicinity of it could create enough instability for the flux-rope to eventually erupt. As discussed by Linker et al. (2003) using two-dimensional MHD simulation, flux cancellation first leads to formation of a flux-rope which stays in a metastable state. When the critical threshold of flux cancellation is exceeded, the flux-rope system erupts violently. We interpret our observation as being consistent with the results by Linker et al. (2003). As explained by Linker et al. (2003) a significant amount of the flux cancellation can produce enough energy leading to the filament eruption.

For two events (05-Mar-2000 & 29-Apr-2000), evolution in the active region near one of the filament's foot points was observed before and during the eruption. For the event on 05-Mar-2000, the orientation of the evolving active region was such that it permitted the formation of X-line in the corona with pre-existing flux. For the event on 24-Apr-2000 the evolving active regions were identified on both side a foot point of the filanment. One of the active regions showed the appearence of parasitic polarity (e.g., Subramanian & Dere 2001).

When the emerging flux was outside (31-May-2000) the filament channel the orientation of the emerging flux was not found to be favorable for formation of X-line in the corona as introduced by F&M. However the filament erupted contradictory to the predictions of F&M. In two cases (04-Sep-2000 & 12-Sep-2000) the emerging flux was observed inside the filament channel. For the event on 12-Sep-2000, the flux emergence was identified to be in the middle of the filament channel. The filament erupted very homogeneously. In the event on 04-Sep-2000 the flux emergence was observed at one of the foot points of the filament. In this case the eruption started at the farther end of the filament and not at the end where the flux emergence was identified. So this event makes us sceptical about the assumption that emergence of the bipole near-by or inside a filament can lead to the eruption. As pointed out by Wang & Sheeley (1999) an emerging flux may not be necessary to trigger the eruption of a filament but it can catalyze the eruption. Our studies seem to confirm the validity of this statement.

10 Summary and Conclusions

In this thesis I have studied the basic physical properties of EUV post-eruptive arcades (PEAs) and their role as tracers of coronal mass ejections (CMEs) based on the observations made by the *Extreme-ultraviolet Imaging Telescope* (EIT), *Large Angle Spectrometric Coronagraph* (LASCO) and *Michelson Doppler Imager* (MDI) aboard the *Solar and Heliospheric Observatory* (SoHO). Complementary observations were taken into account using *Soft X-ray Telescope* (SXT) aboard *Yohkoh* and *ground-based Hα* images from Meudon Observatory Paris & Big Bear Solar Observatory (BBSO) California.

From a careful inspection of the full data-set of EIT 195 Å observations taken from 1997 to 2002, a data-set of 236 PEA events were compiled, with the requirement that each PEA needed to be observable over its full spatial extent on the visible solar disk. PEAs are defined as transient brightening of large-scale ($\approx 5°$ heliographic length) loop systems over periods of several hours. This data-set was used for a systematic study of the basic physical properties of PEAs such as *heliographic length, life-time, variation of lengths with latitude during the current solar cycle.* Additionally, *the magnetic field configurations in their photospheric source regions* were investigated based on the MDI data.

The association between each EUV PEA and white-light CME detected by LASCO/C2 coronagraph was studied based on position angle and height-time (h-t) measurements for corresponding CMEs. The position angle provided informations about the spatial location of the CME on the solar disk and h-t diagram provides the approximate onset time. This study yielded the following major result:

- *For each EUV PEAs observed by SoHO/EIT at 195 Å and white-light CMEs detected by SoHO/LASCO was found i.e., for every EUV PEA there is an associated CME but the converse is not observed. Therefore, PEAs can be considered as reliable disk tracers of CMEs. Hence full-disk images taken at 195 Å can provided informations on CME events even without simultaneous coronagraph observations* (see Chapter 7, section 7.2).

For four events a systematic study of the chronological evolution of EUV PEAs was performed based on EIT, Yohkoh/SXT and GOES 8 (Geostationary Operational Environmental Satellite) observations. In these events *the rising phase of the X-ray flare coincided with the acceleration and lift-off phase of the CMEs. Some minutes after the peak in X-ray intensity, EUV PEAs' formed in the low corona. The coronal brightenings observed by SXT preceded the onset of the EUV PEAs by 5 to 30 minutes. Thus PEAs can be interpreted as the coronal signature of the aftermath of a CMEs in the course of its magnetic restructuring* (see Chapter 7, section 7.4).

The PEA event on 05-Mar-2000 was studied in detail because it showed, to our knowledge the first ever seen, *bright downflow* of material at 1.5 MK above the PEA. The PEA formed after the eruption of a prominence associated CME. The downflow was detected by EIT approximately 90 minutes after the eruption. Running difference and wavelet analysis techniques were applied for specific data analysis. The evolution of the prominence seen by EIT was tracked into the LASCO/C2 and C3 field-of-view where it developed as the core of a typical three-part CME. In contrast to the inflow structures observed in recent studies (e.g., Wang et al. 1999, Asai et al. 2004), which were *dark* and were interpreted as *plasma voids* moving down, the inflow reported here was *bright.* The speed of the inflow, which was only seen in EIT FOV, was ≈ 50-100 km/s at a height between 1.5 and 1.2 $R_\odot$, coinciding with the deceleration phase of the core of the CME. The downflow appeared to be rapidly accelerated during its early phase before it reached to the kink location.

- *The downflow followed a curved path suggesting the apex of a contracting magnetic loop sliding down along groups of other field lines. This observation provides support for the pinching off of the field lines drawn-out by the erupting prominences and the contraction of the arcade formed by the post-CME reconnection* (see Chapter 8).

For specifically selected events near central meridian, the evolution of the photospheric magnetic field in the source regions of CMEs was investigated to understand whether the photospheric magnetic flux changes may initiate the CME event. Seven well-observed disk-centered (heliographic coordinate range between ± 40° with respect to the solar equator) PEA events with lengths greater than or equal to 10° were selected to reduce of the impact of the line-of-sight effect. The evolution of the longitudinal photospheric magnetic field was studied based on SoHO/MDI observations. The full-disk magnetograms obtained from SoHO/MDI were remapped in order to remove any projection effects and were also compensated to account for solar rotational effects (see Chapter 5).

- *In two events, cancellation of magnetic flux near the polarity inversion line was identified at one of the foot-points of the disappearing filament. In two other events, one of the foot-points of the filament was rooted close to a near-by evolving active region. The evolving active region was observed with polarity orientation favorable for magnetic reconnection (Feynman & Martin 1995). In three events newly emerging bipoles were seen around the time of eruption of the filaments. In one event the biople emerged outside the filament channel with a magnetic orientation non-favorable for magnetic reconnection. However, in the other two events the emerging flux was observed inside the filament channel.*

The analysis of seven events shows that there seem to be no unique photospheric features signaling the onset of a CME. However, further studies with higher time resolution and vector measurements of the photospheric magnetic field are needed to study the coupling between the photosphere and the corona in sufficient detail.

Perspectives

The long-term goal concerning the research on solar eruptions will be to predict the onset of a coronal mass ejection and its evolution in the solar corona and heliosphere, and finally whether it will arrive at Earth and with which space weather consequences.

Based on the results of this thesis, EUV post-eruptive arcades (PEAs) provide an unambiguous solar disk signature for the occurrence of a CME even without simultaneous coronagraph observations. This is a very important aspect for space weather predictions because CMEs heading towards the Earth are hardest to observe because of projection effects since front-side halo CMEs appear as transparent unstructured bubbles in white-light. They are also often detected relatively late after their onset compared to CMEs observed at the solar limbs. However, it should be noted that we currently do not understand which CMEs do lack PEA signatures.

In some of the PEA events of this study, the corresponding CMEs caused geomagnetic storms, as for the giant PEA observed on 14-Jul-2000 and the one detected on 17-Feb-2000 (see e.g., Bothmer 2003; Yurchyshyn et al. 2001). In both cases, the in-situ magnetic field properties of the CMEs matched the one predicted from the photospheric pattern of the CME source regions according to the scenario presented by Bothmer and Schwenn (1994, 1998) and Bothmer and Rust (1997).

Because of the reliability of PEA events as tracers of the solar source regions of CMEs, which can not be inferred from white-light observations in which the disk is blocked out, the compiled PEA list of this thesis provides an important data set to further investigate the source regions of CMEs in the low corona and photosphere to help understand further the physical mechanisms that trigger CMEs.

A bright downflow above the post-eruptive arcade, identified for the first time in the field-of-view of SoHO/EIT, yielded insight in the complicated kinematics of CME onsets and the physical properties of the accelerated coronal and prominence material. Based on the detailed analysis of this event, the downflow can be considered as evidence for magnetic reconnection processes above the corresponding PEA. The special spatial geometry visible in this particular event argues in favor of a scenario in which a CME does not only includes rising coronal loops, but that also shrinking loop systems form below the CME. Systematic studies of further events are needed to prove this hypothesis.

Beyond the potential of PEAs as disk signatures for improved space weather predictions, the large list of identified PEAs in this thesis provides a unique data-set to study the underlying photospheric magnetic field configurations and the responsible mechanisms for CME initiations which can be compared with existing theoretical CME models. Here, the photospheric magnetic field was studied using SoHO/MDI magnetic field measurements for seven relatively large-scale PEA events associated with disappearing filaments, which occurred near central meridian so that the line-of-sight events could be substantially reduced. In each case evidence was found that changes in the photospheric magnetic flux in or near the CME source regions could have led to magnetic instabilities and a subsequent release of the CME.

MDI magnetograms are of relatively low time cadence and do not provide vector magnetic field measurements. Future studies based on the availability of such measurements on the solar disk and simultaneously white-light observations taken from different perspectives will certainly shed new light on the expected coupling between the source surface field changes and the overlying coronal field evolution.

The upcoming STEREO (Solar TErrestrial RElation Observatory) and Solar-B NASA space missions with planned launches in 2006 will provide exactly the so far missing data to prove the validity of the results deduced in this thesis. The Solar-B data will include vector magnetograms with a spatial resolution of 0.1 arcsec per pixel as well as sensitive X-ray images of the whole Sun so that it is suitably equipped for studying the underlying magnetic fields and their evolution before, during, and after the onset of a CME together with the STEREO observations. The data will also allow to answer the questions which CMEs are associated with EUV PEAs and which ones are not. Both missions will definitely provide a new picture on the physics of solar transients and its heliospheric consequences.

A Observation Table

Table A.1: The columns from left to right present the following PEA parameters: Date of observation based on SoHO/EIT 195 Å observations during 1997-2002, time of maximum evolution at 195 Å, heliographic coordinates (latitude b, longitude l) of the two endpoints of the PEA axis, heliographic length, negative (n) or positive (p) magnetic polarity to the West of the polarity inversion line (PIL), lifetime, time of first observation of the associated SoHO/LASCO C2 CME. In the last column, cases without availability of LASCO/C2 data are marked as NA (not applicable) and DF represents the disppearing filament.

Date	*Time* (UT)	b_1 (deg)	l_1 (deg)	b_2 (deg)	l_2 (deg)	L (deg)	*Polarity* $to\mathrm{W}ofNL$	*lifetime* (hrs)	$T_{LASCO/C2}$ (UT)
07-Feb-97	07:03	−23.97	43.15	−51.02	13.92	35	*n*	16:00	00:30
07-Apr-97	15:15	−26.21	−16.43	−33.50	−24.10	10	*n*	08:40	14:27
12-May-97	06:22	18.00	8.97	26.08	7.33	8	*p*	06:36	06:30
22-Aug-97	09:59	18.62	− 34.71	35.11	− 53.90	24	*p*	14:00	06:45
30-Aug-97	01:12	31.71	− 10.95	29.96	−13.48	3	*p*	10:12	01:30
21-Oct-97	73:40	−27.74	−35.26	−31.97	−62.17	24	*p*	09:16	01:27
21-Oct-97	17:45	14.49	−1.96	19.86	−9.75	9	*p*	05:04	18:03
23-Oct-97[2]	15:08	22.13	−2.46	21.95	−15.77	12	*p*	07:38	11:26

Table 1 - *Continued*

Date	*Time* (UT)	b_1 (deg)	l_1 (deg)	b_2 (deg)	l_2 (deg)	L (deg)	*Polarity* *to*W*ofNL*	*lifetime* (hrs)	$T_{LASCO/C2}$ (UT)
08-Nov-97	23:52	−21.49	29.27	−34.57	10.99	21	n	13:38	− − −
06-Dec-97	19:51	23.30	49.32	34.51	36.16	16	p	06:00	10:27
03-Jan-98	03:22	22.56	45.82	32.07	33.33	15	p	06:37	23:28
03-Jan-98	11:41	37.69	74.02	42.79	44.92	23	n	01:37	09:42
03-Jan-98	23:13	30.17	13.59	34.22	3.18	10	n	03:51	− − −
25-Jan-98	16:28	20.55	−21.39	27.95	−32.36	12	p	08:33	15:26
24-Feb-98	00:20	23.86	−2.89	25.87	−14.44	11	p	02:00	23:27
28-Feb-98	15:21	23.53	30.96	35.68	20.97	15	p	14:00	10:22
10-Mar-98	12:00	−20.43	−13.90	−28.14	−21.13	10	n	05:09	05:34
26-Mar-98	14:57	−41.39	−19.97	−25.82	−21.31	16	p	06:38	09:42
27-Mar-98	01:29	20.71	−29.71	29.04	−39.52	12	p	12:46	01:23
28-Mar-98	23:34	27.02	12.95	26.84	0.43	11	n	04:10	22:41
14-Apr-98	17:20	18.06	−65.19	27.11	−71.25	11	p	11:20	05:26
15-Apr-98	10:20	29.04	22.02	28.66	7.89	12	p	07:43	07:55
20-Apr-98	12:53	−35.82	89.10	−20.48	80.78	17	− − −	06:51	10:07
27-Apr-98	10:21	−21.35	−49.82	−13.91	−54.02	8	p	08:43	08:56
29-Apr-98	17:35	−17.71	−17.22	−13.21	−24.45	8	p	04:59	16:58
06-May-98	11:01	−21.59	72.76	−12.02	71.67	10	p	16:27	09:32
19-May-98	11:56	18.61	45.39	29.10	35.93	13	n	06:11	10:27
27-May-98	15:48	14.80	66.29	22.96	63.56	9	p	08:09	07:04
01-Jun-98	08:02	−20.81	−7.90	−36.61	−27.60	23	n	17:00	05:26
02-Jun-98	13:39	−43.73	77.85	−57.92	66.51	16	− − −	03:56	08:08
05-Jun-98	05:15	−32.01	27.05	−53.80	−6.57	32	n	06:18	01:30
05-Jun-98	08:14	−22.40	26.05	−35.74	5.26	22	p	06:48	07:02
18-Jun-98	05:20	−25.95	40.39	−44.09	24.52	22	p	02:56	01:27
02-Nov-98	14:50	−36.31	−42.83	−30.49	−42.84	6	− − −	03:25	13:54

Table 1 - *Continued*

Date	*Time* (*UT*)	b_1 (deg)	l_1 (deg)	b_2 (deg)	l_2 (deg)	*L* (deg)	*Polarity* *to*W*ofNL*	*lifetime* (*hrs*)	$T_{LASCO/C2}$ (*UT*)
04-Nov-98	11:48	21.72	6.54	30.33	−2.19	12	*p*	09:13	04:54
05-Nov-98	21:26	24.47	24.00	22.22	17.02	7	*p*	06:42	20:58
06-Nov-98	05:24	−18.89	14.93	−36.72	7.38	19	*n*	06:00	04:18
08-Nov-98	11:48	−19.41	37.91	−24.78	34.94	6	*p*	08:03	11:54
09-Nov-98	19:48	16.81	3.95	19.95	−2.81	7	*n*	03:37	17:54
23-Nov-98	11:54	−29.05	−66.94	−21.27	−60.34	10	*p*	04:25	NA
17-Dec-98	06:00	30.68	−1.79	26.47	−17.45	14	− − −	07:12	− − − DF
18-Dec-98	18:51	23.72	−35.49	33.73	−37.41	10	*p*	04:22	18:21
21-Mar-99	18:48	−22.60	14.16	−36.44	1.89	17	*n*	07:00	15:26
23-Mar-99	22:09	−17.32	17.60	−25.38	7.96	12	− − −	07:34	− − − DF
04-Apr-99	05:48	12.20	−55.01	13.95	−79.20	24	*p*	07:00	04:30
13-Apr-99	03:24	17.87	2.41	24.37	−8.01	12	*p*	06:00	03:30
17-Apr-99	08:22	−24.99	4.23	−34.24	−5.11	12	*n*	08:09	06:36
17-Apr-99	19:36	−28.03	17.20	−37.32	5.31	14	*p*	04:23	19:31
18-Apr-99	11:36	7.56	13.67	25.69	− 3.83	25	*p*	10:00	08:30
25-Apr-99	03:36	−17.44	27.19	−22.51	18.19	10	*n*	07:01	02:06
03-May-99	06:24	24.56	−40.86	15.49	−45.15	10	*p*	03:36	06:06
10-May-99	05:48	14.52	−15.20	44.23	−86.84	11	*p*	08:00	11:26
22-Jun-99	18:48	21.93	−36.79	28.44	−42.05	8	*p*	02:00	18:54
23-Jun-99	07:36	28.18	−41.44	18.50	−44.20	10	*n*	03:59	07:31
24-Jun-99[2]	14:36	26.88	14.97	36.81	1.94	15	*p*	08:24	13:31
07-Jul-99	23:36	14.13	62.66	31.63	39.28	28	*n*	12:37	19:31
19-Jul-99	02:36	15.42	16.75	11.95	13.21	5	*p*	01:36	03:06
23-Jul-99	20:48	20.41	−4.97	21.09	−13.43	8	− − −	03:00	19:31
25-Jul-99	15:36	32.83	76.28	46.40	75.09	14	*p*	09:11	13:31
25-Jul-99	22:36	23.81	60.22	39.00	45.60	20	− − −	02:24	21:30

Table 1 - *Continued*

Date	*Time* (UT)	b_1 (deg)	l_1 (deg)	b_2 (deg)	l_2 (deg)	L (deg)	*Polarity* $to\mathrm{W}ofNL$	*lifetime* (hrs)	$T_{LASCO/C2}$ (UT)
17-Aug-99	18:24	26.34	−38.15	18.14	−39.22	8	− − −	04:00	13:31
27-Aug-99	16:36	−26.84	3.54	−36.77	−12.34	17	p	03:49	17:06
28-Aug-99	21:24	−28.71	19.28	−36.30	5.27	14	− − −	04:00	10:26
30-Aug-99	18:36	18.06	18.58	24.66	11.54	9	p	02:00	18:50
09-Sep-99	18:17	10.96	−35.08	15.32	−39.33	6	p	02:31	− − − DF
09-Sep-99	20:12	20.72	50.21	27.20	46.47	7	p	02:12	19:52
12-Sep-99	03:24	−6.25	50.34	−23.62	32.33	25	p	05:36	00:54
15-Sep-99	15:12	9.96	−46.77	14.57	−55.55	10	p	08:12	14:30
16-Sep-99	18:48	28.84	35.03	53.45	11.69	30	− − −	03:11	06:54
20-Sep-99	08:48	−20.50	8.63	−29.50	−4.41	15	n	10:12	06:06
22-Sep-99	14:00	14.46	−37.73	19.57	−42.50	7	p	02:00	13:54
23-Sep-99	17:12	−11.47	46.69	−24.97	23.16	26	n	05:24	15:54
13-Oct-99	12:36	33.7	17.81	51.59	−33.84	35	n	05:36	09:50
21-Oct-99	04:24	−14.42	7.88	−16.00	1.58	6	p	04:24	− − −
25-Oct-99	18:00	−29.57	30.72	−50.30	−4.16	33	n	09:12	14:26
12-Nov-99	09:48	7.55	−8.47	12.34	−22.47	15	n	07:36	− − − DF
16-Nov-99	06:36	7.80	39.23	12.96	32.32	9	p	05:36	05:30
09-Dec-99	18:31	17.84	43.63	25.11	31.97	13	− − −	05:01	NA
22-Dec-99	03:00	41.59	−30.37	29.32	−30.12	12	− − −	08:24	02:30
02-Jan-00	05:24	14.46	−0.77	14.10	−9.33	8	p	01:34	− − −
04-Jan-00	05:00	25.75	52.52	29.34	45.61	7	p	03:14	03:30
18-Jan-00	19:13	−17.21	−0.97	−24.41	−16.11	16	p	06:36	17:54
28-Jan-00	20:48	−33.90	22.09	−26.97	14.65	9	n	09:00	20:12
08-Feb-00	10:14	26.91	−18.69	17.94	−39.82	21	− − −	09:55	09:30
09-Feb-00	21:24	−12.01	42.80	−21.18	32.91	13	n	03:48	19:54
12-Feb-00	05:24	21.85	28.84	28.34	21.58	9	p	10:24	04:31

Table 1 - *Continued*

Date	*Time* (*UT*)	b_1 (deg)	l_1 (deg)	b_2 (deg)	l_2 (deg)	*L* (deg)	*Polarity toWofNL*	*lifetime* (*hrs*)	$T_{LASCO/C2}$ (*UT*)
17-Feb-00	19:36	−21.77	20.78	−24.00	12.92	8	*n*	00:59	− − − DF
17-Feb-00	21:12	−32.25	−5.81	−26.08	−8.86	6	*n*	08:00	20:06
18-Feb-00	06:00	−7.95	−10.35	−11.36	−10.45	3	*n*	05:00	− − − DF
27-Feb-00	01:13	23.31	−48.40	34.55	−55.67	12	*p*	04:11	23:54
04-Mar-00	19:13	−33.58	−38.18	−33.54	−55.03	14	*p*	02:36	18:54
05-Mar-00[2]	13:13	−4.39	13.42	−19.05	5.62	16	*n*	10:00	12:54
05-Mar-00 [1]	17:48	34.40	38.72	36.30	22.18	13	*p*	04:36	16:54
04-Apr-00	16:37	13.16	59.69	23.34	58.23	10	*n*	03:00	16:32
08-Apr-00	18:48	−15.57	82.55	−21.71	77.89	8	*n*	06:00	15:54
13-Apr-00	22:24	−19.63	45.71	−34.11	23.82	24	*n*	06:48	21:30
29-Apr-00[2]	6:36	−14.30	9.97	−21.89	−2.48	14	*n*	10:48	06:30
08-May-00	10:36	−22.64	13.48	−35.37	−4.65	20	*p*	09:24	06:50
17-May-00	20:00	−18.95	48.94	−31.31	40.32	15	*n*	05:00	16:50
31-May-00[2]	8:48	19.06	1.23	29.33	−6.68	13	*n*	11:24	08:06
02-Jun-00	11:48	14.48	−21.30	8.15	−21.65	6	*p*	02:48	10:30
02-Jun-00	19:48	22.07	−62.04	18.35	−62.99	4	*p*	00:24	20:30
05-Jun-00	03:36	−9.05	35.74	−15.89	26.73	11	*n*	10:12	04:06
06-Jun-00	17:36	16.58	−8.52	22.75	−15.32	9	*p*	07:36	15:54
08-Jun-00	18:48	−13.46	−38.79	−20.39	−46.84	10	*p*	04:12	− − − DF
27-Jun-00	12:12	8.44	79.47	29.15	57.81	29	*n*	05:36	09:05
27-Jun-00	13:48	−18.19	−48.48	−9.40	−52.58	10	*p*	03:47	13:31
28-Jun-00	20:24	14.18	84.88	27.27	75.65	16	*p*	02:36	19:31
06-Jul-00	14:00	13.89	−15.61	16.45	−31.43	15	*p*	10:23	12:50
07-Jul-00	15:36	8.66	5.91	18.93	5.75	10	*n*	08:12	10:26
14-Jul-00	11:36	17.61	5.30	20.42	−6.22	11	*p*	12:00	10:54
17-Jul-00	12:00	−15.35	−33.58	−2.33	−27.12	14	*n*	13:10	08:54

Table 1 - *Continued*

Date	*Time* (UT)	b_1 (deg)	l_1 (deg)	b_2 (deg)	l_2 (deg)	L (deg)	*Polarity* toW$ofNL$	*lifetime* (hrs)	$T_{LASCO/C2}$ (UT)
17-Jul-00	15:12	7.00	11.95	−1.51	2.54	13	p	04:59	− − −
19-Jul-00	08:57	−13.00	−4.38	−24.67	−17.80	17	n	14:56	NA
23-Jul-00	06:12	−8.68	9.86	−13.45	2.39	9	n	13:48	05:30
28-Jul-00	22:12	20.13	−60.79	25.36	−67.18	8	n	04:12	21:08
03-Aug-00	09:36	16.71	77.17	31.81	65.20	19	n	02:11	08:30
07-Aug-00	23:12	−11.52	−18.13	−21.29	−29.20	14	p	03:24	23:30
12-Aug-00	17:00	8.15	52.09	16.91	43.54	12	p	07:00	15:54
13-Aug-00	03:36	−17.17	55.99	−29.71	43.02	17	n	04:48	03:30
04-Sep-00[2]	8:12	33.27	34.26	15.89	31.16	18	n	05:36	06:06
05-Sep-00	06:36	21.99	−7.08	16.12	−17.10	11	n	12:00	05:54
06-Sep-00	17:00	−16.23	19.79	−34.31	11.93	19	n	07:48	16:30
12-Sep-00[2]	13:48	−12.21	14.71	−25.71	−2.56	21	n	10:36	11:54
16-Sep-00	05:12	13.64	8.72	14.11	1.19	7	p	01:49	05:18
27-Sep-00	21:48	−19.90	−11.47	−28.32	−22.30	13	n	02:00	20:50
02-Oct-00	17:36	8.57	73.17	25.04	51.73	26	p	06:00	16:06
08-Oct-00	20:24	25.14	−32.88	31.51	−49.67	16	n	03:00	− − − DF
10-Oct-00	00:24	2.07	17.84	−1.93	9.97	8	p	05:48	23:50
22-Oct-00	13:25	−10.69	−76.51	−19.13	−82.05	10	− − −	16:01	00:50
25-Oct-00	13:13	4.07	60.04	14.39	47.31	16	p	11:24	08:26
29-Oct-00	03:22	−17.53	−33.76	−25.58	−43.07	11	n	08:38	NA
01-Nov-00	17:36	−12.37	−27.87	−15.48	−36.19	9	p	03:24	14:50
02-Nov-00	19:36	19.49	65.38	30.40	46.84	20	p	05:48	16:26
04-Nov-00	04:03	−24.83	67.74	−39.20	46.50	23	p	08:48	01:50
16-Nov-00	01:48	−29.46	−36.14	−19.34	−34.15	10	n	03:36	23:54
17-Nov-00	07:26	−43.35	35.47	−51.70	11.66	18	p	01:12	06:30
17-Nov-00	12:12	−23.34	−12.86	−25.11	−19.12	6	p	02:00	10:30

Table 1 - *Continued*

Date	*Time* (*UT*)	b_1 (deg)	l_1 (deg)	b_2 (deg)	l_2 (deg)	L (deg)	*Polarity* *to*W*ofNL*	*lifetime* (*hrs*)	$T_{LASCO/C2}$ (*UT*)
20-Nov-00	01:13	−15.89	22.79	−28.31	5.27	20	*n*	04:36	− − − DF
26-Nov-00	05:24	−19.98	54.32	−29.84	43.67	14	*n*	04:48	03:30
30-Nov-00	05:30	13.10	−5.40	26.83	−12.56	15	*p*	05:39	− − − DF
12-Dec-00	12:12	−25.72	2.73	−36.82	−21.28	23	*n*	08:48	09:50
18-Dec-00	12:24	12.81	4.43	18.60	−2.93	9	*p*	05:12	11:50
22-Dec-00	17:03	24.88	51.35	37.77	24.51	26	*n*	08:10	14:30
10-Jan-01	02:00	10.63	−33.53	18.74	−41.18	11	*n*	11:24	00:54
20-Jan-01	19:36	−10.05	−40.14	−1.06	−40.62	9	*n*	14:00	19:31
20-Jan-01	22:12	1.02	−44.37	−7.89	−49.97	11	*p*	10:24	21:30
02-Feb-01	21:12	19.45	−51.33	23.52	−59.34	8	*p*	08:48	19:54
10-Feb-01	11:36	18.92	24.67	26.05	−3.78	27	*p*	06:48	06:30
28-Feb-01	15:48	−15.81	9.02	−10.58	5.78	6	*p*	07:48	14:50
15-Mar-01	22:24	7.27	13.93	16.03	11.14	9	*n*	08:36	22:26
19-Mar-01	08:36	−15.17	18.40	−23.12	7.82	13	*p*	11:12	05:26
24-Mar-01	13:13	−39.54	20.26	−44.92	0.88	15	*n*	10:11	13:27
24-Mar-01	21:48	11.04	−13.16	19.87	−23.20	13	*p*	10:36	20:50
05-Apr-01	17:36	−17.26	−47.62	−26.43	−63.86	18	− − −	10:24	17:06
09-Apr-01	06:36	−18.02	−5.61	−30.45	−14.34	15	*n*	13:36	00:06
09-Apr-01	16:36	−23.84	7.55	−18.32	4.43	6	*p*	04:00	15:54
10-Apr-01	07:13	−17.48	6.03	−29.16	3.50	12	*n*	11:00	05:30
15-Apr-01	02:12	27.76	−10.01	44.29	−29.08	23	*n*	08:11	00:30
15-Apr-01	05:36	−17.55	0.00	−9.61	−14.94	17	*p*	11:38	− − − DF
15-Apr-01	16:56	18.35	−16.38	28.93	−17.81	11	*p*	03:44	− − − DF
23-Apr-01	13:39	−10.88	22.02	−16.16	15.26	8	*n*	05:26	12:39
26-Apr-01	10:00	23.38	42.84	34.59	28.22	17	*p*	04:00	08:30
26-Apr-01	14:36	20.92	10.34	26.09	4.28	8	*p*	03:59	12:30

Table 1 - *Continued*

Date	*Time* (UT)	b_1 (deg)	l_1 (deg)	b_2 (deg)	l_2 (deg)	L (deg)	*Polarity* toW$ofNL$	*lifetime* (hrs)	$T_{LASCO/C2}$ (UT)
10-May-01	04:24	19.59	80.55	27.62	63.75	17	p	10:48	04:30
15-May-01	22:36	32.37	−88.38	25.68	−88.77	7	p	03:36	18:52
18-May-01	07:48	−15.10	−54.42	−31.51	−76.61	26	p	08:48	04:50
21-May-01	12:00	32.72	−44.27	36.89	−57.57	12	p	06:00	09:26
24-May-01	21:36	12.84	−35.08	7.31	−35.37	6	p	01:36	20:26
04-Jun-01	02:24	27.16	34.55	38.13	26.82	13	p	06:23	00:54
15-Jun-01	11:36	−28.80	−37.92	−29.00	−53.12	13	p	09:03	10:31
20-Jul-01	05:36	14.10	38.56	25.04	20.23	20	n	07:00	05:06
31-Jul-01	09:11	−16.69	13.48	−30.37	−6.30	23	− − −	05:36	NA
31-Jul-01	12:55	−29.28	30.81	−35.81	−2.87	29	− − −	07:15	NA
14-Aug-01	16:17	15.56	28.47	28.23	14.65	18	p	10:23	16:01
21-Aug-01	14:25	−8.75	60.89	−25.41	42.81	24	n	04:00	12:06
25-Aug-01	18:36	−25.95	−34.20	−18.28	−37.11	8	p	04:36	16:50
11-Sep-01	15:48	7.56	−27.85	17.40	−31.84	11	p	07:01	14:54
17-Sep-01	05:48	−32.05	38.01	−47.41	11.71	25	p	04:12	04:54
24-Sep-01	11:48	−14.68	−21.07	−27.91	−32.51	17	n	06:36	10:30
28-Sep-01	09:36	13.85	−16.38	5.27	−20.01	9	n	07:00	08:54
09-Oct-01	12:12	−26.86	0.85	−31.21	−12.13	12	n	02:48	11:30
19-Oct-01	04:00	7.84	20.81	14.00	20.02	6	p	04:48	16:50
22-Oct-01	15:12	−15.95	−16.09	−23.11	−25.20	11	n	02:24	15:06
01-Nov-01	16:48	−18.32	−70.24	−23.97	−80.06	11	n	06:24	14:30
17-Nov-01	05:24	−6.05	−42.04	−9.34	−49.03	8	p	01:12	05:30
22-Nov-01	21:24	−21.76	68.28	−26.55	61.18	8	p	02:24	20:58
23-Nov-01	02:00	−10.94	30.20	−27.55	29.84	17	p	05:00	23:30
29-Nov-01	10:48	−1.97	−6.19	5.42	−13.14	10	n	05:00	− − − DF
20-Dec-01	04:36	−22.88	−32.76	−44.81	−62.61	33	n	16:24	00:30

Table 1 - *Continued*

Date	$Time$ (UT)	b_1 (deg)	l_1 (deg)	b_2 (deg)	l_2 (deg)	L (deg)	$Polarity$ toW$ofNL$	$lifetime$ (hrs)	$T_{LASCO/C2}$ (UT)
20-Dec-01	05:36	−29.93	34.07	−44.09	5.24	27	p	04:36	04:54
28-Dec-01	23:12	−35.24	−81.01	−20.27	−83.12	15	p	03:36	20:06
28-Jan-02	15:24	−25.66	−9.22	−39.48	−37.79	28	n	03:48	10:54
12-Feb-02	16:00	10.19	−35.12	10.09	−44.07	9	p	05:48	15:06
02-Mar-02	19:41	−14.44	−72.87	−43.03	−84.16	30	p	07:24	15:30
10-Mar-02	12:36	−29.32	9.18	−32.68	−6.77	14	n	04:10	− − − DF
16-Mar-02	01:48	−0.87	13.03	−12.83	5.46	14	n	09:36	23:06
18-Mar-02	05:00	−15.53	26.60	−2.02	21.83	14	p	10:48	02:54
15-Apr-02	07:25	−12.83	9.08	−18.34	2.82	8	n	05:24	04:06
21-Apr-02	03:36	−8.57	85.04	−19.34	75.01	14	n	14:37	01:27
08-May-02	14:24	−14.62	8.40	−10.72	7.08	4	n	02:00	14:06
21-May-02	22:12	15.77	−37.10	23.80	−43.32	10	p	01:48	21:50
22-May-02	03:00	−14.47	77.44	−26.16	72.06	12	p	10:48	00:06
22-May-02	05:36	−12.25	58.93	−29.93	45.78	21	n	06:00	03:50
27-May-02	15:48	20.22	−13.32	29.32	−19.94	11	p	04:11	13:27
02-Jun-02	22:50	−33.97	−50.79	−28.53	−53.94	6	n	03:58	NA
30-Jun-02	20:00	−10.88	−72.32	−20.75	−83.38	15	− − −	09:00	09:30
07-Jul-02	20:00	12.11	77.91	19.56	43.69	34	p	04:35	18:06
15-Jul-02	22:00	22.15	−2.93	33.15	−5.11	11	p	02:24	20:30
23-Jul-02	23:36	4.26	70.24	30.83	36.51	41	p	10:00	20:30
01-Aug-02	09:36	−10.34	−0.65	−25.78	−11.01	18	n	10:00	04:06
06-Aug-02	19:13	−52.92	31.61	−34.95	14.10	22	p	06:00	18:25
13-Aug-02	10:14	16.62	−51.29	37.77	−68.75	26	p	05:12	08:54
14-Aug-02	04:48	3.68	62.60	14.01	55.28	13	n	01:48	02:30
16-Aug-02	14:24	−6.09	−17.16	−25.91	−21.29	20	n	09:00	12:30
21-Aug-02	02:00	42.69	9.52	50.43	−14.58	18	p	04:00	01:31

Table 1 - *Continued*

$Date$	$Time$ (UT)	b_1 (deg)	l_1 (deg)	b_2 (deg)	l_2 (deg)	L (deg)	$Polarity$ toW$of NL$	$lifetime$ (hrs)	$T_{LASCO/C2}$ (UT)
05-Sep-02	18:00	12.32	−23.97	−0.78	−31.21	15	n	03:59	17:06
15-Sep-02	23:48	27.32	−38.68	36.59	−91.36	45	n	07:00	21:30
17-Sep-02	08:36	−7.71	37.98	−20.11	32.97	13	p	11:00	08:06
17-Sep-02	20:24	19.68	22.29	13.78	17.79	7	p	09:36	15:54
22-Sep-02	11:36	21.99	−4.07	17.42	−8.27	6	p	00:48	11:30
15-Oct-02	15:48	10.77	11.85	27.97	3.53	19	n	03:23	14:31
20-Oct-02	22:24	−7.50	11.08	−18.63	−5.27	19	p	02:36	20:30
25-Oct-02	19:13	23.88	17.29	36.52	0.00	19	p	− − −	18:06
30-Oct-02	05:36	−5.22	45.57	−14.90	34.18	15	n	09:11	00:50
04-Nov-02	13:25	−8.08	−20.85	4.25	−27.53	14	n	12:12	11:06
09-Nov-02	13:25	−8.14	29.14	−17.43	26.27	9	− − −	02:35	13:31
10-Nov-02	04:24	−8.86	38.25	−18.77	34.48	10	− − −	02:48	03:30
19-Nov-02	07:36	27.08	−25.91	41.15	−72.43	40	p	17:36	03:50
24-Nov-02	22:24	4.96	−29.18	31.07	−47.39	31	n	13:48	20:30
13-Dec-02	14:12	−8.36	5.31	−18.14	−16.45	23	n	08:11	13:31
13-Dec-02	20:00	17.89	−10.10	29.42	−14.31	12	p	12:12	20:06
14-Dec-02	20:24	−17.27	−23.58	−7.46	−28.53	11	p	02:47	19:31
17-Dec-02	17:00	−24.19	20.72	−26.97	−5.54	24	p	05:24	14:30
19-Dec-02	22:36	11.68	9.48	25.82	8.59	14	n	03:48	22:06
21-Dec-02	05:48	31.32	16.08	46.01	−28.19	37	p	13:24	02:30

---

[1] This event was selected for detailed study of the dynamics of different associated features described in Chapter 8.

[2] Events were selected for detailed study of magnetic field evolution in the source region described in Chapter 9.

B Magnetic Reconnection

Magnetic reconnection is a phenomenon which is of particular importance in solar system plasma. In the solar corona, it results in the rapid release of the energy stored in the large-scale structure of the coronal magnetic field, an effect which is thought to give rise to solar eruptions among processes (e.g., Lin & Forbes 2002). Small scale reconnection may play a role in heating the corona, and thereby, driving the outflow of the solar wind.

The evolution of the magnetic field in a resistive Magnetohydrodynamics (MHD) plasma is given by the induction equation:

$$\frac{\partial \mathbf{B}}{\partial t} = \bigtriangledown \times (\mathbf{V} \times \mathbf{B}) + \eta \bigtriangledown^2 \mathbf{B}$$

where $\eta = \frac{c^2}{4\pi\sigma}$ is called magnetic diffusivity or resistivity and σ is the electric conductivity. While obtaining this equation the electrical conductivity is assumed to be spatially constant and hence taken outside the spatial derivative.

The first term on the right-hand side of the equation describes the advection of the magnetic field with the plasma flow. The second term describes the resistive diffusion of the field through the plasma. If the first term dominates then magnetic flux is frozen into the plasma, and the topology of the magnetic field cannot change or it changes in the topology equivalent to the pre-existing one. Therefore for this case cutting and pasting of the magnetic field lines is not possible. On the other hand, if the second term dominates then there is little coupling between the field and the plasma flow, and the topology of the magnetic field is free to change into any kind of topology.

For solar plasma due to high electrical conductivity the first term becomes very important and as a very crude MHD approximation the induction equation takes the form:

$$\frac{\partial \mathbf{B}}{\partial t} = \bigtriangledown \times (\mathbf{V} \times \mathbf{B})$$

and the magnetic fields are frozen into the plasma i.e. if two fluid elements lie on a magnetic field line, then they would always lie on the same magnetic field.

However, if there exits a small electrical resistivity, its effect can become important in a layer where the magnetic field gradient is large. Since large gradients of magnetic field are associated with large current densities, such regions are often called *current sheet*. Thus, in low-resistive plasma cutting and pasting of field lines can take place within the current sheet but the magnetic field may be taken to be frozen in the plasma outside the current sheet and the magnetic topologies are preserved everywhere except in the current sheet.

Therefore in regions such as current sheet, the large value of $\bigtriangledown^2\mathbf{B}$ would make the electrical resistivity term important and hence the magnetic field would decay away. Since the magnetic field has associated pressure $B^2/8\pi$, a decrease in the magnetic field would cause a pressure decrease in the region near the current sheet. Since in the solar corona plasma-β is less than one, the decay of the magnetic field near the current sheet region would cause an appreciable depletion of the total pressure. Therefore, plasma on both sides of the current sheet with fresh magnetic field would be pulled to the current sheet. This fresh magnetic field would then decay and more plasma from above and below would be pulled in to compensate for the pressure decrease due to this decay. This process may go on as long as fresh magnetic fields are brought in to current sheet region. An extensive description of magnetic reconnection process can be found in Choudhuri (1998) and Forbes & Priest (2000).

Bibliography

Alfv́en, H. 1942, Existence of electromagnetic-hydrodynamic waves, Nature, 150, 405

Allen, C. W., 1947, Interpretation of Electron Density from Corona Brightness, Mon. Not. Roy. Astron. Soc., 107, 426

Amari, T.; Luciani, J. F.; Aly, J. J.; Tagger, M., 1996, Very Fast Opening of a Three-dimensional Twisted Magnetic Flux Tube, Astrophysical Journal, 466, 39

Antiochos, S. K., 1998, The Magnetic Topology of Solar Eruptions, Astrophysical Journal, 502, 181

Antiochos, S. K.; Devore, C. R.; Klimchuk, J. A., 1999, A Model for Solar Coronal Mass Ejections, Astrophysical Journal, 510, 485

Asai, A.; Yokoyama, T.; Shimojo, M.; Shibata, K., 2004, Downflow Motions Associated with Impulsive Nonthermal Emissions Observed in the 2002 July 23 Solar Flare, Astrophysical Journal, 605, L77

Aschwanden, M. J., 2004, Physics of The Solar Corona: An Introduction, Springer-Verlag

Babcock, H. W., 1961, The Topology of the Sun's Magnetic Field and the 22-YEAR Cycle, Astrophysical Journal, 133, 572

Benevolenskaya, E. E., Hoeksema, J. T., Kosovichev, A. G., Scherrer, P. H., 1999, The Interaction of New and Old Magnetic Fluxes at the Beginning of Solar Cycle 23, Astrophysical Journal, 517, L163

Benevolenskaya, E. E., Kosovichev, A. G., Lemen, J. R., Scherrer, P. H., Slater, G. L., 2002, Large-Scale Solar Coronal Structures in Soft X-Rays and Their Relationship to the Magnetic Flux, Astrophysical Journal, 571, L181

Biesecker, D. A.; Myers, D. C.; Thompson, B. J.; Hammer, D. M.; Vourlidas, A., 2002, Solar Phenomena Associated with ”EIT Waves”, Astrophysical Journal, 569, 1009

Bothmer, V., 2003, Sources of magnetic helicity over the solar cycle, in Proc. ISCS 2003 Symposium, Solar Variability as an Input to the Earth's Environment, ed. A. Wilson (Noordwijk: ESA), 419

Bothmer, V. and Rust, D. M., 1997, The Field Configuration of Magnetic Clouds and the Solar Cycle, in Coronal Mass Ejections, ed. N. Crooker, J. A. Joselyn & J. Feynman Washington, DC, AGU, 139

Bothmer, V. and Schwenn, R., 1994, Eruptive prominences as sources of magnetic clouds in the solar wind, Space Science Reviews, 70, 215

Bothmer, V. and Schwenn, R., 1998, The structure and origin of magnetic clouds in the solar wind, Annales Geophysicae, 16, 1

Brueckner, G. E.; Howard, R. A.; Koomen, M. J. et al., 1995, The large angle spectrometric coronagraph (LASCO), Solar Physics, 162, 357

Brueckner, G. E.; Delaboudiniere, J.-P.; Howard, R. A. et al., 1998, Geomagnetic storms caused by coronal mass ejections (CMEs): March 1996 through June 1997, Geophysical Research Letters, 25, 3019

Burkepile, J. T. and St. Cyr, O. C., 1993, A revised and expanded catalogue of mass ejections observed by the Solar Maximum Mission coronagraph, NCAR/TN-369+ST, Boulder, 9326556B

Canfield, R. C.; Hudson, H. S.; McKenzie, D. E., 1999, Sigmoidal morphology and eruptive solar activity, Geophysical Research Letter, 26, 627

Cargill, P. J.; Priest, E. R., 1983, The heating of postflare loops, Astrophysical Journal, 266, 383

Carrington, R. C., 1859, Description of a Singular Appearance seen in the Sun on September 1, 1859, Mon. Not. Roy. Astron. Soc., 20, 13

Carrington, R. C., 1863, On the Motion of the Solar System in Space, Mon. Not. Roy. Astron. Soc., 23, 203

Chen, J.; Howard, R. A.; Brueckner, G. E. et al., 1997, Evidence of an Erupting Magnetic Flux Rope: LASCO Coronal Mass Ejection of 1997 April 13, Astrophysical Journal Letters, 490, 191

Chen, P. F. and Shibata, K., 2000, An Emerging Flux Trigger Mechanism for Coronal Mass Ejections, Astrophysical Journal, 545, 524

Choudhuri, A. R., 1998, The Physics of Fluids and Plasmas : An Introduction for Astrophysicists, Cambridge University Press

Cliver, E. W.; St. Cyr, O. C.; Howard, R. A.; McIntosh, P. S., 1994, Rotation-Averaged Rates of Coronal Mass Ejections and Dynamics of Polar Crown Filaments, in Solar Coronal Structure, ed. V. Rusin, P. Heinzel and J. -C. Vial, VEDA Publishing Co. Bratislava, 83

Cremades, H. and Bothmer, V., 2004, On the three-dimensional configuration of coronal mass ejections, Astronomy and Astrophysics, 422, 307.

Daglis, I. A., 2004, Effects of Space weather on technology infrastructure, Nato Science Series, II Mathematics, Physics and Chemistry, Kluwer Academic Publishers

Delaboudinière J. P.; Artzner, G. E.; Brunaud, J. et al. 1995, EIT: Extreme-Ultraviolet Imaging Telescope for the SoHO Mission, Solar Physics, 162, 291

Delannée, C.; Delaboudinière, J.-P.; Lamy, P., 2000, Observation of the origin of CMEs in the low corona, Astronomy and Astrophysics, 355, 725

Dere, K. P.; Brueckner, G. E.; Howard, R. A.; Michels, D. J.; Delaboudiniere, J. P., 1999, LASCO and EIT Observations of Helical Structure in Coronal Mass Ejections, Astrophysical Journal, 516, 465

Dere, K. P.; Moses, J. D.; Delaboudinière, J.-P. et al., 2000, The Preflight Photometric Calibration of the Extreme-Ultraviolet Imaging Telescope EIT, Solar Physics, 195, 13

Domingo, V.; Fleck, B.; Poland, A. I., 1995, The SoHO mission: An overview, solar Physics, 162, 1

Dryer, M., 1982, Coronal transient phenomena, Space Science Reviews, 33, 233

Dryer, M., 1996, Comments on the Origins of Coronal Mass Ejections, Solar Physics, 169, 421

Feynman, J.; Martin, S. F., 1995, The initiation of coronal mass ejections by newly emerging magnetic flux, Journal of Geophysical Research, 100, 3355

Fisher, George H.; Longcope, Dana W.; Metcalf, Thomas R.; Pevtsov, Alexei A., 1998, Coronal Heating in Active Regions as a Function of Global Magnetic Variables, Astrophysical Journal, 508, 885

Fligge, M. and Solanki, S. K., 1997, Noise reduction in astronomical spectra using wavelet packets, Astronomy and Astrophysics, 124, 579

Forbes, T. G., 1991, Magnetic reconnection in solar flares, Geophysical and Astrophysical Fluid Dynamics, 62, 16

Forbes, T. G., 2000, A review on the genesis of coronal mass ejections, Journal of Geophysical Research, 105, 23153

Forbes, T. G. and Isenberg, P. A., 1991, A catastrophe mechanism for coronal mass ejections, Astrophysical Journal, 373, 294

Forbes, T. G.; Malherbe, J. M., 1986, A shock condensation mechanism for loop prominences, Astrophysical Journal, 302, 67

Forbes, T. G. and Priest, E. R., 1998, Magnetic Reconnection: MHD Theory and Applications, Cambridge University Press

Gibson, S. E. and Low, B. C., 2000, Three-dimensional and twisted: An MHD interpretation of on-disk observational characteristics of coronal mass ejections, Journal of Geophysical Research, 105, 18187.

Gopalswamy, N.; Lara, A.; Yashiro, S.; Nunes, S.; Howard, R. A., 2003, Coronal mass ejection activity during solar cycle 23, ISCS 2003 Symposium, 'Solar variability as an input to the Earth's Environment', Tatranská Lomnica, Slovakia, 23-28 June 2003, 403.

Gosling, J. T., 1993, Coronal mass ejections: the link between solar and geomagnetic storms, Physics of fluids B 5, 7, 2638

Gosling, J. T., 1993, The solar flare myth, Journal of Geophysical Research, 98, 18937.

Gosling, J. T.; Hildner, E.; MacQueen, R. M.; Munro, R. H.; Poland, A. I.; Ross, C. L., 1976, The speeds of coronal mass ejection events, Solar Physics, 48, 389.

Hagenaar, H. J.; Schrijver, C. J.; Title, A. M., 2003, The Properties of Small Magnetic Regions on the Solar Surface and the Implications for the Solar Dynamo(s), Astrophysical Journal, 584, 1107

Hale, George E.; Ellerman, Ferdinand; Nicholson, S. B.; Joy, A. H., 1919, The Magnetic Polarity of Sun-Spots, Astrophysical Journal, 49, 153

Handy, B. N.; Acton, L. W.; Kankelborg, C. C., 1999, The transition region and coronal explorer, Solar Physics, 187, 229

Harra, L. K., 2004, The Physics of the Sun, Eddited by Harra, L. K. and Mason, K. O., Imperial College Press

Harra, L. K.; Sterling, A. C., 2001, Material Outflows from Coronal Intensity Dimming Regions during Coronal Mass Ejection Onset, Astrophysical Journal, 561, 215

Harrison, R. A., 1986, Solar coronal mass ejections and flares, Astronomy and Astrophysics, 162, 283

Harrison, R. A., 1995, The nature of solar flares associated with coronal mass ejection, Astronomy and Astrophysics, 304, 585.

Heyvaerts, J.; Priest, E. R.; Rust, D. M., 1977, An emerging flux model for the solar flare phenomenon, Astrophysical Journal, 216, 123

Hildner, E.; Gosling, J. T.; MacQueen, R. M.; Munro, R. H.; Poland, A. I.; Ross, C. L., 1976, Frequency of coronal transients and solar activity, Solar Physics, 48, 127.

Howard, R. A.; Michels, D. J.; Sheeley, N. R., Jr.; Koomen, M. J., 1982, The observation of a coronal transient directed at earth, Astrophysical Journal, 263, L101.

Howard, R. A.; Sheeley, N. R., Jr.; Michels, D. J.; Koomen, M. J., 1984, The statistical properties of coronal mass ejections during 1979-1981, Advances in Space Research, 4, 307

Howard, R. A.; Sheeley, N. R., Jr.; Michels, D. J.; Koomen, M. J., 1985, Coronal mass ejections - 1979-1981, Journal of Geophysical Research, 90, 8173.

Howard, R. A.; Sheeley, N. R., Jr.; Michels, D. J.; Koomen, M. J., 1986, The solar cycle dependence of coronal mass ejections, The sun and the heliosphere in three dimensions; Proceedings of the Nineteenth ESLAB Symposium, Les Diablerets, Switzerland, 1985, Dordrecht, D. Reidel Publishing Co., 107

Howard, R. A.; Brueckner, G. E.; St. Cyr, O. C. et al., 1997, Observations of CMEs from SoHO/LASCO, Coronal Mass Ejections, Geophysical Monograph 99, AGU, 17

Hudson, H. S.; Lemen, J. R.; St. Cyr, O. C.; Sterling, A. C.; Webb, D. F., 1998, X-ray coronal changes during halo CMEs, Geophysical Research Letters, 25, 2481.

Hundhausen, A. J., 1993, Sizes and locations of coronal mass ejections - SMM observations from 1980 and 1984-1989, Journal of Geophysical Research, 98, 13177.

Hundhausen, A. J., 1999, Coronal Mass Ejections, in The many faces of the Sun edited by K. T. Strong, J. L. R. Saba, B. M. Haisch, J. T. Schmelz, Springer-Verlag, 143

Hundhausen, A. J.; Sawyer, C. B.; House, L.; Illing, R. M. E.; Wagner, W. J., 1984, Coronal mass ejections observed during the solar maximum mission - Latitude distribution and rate of occurrence, Journal of Geophysical Research, 89, 2639.

Hundhausen, A. J.; Burkepile, J. T.; St. Cyr, O. C., 1994, Speeds of coronal mass ejections: SMM observations from 1980 and 1984-1989, Journal of Geophysical Research, 99, 6543

Innes, D. E.; McKenzie, D. E.; Wang, Tongjiang, 2003, SUMER spectral observations of post-flare supra-arcade inflows, Solar Physics, 217, 247

Innes, D. E.; McKenzie, D. E.; Wang, Tongjiang, 2003, Observations of 1000 km/s Doppler shifts in 107 K solar flare supra-arcade, Solar Physics, 217, 267

Isenberg, P. A.; Forbes, T. G.; Demoulin, P., 1993, Catastrophic Evolution of a Force-free Flux Rope: A Model for Eruptive Flares, Astrophysical Journal, 417, 3681

Kahler, S., 1977, The morphological and statistical properties of solar X-ray events with long decay times, Astrophysical Journal, 214, 891

Kahler, S. W., 1992, Solar flares and coronal mass ejections, Annual Review of Astronomy and Astrophysics, 30, 113

Kopp, R. A.; Pneuman, G. W., 1976, Magnetic reconnection in the corona and the loop prominence phenomenon, Solar Physics, 50, 85

Klimchuk, J., 2001, Theory of Coronal Mass Ejections, Proc-2001-Song., 143

Krall, J.; Chen, J.; Santoro, R., 2000, Drive Mechanisms of Erupting Solar Magnetic Flux Ropes, Astrophysical Journal, 539, 964

Lang, K. R., 2001, The Cambridge Encyclopedia Of The Sun, Cambridge University Press

Li, Ke-Jun, Xiao-Hua, Yun, Hong-Sik et al. 2002, Asymmetrical distribution of sunspot groups in the solar hemispheres, Astronomical Society of Japan, 54, 629

Lin, J.; Forbes, T. G., 2000, Effects of reconnection on the coronal mass ejection process, Journal of Geophysical Research, 105, 2375

Lin, J.; Forbes, T. G.; Isenberg, P. A., 2001, Prominence eruptions and coronal mass ejections triggered by newly emerging flux, Journal of Geophysical Research, 106, 25053.

Linker, J.; Mikič, Z.; Lionello, R. et al. 2003, Flux cancellation and coronal mass ejections, Physics of Plasmas, 10, 2003

Low, B. C., 1996, Solar Activity and the Corona, Solar Physics, 167, 217

Low , B. C., 1999, Coronal Mass Ejections, Flares, and Prominences, Solar Wind Nine, Proceedings of the Ninth International Solar Wind Conference, Nantucket, MA, October 1998. Edited by Shaddia Rifai Habbal, Ruth Esser, Joseph V. Hollweg, and Philip A. Isenberg. AIP Conference Proceedings, 471, 109

Low, B. C., 2001, Coronal mass ejections, magnetic flux ropes, and solar magnetism, Journal of Geophysical Research, 106, 25141

Martin, S. F.; Harvey, K. H., 1979, Ephemeral active regions during solar minimum, Solar Physics, 64, 93

MacQueen, R. M.; Eddy, J. A.; Gosling, J. T. et. al., 1974, The Outer Solar Corona as Observed from Skylab: Preliminary Results, Astrophysical Journal, 187, L85

MacQueen, R. M.; Csoeke-Poeckh, A.; Hildner, E. et al., 1980, The High Altitude Observatory Coronagraph/Polarimeter on the Solar Maximum Mission, Solar Physics, 65, 91.

McKenzie, D. E., 2000, Supra-arcade Downflows in Long-Duration Solar Flare Events, Solar Physics, 195, 381

McKenzie, D. E.; Hudson, H. S., 1999, X-Ray Observations of Motions and Structure above a Solar Flare Arcade, Astrophysical Journal, 519, 93

Martin, S. F.; Dezso, L.; Antalova, A.; Kucera, A.; Harvey, K. L., 1982, Emerging magnetic flux, flares and filaments - FBS interval 16-23 June 1980, Advances in Space Research, 2, 39

Martin, S. F.; Bentley, R. D.; Schadee, A. et al., 1984, Relationships of a growing magnetic flux region to flares, Advances in Space Research, 4, 61

Michels, D. J.; Howard, R. A.; Koomen, M. J.; Sheeley, N. R., Jr., 1980, Satellite observations of the outer corona near sunspot maximum, In: Radio physics of the sun; Proceedings of the Symposium, College Park, Md., August 7-10, 1979. D. Reidel Publishing Co., 439.

Mikic, Z.; Linker, A., 1994, Disruption of coronal magnetic field arcades, Astrophysical Journal, 430, 898

Mikic, Z.; Linker, A., 1999, Initiation of Coronal Mass Ejections by Changes in Photospheric Flux, American Astronomical Society, Bulletin of the American Astronomical Society, 31, 918

Moses, D.; Clette, F.; Delaboudiniere, J.-P. et al., 1997, EIT Observations of the Extreme Ultraviolet Sun, Solar Physics, 175, 571

Munro, R. H. and Sime, D. G., 1985, White-light coronal transients observed from SKYLAB May 1973 to February 1974 - A classification by apparent morphology, Solar Physics 97, 191.

Munro, R. H.; Gosling, J. T.; Hildner, E.; MacQueen, R. M.; Poland, A. I.; Ross, C. L., 1979, The association of coronal mass ejection transients with other forms of solar activity, Solar Physics, 61, 201.

Nitta, N., 2000, The relation between hot and cool loops, Solar Physics, 195, 123

Plunkett, S. P.; Thompson, B. J.; Howard, R. A. et al., 1998, LASCO observations of an Earth-directed coronal mass ejection on May 12, 1997, Geophysical Research Letters, 25, 2477

Pojoga, S. and Cudnik, B., 2002, The Clustering Properties of Active Regions During the First Part of Solar Cycle 23, Solar Physics, 208, 17

Rust, D. M., 1972, Flares and Changing Magnetic Fields, Solar Physics, 25, 141

Rust, D. M.; Kumar, A., 1996, Evidence for Helically Kinked Magnetic Flux Ropes in Solar Eruptions, Astrophysical Journal Letters, 464, L199.

Rust, D. M.; Webb, D. F., 1977, Soft X-ray observations of large-scale coronal active region brightenings, Solar Physics, 54, 403

Scherrer, P. H.; Bogart, R. S.; Bush, R. I., et al., 1995, The Solar Oscillations Investigation - Michelson Doppler Imager, Solar Physics, 162, 129

Schwenn, R., 1996, An Essay on Terminology, Myths and Known Facts: Solar Transient - Flare - CME - Driver Gas - Piston - BDE - Magnetic Cloud - Shock Wave - Geomagnetic Storm, Solar and Interplanetary Transients, proceedings of IAU Colloquium 154, held in Pune, India, January 23-27, 1995. ASTROPHYSICS AND SPACE SCIENCE I, edited by S. Ananthakrishnan; A. Pramesh Rao., 243, 187

Schwenn, R.; Inhester, B.; Plunkett, S. P., et al., 1997, First View of the Extended Green-Line Emission Corona At Solar Activity Minimum Using the LASCO-C1 Coronagraph on SoHO, Solar Physics, 175, 667

Sheeley, N. R., Jr.; Wang, Y.-M., 2002, Characteristics of Coronal Inflows, Astrophysical Journal, 59, 874

Sheeley, N. R., Jr.; Howard, R. A.; Koomen, M. J., et al., 1982, Observations of coronal structure during sunspot maximum, Space Science Reviews, 33, 219

Sheeley, N. R.; Walters, J. H.; Wang, Y.-M.; Howard, R. A., 1999, Continuous tracking of coronal outflows: Two kinds of coronal mass ejections, Journal of Geophysical Research, 104, 2439

Shensa, M. J., 1992, Discrete wavelet transforms: wedding the á trous and Mallat algorithm, Proceeding IEEEE Transactions on Signal Processing, 40, 2464

Smart, W. M., 1944, A text book of spherical astronomy, Cambridge University Press

St. Cyr, O. C.; Webb, D. F., 1991, Activity associated with coronal mass ejections at solar minimum - SMM observations from 1984-1986, Solar Physics, 136, 379

St. Cyr. O. C., Howard, R. A., Sheeley, N. R. Jr., 2000, Properties of coronal mass ejections: SoHO/LASCO observations from January 1996 to June 1998, Journal of Geophysical Research, 105, 18169

Starck, J, -L.; Siebenmorgen, R.; Gredel, R., 1997, Astrophysical Journal, 482, 1011

Stenborg, G. and Cobelli, P. J., 2003, A wavelet packets equalization technique to reveal the multiple spatial-scale nature of coronal structures, Astronomy and Astrophysics, 398, 1185

Sterling, A. C.; Hudson, H. S.; Thompson, B. J.; Zarro, D. M., 2000, Yohkoh SXT and SoHO EIT Observations of Sigmoid-to-Arcade Evolution of Structures Associated with Halo Coronal Mass Ejections, The Astrophysical Journal, 532, 628.

Subramanian, P.; Dere, K. P., 2001, Source Regions of Coronal Mass Ejections, Astrophysical Journal, 56, 372.

Ŝvestka, Z., K., 2003, Dynamic Sun, Edited by B. N. Dwivedi, Cambridge University Press, 238

Ŝvestka, Z., K.; Fárník, F.; Hudson, H. S.; Hick, P., 1998, Large-Scale Active Coronal Phenomena in Yohkoh SXT Images - IV. Solar Wind Streams from Flaring Active Regions, Solar Physics, 182, 179

Tandberg-Hanssen, E., 1974, Solar Prominences, D. Reidel Publishing Company

Thompson, B. J.; Plunkett, S. P.; Gurman, J. B., et al., 1998, SoHO/EIT observations of an Earth-directed coronal mass ejection on May 12, 1997, Geophysical Research Letters, 25, 2465

Thompson, B. J.; Gurman, J. B.; Neupert, W. M. et al., 1999, SoHO/EIT Observations of the 1997 April 7 Coronal Transient: Possible Evidence of Coronal Moreton Waves, Astrophysical Journal, 517, 151

Thompson, B. J.; Reynolds, B.; Aurass, H., et al., 2000, Observations of the 24 September 1997 Coronal Flare Waves, Solar Physics, 193, 161

Titov, V. S.; Démoulin, P., 1999, Basic topology of twisted magnetic configurations in solar flares, Astronomy and Astrophysics, 351, 707

Tousey, R.; Bartoe, J. D. F.; Bohlin, J. D., et al., 1973, A Preliminary Study of the Extreme Ultraviolet Spectroheliograms from Skylab, Solar Physics, 33, 265

Tousey, R.; Howard, R. A.; Koomen, M. J., 1974, The Frequency and Nature of Coronal Transient Events Observed by OSO-7, Bulletin of the American Astronomical Society, 6, 295.

Tousey, R.; Bartoe, J.-D. F.; Brueckner, G. E.; Purcell, J. D., 1977, Extreme ultraviolet spectroheliograph ATM experiment S082A, Applied Optics, 16, 870

Tripathi, D.; Bothmer, V.; Cremades, H., 2004, The basic characteristics of EUV post-eruptive arcades and their role as tracers of coronal mass ejection source regions, Astronomy and Astrophysics, 422, 337

Tsuneta, S.; Acton, L.; Bruner, M., et al., 1991, The soft X-ray telescope for the SOLAR-A mission, Solar Physics, 136, 37

Wang, Y. -M. and Sheeley, N. R. Jr., 1999, Filament Eruptions near Emerging Bipoles, Astrophysical Journal, 510, 157

Wang, Y.-M.; Sheeley, N. R.; Howard, R. A.; St. Cyr, O. C.; Simnett, G. M., 1999. Coronagraph observations of inflows during high solar activity, Geophysical Research Letters, 26, 1203

Wang, T. J.; Solanki, S. K.; Curdt, W., et al., 2003, Hot coronal loop oscillations observed with SUMER: Examples and statistics, Astronomy and Astrophysics, 406, 1105

Webb, D. F.; Howard, R. A., 1994, The solar cycle variation of coronal mass ejections and the solar wind mass flux, Journal of Geophysical Research, 99, 4201

Webb, D. F.; Hundhausen, A. J., 1987, Activity associated with the solar origin of coronal mass ejections, Solar Physics,108, 2, 383

Webb, D. F.; Jackson, B. V., 1981, Kinematical analysis of flare spray ejecta observed in the corona, Solar Physics, 73, 341

Webb, D. F.; Krieger, A. S.; Rust, D. M., 1976, Coronal X-ray enhancements associated with H-alpha filament disappearances, Solar Physics, 48, 159.

Wilhelm, K.; Curdt, W.; Marsch, E., et al., 1995, SUMER - Solar Ultraviolet Measurements of Emitted Radiation, Solar Physics, 162, 189

Wu, S. T., 1982, Numerical simulation of magnetohydrodynamic shock propagation in the corona, Space Science Reviews, 32, 115

Wu, S. T.; Guo, W. P.; Wang, J. F., 1995, Dynamical evolution of a coronal streamer-bubble system. 1: A self-consistent planar magnetohydrodynamic simulation, Solar Physics, 157, 325

Wu, S. T.; Wang, A. H.; Plunkett, S. P.; Michels, D. J., 2000, Evolution of Global-Scale Coronal Magnetic Field due to Magnetic Reconnection: The Formation of the Observed Blob Motion in the Coronal Streamer Belt, Astrophysical Journal, 545, 1101

Yashiro, S., Gopalswamy, N., Michalek, G. et al. 2002, Properties of coronal mass ejections observed by SoHO, American Geophysical Union, SH32A-03

Yurchyshyn, V. B.; Wang, H.; Goode, P. R.; Deng, Y., 2001, Orientation of the Magnetic Fields in Interplanetary Flux Ropes and Solar Filaments, Astrophysical Journal, 563, 381

Zhang, J.; Dere, K. P.; Howard, R. A.; Kundu, M. R.; White, S. M., 2001, On the Temporal Relationship between Coronal Mass Ejections and Flares, Astrophysical Journal, 559, 452

Zhukov, A. N.; Auchère, F., 2004, On the nature of EIT waves, EUV dimmings and their link to CMEs, Astronomy and Astrophysics, 427, 705

Acknowledgements

Successful completion of my Ph.D. thesis is a linear combination of the masterful guidance from my supervisors, support of the institute & my friends and continuing wishes from my parents and relatives.

Dr. Volker Bothmer, my supervisor at MPS now at Sternwarte Göttingen, deserves first-mention in a long list of people, not only because he was my principal supervisor and came up with a challenging and interesting problem, but also for his generous supervision throughout my thesis. Thanks a lot Volker!

Another person I frequently pestered throughout my stay at Max-Planck was Prof. Dr. Rainer Schwenn. But without the slightest of hesitation he answered all my queries and gave me invaluable ideas all through my research. Vielen Dank Rainer!

I would like to thank Prof. Dr. Franz Kneer for accepting me as his Ph.D. student in the Department of Physics at the University of Göttingen and providing me numerous opportunities to present my results at Sternwarte solar group seminars. His encouraging and enlightening comments were tremendously helpful in polishing my research and my thesis. Thank you Franz!

The abilities of Prof. Dr. Sami K. Solanki and Dr. Bernd Inhester to simplify complex-looking problems and ideas really astonished me. My sincere thanks to both these people for taking time-out from their busy schedule to explain to me many different concepts that I found hard to comprehend. Thanks once again!

I would like to express my gratitude to Dr. Dieter Schmitt, the coordinator of the Max-Planck Research School on Solar System and Beyond, for providing us such a good academic atmosphere and for his help during my stay at MPS.

Special thanks to Shibu Mathew, J. M. Borrero, N. -E. Raouafi, Borut Podlipnik for their help in teaching me the ”ways of IDL” and the ”contours of LaTeX”. Thanks Shibu-Da Master, Nouri, Borut, Gracias Juna Ma! I also extend my thanks to Hebe, Marilena, Luciano, Mark, Katerina and Laura for always being there for me, helping me with discussions and suggestions, be it professional or personal, and with frequent coffee breaks. If I start mentioning all the names I am grateful to, well..... the publishers will complain. In short I would like to acknowledge the ”Lindau football team” and the help and support of the entire IMPRS group.

Cooking during the last months of a Ph.D. is a momentus task. But Roopali and Rajat with their *culinary skills*, came to my rescue. Thanks a lot to them and Aveek for their friendly support and advice.

A special word of mention towards Dr. Shantanu Rastogi and his wife Pooja Rastogi, Dr. U. S. Pandey, Dr. Vivek Tiwari and Prof. B. N. Dwivedi for their continuous support and guidance. Especially I would like to thank Dr. Shantanu

Rastogi and Pooja Rastogi for being instrumental in my efforts to come to Germany for higher education.

Finally and the most importantly, I would like to express my deep gratitude towards my parents, and all family members for their love, care and blessings. I would like to thank all my friends specially Janardan, Shikha, Saurabh in India and Urvashi in USA. They have always been extremely helpful and supportive.

This study is part of the scientific investigations of the project Stereo/Corona supported by the German "Bundesministerium für Bildung und Forschung" through the "Deutsche Zentrum für Luft- und Raumfahrt e.V." (DLR, German Space Agency) under project number 50 OC 0005. Stereo/Corona is a science and hardware contribution to the optical imaging package SECCHI, currently being developed for the NASA STEREO mission to be launched in 2006. I would like to thank the SOHO/LASCO/EIT/MDI consortium for providing the data and the software libraries and I acknowledge use of the CME catalog generated and maintained by NASA and The Catholic University of America in cooperation with the Naval Research Laboratory. SoHO is a project of international cooperation between ESA and NASA. I acknowledge the use of data from the American-Japanese satellite Yohkoh provided by the MSSL SURF group and of Hα data from the Observatory at Paris/Meudon distributed via the French BASS2000 and BBSO at California, USA. TRACE is a mission of the Stanford-Lockheed Institute for Space Research (a joint program of the Lockheed-Martin Advanced Technology Center's Solar and Astrophysics Laboratory and Stanford's Solar Observatories Group), and part of the NASA Small Explorer program.

Scientific Contributions

Refereed Publications:

[1] **Tripathi, D.**, Bothmer, V., Cremades, H. *The basic characterstics of EUV post-eruptive arcades and their role as tracers of coronal mass ejection source regions*, Astron. and Astrophys., 2004, 422, 33-349

[2] H. Cremades, Bothmer, V., **Tripathi, D** *Properties of structured coronal mass ejections in solar cycle 23*, COSPAR 2004, accepted

[3] **Tripathi, D.**, Bothmer, V., Solanki, S. K., Schwenn, R., Mierla, M., Stenborg, G. *Observation of a bright coronal inflow by SoHO/EIT*, To be submitted in Astron. and Astrophys., 2005

Conference Contributions:

[1] **Tripathi, D.**, Bothmer, V., Cremades, H. *Properties of post-eruptive arcades in solar cycle 23*, EGS-AGU-EUG Joint Assembly, 2003EAEJA..843T, 2003

[2] Cremades, H., Bothmer, V., **Tripathi, D.** *3D magnetic field configuration and evolution of coronal mass ejections*, EGS-AGU-EUG Joint Assembly, EAEJA..852C, 2003

[3] **Tripathi, D.**, Bothmer, V., Solanki, S. K., Schwenn, R., Mierla, M., Stenborg, G. *Plasma dynamics in prominence associated coronal mass ejection*, Proceedings of IAU 223. St. Petersburg, Russia, 2004

[4] **Tripathi, D.**, Bothmer, V., Solanki, S. K., Schwenn, R., Mierla, M., Stenborg, G. *SoHO/EIT observation of a coronal inflow*, Proceedings of IAU 226. Bejing, China, 2004

Lebenslauf

PERSÖNLICHE DATEN

Name	Durgesh Kumar Tripathi
Geburtsdatum	Juli 15, 1976
Geburtsort	Gorakhpur/Indien
Staatsangehörigkeit	Indien

SCHULBILDUNG

1982 - 1987	Primary School Badra, Gorakhpur, Indien
1988 - 1990	Intermediate College Bahuripar, Gorakhpur, Indien
1990 - 1992	Intermediate College Haradi-Chak, Gorakhpur, Indien
1992 - 1994	M. G. Intermediate College, Gorakhpur, Indien

STUDIUM

1995 - 1998	Bachelor of Science, St. Andrews College, University of Gorakhpur, Indien
1999 - 2001	Master of Science, University of Gorakhpur, Gorakhpur, Indien

PROMOTION

Feb. 2002 - Feb. 2005	Promotion an der Universitäts-Sternwarte Göttingen
Feb. 2002 - Jan. 2005	Stipendium des Max-Planck-Instituts für Sonnensystemforschung